Polymer Waveguide Micro-resonators for Optical Biosensors

UNIVERSITY
of
GLASGOW

Mohd Hazimin Mohd Salleh

This thesis is submitted in fulfilment of the requirement for
the Degree of Doctor of Philosophy (PhD)

Department Electronics and Electrical Engineering
School of Engineering
College of Science and Engineering
University of Glasgow

Author Declaration

" I declare that, except where explicit reference is made to the contribution of others, that this dissertation is the result of my own work and has not been submitted for any other degree at he University of Glasgow or any other institution "

Signature: _____

Name MOHD HAZIMIN MOHD SALLEH

Abstract

This work describes the investigation of optical ring or disk micro-resonator as elements in label-free biosensing devices. The use of polymeric materials for micro-resonator structures recently has been gain major interest multi disciplinary research since it allows rapid and straightforward fabrication process. The aim of the work described here was to develop an optical biosensor which operates within the visible range of λ = 500 – 800 nm based on micro-resonator principle by exploiting the SU-8 polymer material.

This thesis is focused on fabrication procedures using the electron beam lithography (EBL) technology, device characterization, biological element immobilization and sensing experiments. Through the use of EBL technology, a double-cascaded gapless disk resonator (DDR) structure has been fabricated in order to significantly increase (composite) free-spectral range (FSR) to 10.0 nm from the 1.3 nm achievable with a single gapless disk resonator. The DDR structures also overcome the fabrication complexity of obtaining 50 nm gap spacing for bus waveguide to micro-resonator coupling. In order to build the device into a biological sensing platform, a biological immobilization protocol has been optimized by evaluating the degree of surface functionalization using fluorescence microscopy and X-ray photoelectron spectroscopy (XPS). Following this, to deliver the solutions required for sensing experiments, the device is integrated with a microfluidic channel system.

In experiments using sucrose solutions, linear relationship between resonance wavelength shift and refractive index of the solution was achieved with the sensitivity of 12 nm/RIU. Further experiments were performed that used specific biotin-streptavidin antibody and multiple protein binding. These showed that the device was capable of detecting immobilised biomolecules. For example, the resonance wavelength shifted by 0.43 nm following streptavidin binding. Effort also has been devoted to perform experiments on combining the spectral absorption and resonance wavelength shift analysis since this device has a capability to operate in visible wavelength region, thus exploiting strongly coloured dyes. Here, using Dylight 649® labelled streptavidin, absorption at λ = 655 nm could be detected and was accompanied by a resonance wavelength shift of 0.261 nm.

From the experiments in this thesis, the DDR device that operated within the visible wavelength region has exhibited the capability of resonance wavelength shift for label-free detection and absorption spectra analysis for optical biosensing.

Acknowledgement

الحمـــد لله First of all, my sincere thanks to my supervisor Prof Jon Cooper for accepting me as his student. His infinite guidance, support and patience are highly appreciated particularly in helping me through this challenging experience in order to complete this work. I would like to thank Dr Andrew Glidle, a dedicated and resourceful person, for his help particularly improving my English and fruitful discussions.

Many thanks to Dr Rab Wilson for sharing a vast number of idea and support and to all the technical staff in James Watt Nanofabrication Centre (JWNC) for helping me with the fabrication work and sharing their technical knowledge. Thanks also go to other research colleagues that directly or indirectly involved in this work.

My special gratitude also goes to my sponsor Ministry of Higher Education of Malaysia, International Islamic University Malaysia (IIUM) for giving me this precious opportunity and fully funded scholarship.

Finally and most importantly, to my father Mohd Salleh Abd Rahman and Zaiton Abd Rahman and family for their infinite support and dua', last but not least to my beloved wife, Noor Isma Yanti Masseren and my two lovely daughters, Sarah Madihah and Anna Sumayyah. Their smiles and laughter give me strength and encouragement every day. Their patience and support after long working hours even during the weekend are highly delightful.

Table Of Contents

CHAPTER 3
Material and Fabrication

CHAPTER 4
Optical Characterization

CHAPTER 5
Biological Immobilization Protocol

CHAPTER 6
Applying Micro-resonator for Optical Biosensing

CHAPTER 7
Summary and Future Work

List of Conferences

M.H M. Salleh, A. Glidle, J.M Cooper, "Fabrication and Characterization of SU-8 Polymeric Microring Resonators for Biosensors", 5th IEEE EMBS UK & Republic of Ireland Postgraduate Conference on Biomedical Engineering and Medical Physics (PGBioMed 09), Magdalen College, University of Oxford, U.K, 12th – 14th July 2009.

M.H M. Salleh, A. Glidle, J.M Cooper, "Simulation and Characterization of SU-8 Polymer Gapless Microresonator Structure ", Malaysia-Glasgow Doctoral Colloquium (MGDC 2010), Scottish Exhibition and Conference Centre (SECC), Glasgow, Scotland, 20th – 21st January 2010.

M.H M. Salleh, A. Glidle, J.M Cooper, "Characterization of SU8 Polymer Gapless Disk Resonators Using Visible Wavelength Light Source", Optics and Photonics 2010 (Photon10), University of Southampton, U.K, 23rd– 26th August 2010. (2nd Runner-Up prize for poster session)

List of Tables

List of Figures

Abbreviations

APTES	3-aminopropyl triethoxysilane
NHS-biotin	biotinamidohexanoyl-6-aminohexanoic acid N-hydroxysuccinimide ester
BPM	beam propagation method
CAD	computer aided design
DI	de-ionised
DMSO	dimethyl sulfoxide
DDR	double-cascaded gapless disk resonator
EBL	electron beam lithography
FDTD	finite-difference time-domain
FITC	fluorescein isothiocyanate
GDSII	graphic design system
GUI	graphical user interface
IPA	isopropyl alcohol
NIR	near infrared
PBS	phosphate buffer saline
PDMS	polydimethylsiloxane
PMMA	poly (methyl 2-methylpropenoate)
PTFE	poly (difluoromethylene)
PEB	post-exposure bake
SEM	scanning electron microscope
SPR	surface plasmon resonance
TE	transverse electric
TM	transverse magnetic
TIR	total internal reflection
WGM	whispering gallery mode
XPS	x-ray photoelectron spectroscopy

CHAPTER 1

Introduction

1.1 Background

The word “biosensor” has various definitions and terminologies depending on the field of study, however in general terms it encompasses the wide-range of devices that give a response when a specific biological species presents itself to a detecting element. The detecting or transducing element in a biosensor can be based on an electrical, chemical or optical response, following interaction of the biological analyte with, for example, an enzyme, antibody, antigen or cell.

Increasing demand and the need for simple, user friendly and real-rime monitoring devices with rapid response times drives developments in biosensors. These are particularly important in a broad range of applications for example medical and health, pharmaceutical, microbiology, environmental monitoring, bioprocess, food technology, automotive and defence. Thus, the field of biosensing offers remarkable opportunities for both fundamental research and development (R&D) in the commercial sector. These R&D efforts are able to take advantage of other emerging and established technologies: biotechnology, photonics, and nano-technology.

Biosensor development can be dated back to the mid 1950’s, with the invention of the oxygen electrode by a scientist, Leland C. Clark[1]. He introduced the concept by entrapping glucose oxidase on the dialysis membrane that covered the oxygen-sensing electrode. He found that the oxygen concentration in a sample decreased in proportion to the increase in glucose concentration. After almost 20 years of research and improvement, his idea became a reality when the first commercial biosensor was successfully launched in 1975 by Yellow Spring

Instrument Company (YSI Inc, USA). This glucose analyser was used in blood, water or other liquids based on the amperometric detection of hydrogen peroxide (H_2O_2). For example, his invention enabled a surgeon to perform open-heart surgery because the blood constituency could be measured in real time rather than having to be taken to a specific laboratory for analysis (YSI Inc, USA). Importantly, today devices based on an extension of this concept help millions of people that have been diagnosed with diabetes to monitor the blood sugar levels (diabetes is one of the chronic disease worldwide, currently more than 220 million people have been diagnosed with diabetes according to World Health Organization, WHO). To date, the glucose-detector still retains the largest portion of the biosensor market (World Biosensors Market 2005, Frost and Sullivan).

Since mid 1970's, scientists and research communities together with specialization companies have put a vast amount of effort and investment to provide high accuracy, sensitive, user friendly, affordable and highly specific sensing devices for various applications. In the early 1980's, several biosensors for example pH sensors[2] and the surface plasmon resonance (SPR) immunosensor[3], were invented and commercialised. The latter led to the launch of the Pharmacia BIAcore company in 1990 (GE Heathcare,USA). Meanwhile the screen-printing the enzyme electrode for blood-glucose was introduced by MediSense in 1987, who were then purchased by Abbot in 1996 (this became one of the world biggest diabetes care biosensor devices). During the past 5 years, new biosensor applications have successfully penetrated the market showing strong growth with increasingly innovative approaches to new applications[4]. In addition, established academic journals and reports currently contain a variety of devices that can detect biological analytes for example enzymes, DNA and rNA, antigen-antibody and cells, merged at different sensing platforms (e.g. electrochemical, piezoelectric, optical and optoelectronics). In the coming years, it is predicted that the ultimate goal for biosensor technology will be towards sensitive, rapid detection and analysis, with robust and widely available devices that are simple to integrate with other systems[5][6]. Much of this will be facilitated by rapid prototyping capabilities.

The building blocks behind a biosensor device, include the transducer or sensor platform, a biological element that is normally immobilised onto the transducer, an analyte (i.e. specific biochemical reaction), output signal detection and an integrated fluidic channel. There are various types of transducer modalities for signal detection, for example electrochemical for measuring potentiometric or amperometric responses from redox molecules, electrical to measure conductivity, piezoelectric quartz crystal microbalance (QCM) resonance shifts, thermometric for heats of reaction, and optical (absorption, resonance shift, fluorescence and etc.). An important consideration in the development of a biosensor is how the biological analyte is presented to the transducing element. (e.g. a specific analyte can be an antigen in antibody-antigen interaction, or glucose in blood sugar analysis). Often, in order for the biological element to interact with the transducer, the surface of transducer needs to be functionalised

often with another biological species or molecular recognition molecule as illustrated in **Figure 1.1.**

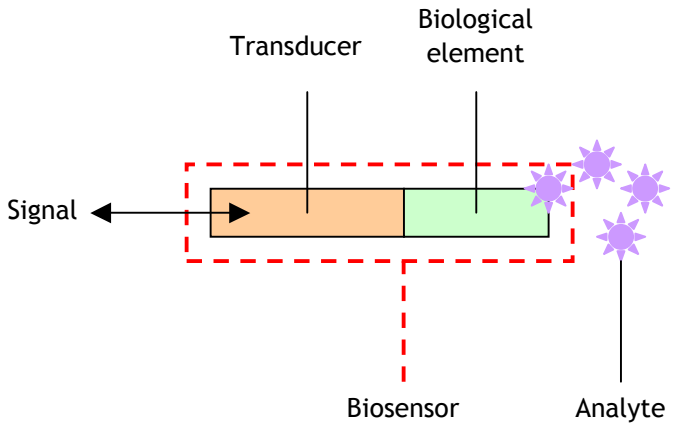

Figure 1.1: Schematic diagrams that represent building blocks for biosensing. Various types of input and output signal are exploited for example electrical, thermal and optical. Specific biological element is immobilised on the surface of transducer, as a sensing layer. The sensing involves biological binding between immobilised biological species with a specific analyte.

There are four common types of functionalization method to immobilize biological species. For example, membrane entrapment[7], physical adsorption[8], matrix entrapment and covalent bonding[9][10] (these are discussed further in **Chapter 5**). Physical adsorption refers to the combination of ionic, hydrophilic or hydrophobic and van der Waals' forces in order to attach the biological element onto the sensing surface. In the case of covalent bonding, the transducer is treated to put the specific functional group onto the sensing surface so that it can bind the biological species that can interact with the desired analyte. Biological interaction is then converted into a detectable signal so that the presence and amount of species present can be analysed. In a modern device, an integrated microfluidic channel system is used in order to dispense and manipulate the fluid during analyte detection. This system allows a smaller fraction (nano or pico liter) of analyte to be delivered and tested.

Whilst the electro-chemical biosensor (e.g. glucose sensor) dominates the end-user application market, recently optical biosensor technology has emerged as a trend and brought new innovative technologies into the market (developing the SPR biosensor by BIAcore). In an optical biosensor, the input and output signals are light, and the transducing element can either generate emission, phase or resonance shift, optical absorption or light scattering. With the excellent light delivery, low losses, immunity to electrical and magnetic interference, fibre optic technology offers advantages for detection capabilities.

Another remarkable advantage and interest in optical biosensing arises from the potential to perform label-free detection. Since biological species are generally transparent, usually they must be conjugated with fluorescent dyes for detection. With a label-free platform capability, optical biosensors can be operated without any fluorescence tag, luminescence or radioactive label. Consequently, loss of signal due to quenching of fluorescence tag or low sensitivity due to autofluorescence within the background signal can be avoided. Examples of the commercial optical biosensors are shown in **Figure 1.2**.

Figure 1.2: Commercial optical biosensors with different type of sensing method. (a) Epic® (Corning Inc, USA), the operating principle is based on refractive index waveguide surface to measure response the cellular signal of transduction (genetics) process; (b) Octet RED96® (ForteBio Inc,USA); (c) Biacore T200 (GE Heathcare,USA) measuring kinetic and affinity system using the SPR method and (d) AnaLight® System (Farfield Group Ltd, UK) analysing lipid and protein interaction using a planar waveguide platform.

In brief, optical biosensors can be divided into different classes depending on their principle of operation[7]; (i) light intensity changes because of absorption, scattering and reflection. Here, the direct light is introduced onto the sample and light transmission is measured; (ii) frequency or wavelength changes generated by a fluorescence tag when excited

with light at the specific wavelength and (iii) resonance angle or wavelength shifts produced from the changes of refractive index at an interface.

There are various types of optical biosensor formats, for example fibre optics, surface plasmon resonance (SPR) prisms and planar waveguides. Fibre-optic biosensors are the one of the most commonly investigated and offer excellent configuration possibilities[11,12]. Usually, the end tip or cladding of the fibre optic is functionalised with a biological species to give an active sensing layer to probe the specific analyte interaction. Despite being miniaturised, fibre-optic biosensors also offer the capability of being adapted for in-vivo measurement, thus enabling the measurement to be performed inside the body.

Another recent technology that utilizes an optical principle is SPR[13, 14]. Here, an evanescent field is generated that extends away from the metal-dielectric interface, when incident light (e.g. a laser) strikes the dielectric (e.g. prism) - metal interface at a specific angle. The thin metal (gold) layer, then acts as a detection surface and biological species immobilised onto the thin metal layer surface forming the sensing layer. At this specific angle p-polarized light will interact with free electrons from the metal surface and convert them into the surface plasmon waves. A dip in reflectivity of the light is seen when the light strikes the metal interface at the resonance angle. When the biological interaction (e.g. absorption or binding) occurs, the refractive index of the layer on top of the gold film changes and so the resonance condition of the dielectric of the thin metal layer is altered. As a result, the reflectivity angle (°) is shifted and this shift can be measured with the photodiode array. This shift can be measured in real time and so the kinetics of the absorption can be studied. Since this shift depends only on the absorption of the biomolecules on the sensing surface, it can be used as a label-free platform.

Planar waveguides also demonstrate a great potential in optical biosensing. Adapting similar concepts to those used for fibre-optic waveguides, light is confined inside the waveguide by total internal reflection (TIR) with a surrounding or cladding refractive index. Generally, planar waveguide platforms for optical biosensors exploit the evanescence field phenomenon of the exposed interface to interrogate the presence of analytes that absorbed onto the surface or in the surrounding media. When the light propagates along the waveguide, the interface between core and surrounding medium of higher and lower refractive index respectively produces a localised evanescent field region when guided light strikes the interface at the critical angle. This localised area can be is utilised for either fluorescence sensing[15] or refractive index detection when the existence of analyte has changed the effective index of the guiding mode[16][17]. Various configurations of fabricated planar waveguide have been used as optical biosensors, for example the Mach-Zehnder interferometer (MZI)[18][19][20], multimode interference waveguide (MMI)[21], resonance waveguide grating (RWG)[22] and micro-resonator.

For example, Mach-Zehnder interferometers (MZI) are constructed with a single input that splits into two waveguide channels to form a reference and sensing arm that are then recombined to give the output channel. On the sensing arm, a biological element, suitable for binding interaction is immobilised while the reference is kept unmodified to provide a 'control' light path. When the input light is split into the two arms when the light travelling down. The sensing arms experiences a different refractive index at the waveguide surface compared to the light in the reference arm. This results in a phase difference in the light of the two arms. When the light is recombined in the output channel, this generates an interference pattern that can be accurately measured. These small changes in the phase shift can be correlated with binding interactions or thickness changes of the immobilised surface.

There are many advantages of the planar waveguide as an optical biosensor. Firstly, planar waveguides providing a larger sensing area compared to the tip of a fibre-optic in a single device. This provides a wider sensing area and enhanced capability for multi layer analyte detection. Another advantage is the planar structure can be more easily integrated with a microfluidic system. As with fibre-optics platform, this planar waveguide geometry also shows the capability of label-free biosensing, thus allowing wider range of complex biological analyte detection without any fluorescence or dyes label[23].

However, there are a few drawbacks to optical biosensor configurations. For example, with the SPR system the optical setup is complex and the measurements require careful interpretation. In case of the planar waveguide especially for MZI, MMI or resonance grating arrangement, the disadvantage lies in the interaction length required i.e. the longer dimension of the planar waveguide. In order to detect analyte interaction or biological binding especially in a lower concentration condition, sufficient phase-shift of the propagated light needs to be achieved. Therefore longer waveguides (reference and sensing arm for MZI) need to be fabricated to overcome the problem.

1.2 Motivation

Due to the need to produce relatively low sensing arms (~ 15 mm) of MZI optical biosensing device[19], there has been a drive to investigate the possibility to obtain sufficient interaction without having to increase the dimension of the device. One principle, by which this can be done is to exploit a resonance effect, as in optical microring resonator. Generally, an optical resonance occurs when the propagated light is coupled into the micro-resonator structure at certain resonance wavelengths. The light is confined inside the structure by TIR principle. The resonance light circulates inside the micro-resonator structure (e.g. ring or disk) until it disappears due to output coupling, material absorption or scattering losses. By exploiting the continuous circulation of resonance light inside the resonance cavity, numerous interactions can

occur between the generated evanescence field and analyte on the resonator surface. Therefore, an optical micro-resonator biosensor platform has the potential to offer a greater degree of interaction with the immobilised biomolecules and still have the capability of being miniaturized into sub-mm devices.

Despite being demonstrated as promising platforms for fundamental studies in many applications associated with photonics such as laser emission[24][25], channel dropping filters[26][27], couplers[28], switches[29] and sensors[30]. Recently, the micro-resonator structures have also been extensively investigated and utilised in biosensing applications. There are many types of micro-resonator structures in which the resonator element is a micro-sphere[31][32], a micro-ring[33][34][35], a micro-disk[36], a micro-cylinder[37], a micro-particle[38] or a micro-toroid[39][40]. These structures allow light to circulate inside the micro-resonator and generate an enhanced evanescent field. This phenomenon is known as the Whispering Gallery Mode (WGM), which can be exploited for biological analyte detection.

In order to confine the light inside the micro-resonator structure, several materials have been used such as silica[41][42], silicon-on-insulator (SOI)[43][44][45], silicon nitride (Si_3N_4)[33][46], glass [34][47], and polymer[48][49] (see **Figure 1.3**). In general, the silicon-based materials have the high refractive index required for efficient light confinement. In addition, they can be fabricated using advance complementary metal-oxide-semiconductor (CMOS) technology facilities[45], leading to mass production of devices. However, in terms of fabrication, silicon based materials need to undergo many processing steps consisting of growth or layer deposition, dry etching, wet etching and multi layer patterning to create the waveguide structure. Each step requires precision and it is a demanding process. The current research of optical micro-resonators for biosensors is tabulated as follows:-

Table 1.1: Recent approach on optical micro-resonator biosensor.

No	Author	Year	Material	Operational λ/nm	Sensing structure	Purpose
1	Carlborg *et. al.*	2010	Si_3N_4	1260-1360	Slot ring resonator waveguide	Label-free assay (BSA)
2	Dai *et. al.*	2009	SU-8	1550-1555	Strip racetrack resonator	High Q device ~ 8000
3	Chen *et. al.*	2009	Si_3N_4	1546-1554	Microring resonator	Glucose sensing
4	De Vos *et. al.*	2009	SOI	1550-1590	Microring resonator	Biotin-avidin detection
5	Ramachandran *et. al.*	2008	Hydex Glass	1530-1610	Microring resonator	Bacterial detection
6	Robinson *et. al.*	2008	Si	1520-1620	Slot ring resonator waveguide	Gas detection - acetylene
7	Sumetsky *et. al.*	2007	Capillary fibre	1540-1545	Optical liquid ring resonator	Different liquid refractive index
8	Passaro *et. al.*	2007	SOI	1550-1560	Microring resonator	Ammonia detection
9	Armani *et. al.*	2007	Si	1300-1350	Microcavity resonator	Single molecule detection
10	Chao *et. al.*	2006	Polystyrene	1550-1580	Microring resonator	Biochemical detection

It can be seen in the **Table 1.1**, generally silicon based material is used to fabricate the micro-resonator structure and the sensing application is operated within the communication wavelength range between λ = 1300 - 1600 nm as a tuneable broadband source.

Various polymer materials have been investigated as waveguide materials in order to reduce the fabrication complexity and allow the development of novel structures. Polymers that have been explored include polystyrene (PS)[50], poly(methyl-methacrylate) (PMMA)[51], polyimide (PI)[52] and SU-8[53][54][55]. In general, the polymer fabrication process consists of a sequence of resist layer spinning, pattern exposure, and then development. These are simple fabrication processes[55][56][57] compared to the chemical or physical deposition and dry etching procedure required for silicon based materials. In addition, the polymer material also offers low cost of raw material, a means of altering the refractive index[58][59], high-speed patterning processes and the possibility of functionalization with chemicals for the detection of biological molecules. Since the SU-8 polymer material offers the highest refractive index among the photo-patternable polymer available, it was chosen as a waveguide core structure to explore in fabrication of a micro-resonator biosensing device. Although polymers have been used for microresonators, little work has been done using visible wavelength light.

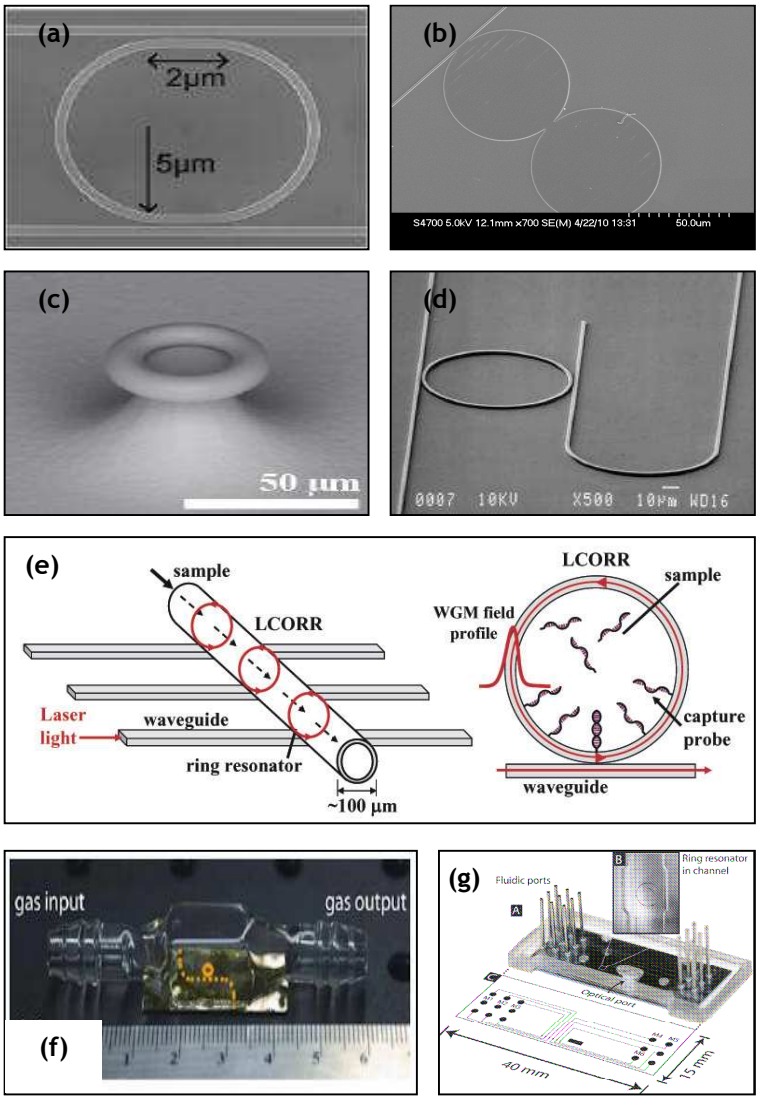

Figure 1.3: Examples of fabricated micro-resonator structures in optical biosensor application. (a) Microring racetrack[45]; (b) Double-cascaded gapless disk[60]; (c) Micro-toroid for single molecule[61]; (d) Polymer microring[48]; e) liquid-core optical-ring-resonator (LCORR)[62] (f) Micro-ring gas sensor[63]; and (g) Micro-slot resonator[17].

Several recent applications in optical biosensing utilising the micro-resonator building block have been used for the detection of low refractive index analytes[17], biotin-avidin interaction[17][34][36][45][41], gas sensing[63], cell growth[64] and viruses[38]. Most of these devices operate in the communication wavelength band between λ = 1300 – 1550 nm since the silicon (Si) based material upon which they are based, is not transparent in the visible wavelength region. Although Si performs well in the communication wavelength, it is not used widely in optical biosensing, which uses visible wavelength light[55][65], (e.g. those involving coloured species or

labels, or in sensors that can also be compromised by the high optical absorption of water in this wavelength band).

Due to the above characteristics and considerations, SU-8 polymer micro-resonators that can operate at the visible wavelength region λ = 500 – 800 nm were investigated in this thesis. Usefully, in addition to the detection of a resonance wavelength, the visible wavelength range also allows this device to be used in detecting labelled molecules with coloured tags.

1.3 Merit of The Research

a. Low cost: The use of polymer reduces the cost.

Visible light source / bulb (100W, 12V) would be around GBP10 compared to the tunable laser / super continuum laser source that will cost around GBP40k.

Low cost of polymer material can reduce the overall price when compared to silicon based material.

b. Easy fabrication: The use of polymers makes fabrication easier.

Straightforward fabrication process by using negative resist SU8 polymer without the need for multilayer depositions, dry etching and wet etching.

c. Polymer material: The material has the following properties.

Capability to tune the refractive index of SU8 polymer by using different recipes during development processes.

SU8 polymer processing is a fast patterning process with low dose (2.0 μC/cm^2) compared to silicon base material.

d. Integration with biological element

Direct surface modification and protein immobilization protocol.

Different visible wavelength dyes can be used as tags to uniquely identify immobilised species, particularly in complex mixtures.

1.4 Aims and Objectives

The main aims and objectives for the project are to design, fabricate, characterize and utilise the double-cascaded gap and gapless ring and disk resonators as a platform for optical biosensors. These fabricated structures should operate in the visible wavelength region between 500-800 nm. The devices must also be integrated with a microfluidic channel for analyte delivery and the surface of the sensing structures must be capable of chemical modification for protein immobilization of the biosensing detection. Optical characteristics of the ring and disk structures were simulated and experimentally characterized in order to compare the optical output behaviour. The experiments with the bulk refractive index and specific surface detection were then performed. In general, the aims and objectives of the work are as follows: -

- To study the behaviour of the output response of the micro resonator and compare with the gapless spacing resonator structures.
- To design and fabricate the SU-8 polymer micro resonator structures.
- To characterise and understand the basic concept of micro resonators.
- To fabricate the microfluidic channel and integrate onto the sensing device for analytes delivery.
- To study and investigate the surface modification and protein immobilization protocol
- To exploit the double-cascaded gapless disk resonator response characteristic into the bulk refractive index and specific protein interaction detection.
- To explore the application for both label-free and labelled biosensing applications in the visible wavelength range.

1.5 Thesis Outline

This thesis will present progress towards and realization of an optical biosensor device based on SU8 polymer waveguide technology.

Chapter 2 (Theory and Simulation) is divided into two sections. In the first section, the fundamental background of micro resonator waveguide and related parameters are described. In the second section, the Finite Difference Time Domain (FDTD) simulation is shown in order to obtain an overview of optical response of the device design. Important parameters are simulated

and discussed. In addition, the gapless resonator structure is also described for comparison. Due to the computational complexity, only 2D FDTD approaches are explored.

Chapter 3 (Material and Fabrication) describes the fabrication techniques used to develop the SU-8 polymer microring and microdisk structures. The whole fabrication processes begins with designing waveguide pattern structures and finished with integration of a microfluidic channel on the sensing device. Electron beam pattern writing processes using the Vistec VB6 electron beam lithography (EBL) tool and pattern development processes are involved in the fabrication process, each of which must be optimized in order to achieve devices having the small critical dimensions required for efficient waveguide transmission and coupling properties.

Chapter 4 (Optical Characterization) presents the experimental setup and instruments that were involved in the optical characteristic performed in this research. Calibration and basic alignment were performed to couple the light from the visible wavelength source into the input waveguide of the resonator device. The first part of this chapter is dedicated to characterize the resonance response of the gapless microring and microdisk. Following this, investigation on gapless double-cascaded disk resonator is discussed.

Chapter 5 (Biological Immobilization Protocol) describes the SU-8 surface modification characterization required to determine the correct protocol for protein immobilization. Two types of measurements are conducted to validate the functional group and chemical reaction protocol of the modified SU-8 surface, namely fluorescence microscopy and X-ray photoelectron spectroscopy (XPS).

Chapter 6 (Application of Micro-resonators For Optical Biosensing) concerns with the experiments conducted to measure the refractive index changes within aqueous solutions. Bulk detection of sucrose solution is investigated for calibration purposes. A specific protein binding experiment (biotin-streptavidin) is conducted in order to investigate the capability of the SU-8 double-cascaded gapless disk resonator device to be utilized as a platform for label-free biomolecules detection. In addition, a multiple protein binding assay is investigated involving antibody-antigen binding, as in an immunoassay.

Chapter 7 (Summary and Future Work) provides a summary and conclusion from this work. An illustration is also given of future directions including an absorption spectrophotometer system based on a single channel, without the need for the usual reference channel measurements. This could be configured as a dual detection platform in which resonance shifts are measured in combination with optical absorptions.

References

[1] L. C. Clark, "Monitor and Control of Blood and Tissue Oxygen Tensions," *Transactions American Society for Artificial Internal Organs*, vol. 2, pp. 41-&, 1956.

[2] J. I. Peterson, S. R. Goldstein, R. V. Fitzgerald, and D. K. Buckhold, "Fiber Optic pH Probe for Physiological Use," *Analytical Chemistry*, vol. 52, pp. 864-869, 1980.

[3] B. Liedberg, C. Nylander, and I. Lundstrom, "Surface-Plasmon Resonance for Gas-Detection and Biosensing," *Sensors and Actuators*, vol. 4, pp. 299-304, 1983.

[4] R. Thusu, "Strong Growth Predicted for Biosensors Market," Sensors Magazine, 2010.

[5] A. P. F. Turner, "Current Trends in Biosensor Research and Development," *Sensors and Actuators*, vol. 17, pp. 433-450, 1989.

[6] M. E. Bosch, A. J. R. Sanchez, F. S. Rojas, and C. B. Ojeda, "Recent development in optical fiber biosensors," *Sensors*, vol. 7, pp. 797-859, 2007.

[7] Prasad, P.N., Introduction to biophotonics; John Wiley and Sons, Inc., USA 2003

[8] S. L. Hirsh, M. M. M. Bilek, N. J. Nosworthy, A. Kondyurin, C. G. dos Remedios, and D. R. McKenzie, "A Comparison of Covalent Immobilization and Physical Adsorption of a Cellulase Enzyme Mixture," *Langmuir*, vol. 26, pp. 14380-14388, 2010.

[9] E. P. Diamandis and T. K. Christopoulos, "The Biotin (Strept)Avidin System - Principles and Applications in Biotechnology," *Clinical Chemis*try, vol. 37, pp. 625-636, 1991.

[10] M. Joshi, R. Pinto, V. R. Rao, and S. Mukherji, "Silanization and antibody immobilization on SU-8," *Applied Surface Science*, vol. 253, pp. 3127-3132, 2007.

[11] N. Verma, S. Kumar "Fiber Optic Biosensor for the Detection of Cd in Milk," *J Biosens Bioelectron* vol. 1, pp. 102, 2010.

[12] S. H. Ohk, O. K. Koo, T. Sen, C. M. Yamamoto, and A. K. Bhunia, "Antibody-aptamer functionalized fibre-optic biosensor for specific detection of Listeria monocytogenes from food," *Journal of Applied Microbiology*, vol. 109, pp. 808-817, 2010.

[13] T. Vo-Dinh and B. Cullum, "Biosensors and biochips: advances in biological and medical diagnostics," *Fresenius Journal of Analytical Chemistry*, vol. 366, pp. 540-551, 2000.

[14] B. P. Nelson, T. E. Grimsrud, M. R. Liles, R. M. Goodman, and R. M. Corn, "Surface plasmon resonance imaging measurements of DNA and RNA hybridization adsorption onto DNA microarrays," *Analytical Chemistry*, vol. 73, pp. 1-7, 2001.

[15] Y. Enami, T. Fukuda, and S. Suye, "Sol-gel silica planar waveguide doped with green fluorescent protein for in-line biosensors," *Applied Physics Letters*, vol. 91, pp. -, 2007.

[16] C. Y. Chao, W. Fung, and L. J. Guo, "Polymer microring resonators for biochemical sensing applications," *IEEE Journal of Selected Topics in Quantum Electronics*, vol. 12, pp. 134-142, 2006.

[17] C. F. Carlborg, K. B. Gylfason, A. Kazmierczak, F. Dortu, M. J. B. Polo, A. M. Catala, G. M. Kresbach, H. Sohlstrom, T. Moh, L. Vivien, J. Popplewell, G. Ronan, C. A. Barrios, G. Stemme, and W. van der Wijngaart, "A packaged optical slot-waveguide ring resonator sensor array for multiplex label-free assays in labs-on-chips," *Lab on a Chip*, vol. 10, pp. 281-290, 2010.

[18] B. J. Luff, J. S. Wilkinson, J. Piehler, U. Hollenbach, J. Ingenhoff, and N. Fabricius, "Integrated optical Mach-Zehnder biosensor," *Journal of Lightwave Technology*, vol. 16, pp. 583-592, 1998.

[19] B. Sepulveda, J. S. del Rio, M. Moreno, F. J. Blanco, K. Mayora, C. Dominguez, and L. M. Lechuga, "Optical biosensor microsystems based on the integration of highly sensitive Mach-Zehnder interferometer devices," *Journal of Optics a-Pure and Applied Optics*, vol. 8, pp. S561-S566, 2006.

[20] D. Esinenco, S. D. Psoma, M. Kusko, A. Schneider, and R. Muller, "Su-8 micro-mosensor based on Mach-Zehnder interferometer," *Reviews on Advanced Materials Science*, vol. 10, pp. 295-299, 2005.

[21] K. R. Kribich, R. Copperwhite, H. Barry, B. Kolodziejczyk, J. M. Sabattie, K. O'Dwyer, and B. D. MacCraith, "Novel chemical sensor/biosensor platform based on optical multimode interference (MMI) couplers," *Sensors and Actuators B-Chemical*, vol. 107, pp. 188-192, 2005.

[22] Y. Fang, "Non-invasive optical biosensor for probing cell signalling," *Sensors*, vol. 7, pp. 2316-2329, 2007.

[23] Cooper, M.A., Label-Free Biosensor: Techniques and Applications; Cambridge University Press, UK, 2009

[24] A. F. J. Levi, R. E. Slusher, S. L. Mccall, J. L. Glass, S. J. Pearton, and R. A. Logan, "Directional Light Coupling from Microdisk Lasers," *Applied Physics Letters*, vol. 62, pp. 561-563, 1993.

[25] D. G. Rabus, Z. X. Bian, and A. Shakouri, "A GaInAsP-InP double-ring resonator coupled laser," *IEEE Photonics Technology Letters*, vol. 17, pp. 1770-1772, 2005.

[26] B. E. Little, S. T. Chu, H. A. Haus, J. Foresi, and J. P. Laine, "Microring resonator channel dropping filters," *Journal of Lightwave Technology*, vol. 15, pp. 998-1005, 1997

[27] D. Lee, T. Lee, J. Park, S. Kim, W. Hwang, and Y. Chung, "Widely tunable double-ring-resonator add/drop filter using high-index-contrast polymer waveguide," 2007 Pacific Rim Conference on Lasers and Electro-Optics, Vols 1-4, pp. 822-8231441, 2007.

[28] L. Caruso and I. Montrosset, "Analysis of a racetrack microring resonator with MMI coupler," *Journal of Lightwave Technology*, vol. 21, pp. 206-210, 2003.

[29] A. Yariv, "Critical coupling and its control in optical waveguide-ring resonator systems," *IEEE Photonics Technology Letters*, vol. 14, pp. 483-485, 2002.

[30] B. Bhola, H. C. Song, H. Tazawa, and W. H. Steier, "Polymer microresonator strain sensors," *IEEE Photonics Technology Letters*, vol. 17, pp. 867-869, 2005.

[31] F. Vollmer, D. Braun, A. Libchaber, M. Khoshsima, I. Teraoka, and S. Arnold, "Protein detection by optical shift of a resonant microcavity," *Applied Physics Letters*, vol. 80, pp. 4057-4059, 2002.

[32] N. M. Hanumegowda, I. M. White, H. Oveys, and X. D. Fan, "Label-free protease sensors based on optical microsphere resonators," *Sensor Letters*, vol. 3, pp. 315-319, 2005.

[33] J. P. Guo, M. J. Shaw, G. A. Vawter, G. R. Hadley, P. Esherick, and C. T. Sullivan, "High-Q microring resonator for biochemical sensors," *Integrated Optics: Devices, Materials, and Technologies IX*, vol. 5728, pp. 83-92368, 2005.

[34] A. Yalcin, K. C. Popat, J. C. Aldridge, T. A. Desai, J. Hryniewicz, N. Chbouki, B. E. Little, O. King, V. Van, S. Chu, D. Gill, M. Anthes-Washburn, and M. S. Unlu, "Optical sensing of biomolecules using microring resonators," *IEEE Journal of Selected Topics in Quantum Electronics*, vol. 12, pp. 148-155, 2006.

[35] S. Mookherjea, "Mode cycling in microring optical resonators," *Optics Letters*, vol. 30, pp. 2751-2753, 2005.

[36] R. W. Boyd and J. E. Heebner, "Sensitive disk resonator photonic biosensor," *Applied Optics*, vol. 40, pp. 5742-5747, 2001.

[37] Y. Z. Sun, S. I. Shopova, G. Frye-Mason, and X. D. Fan, "Rapid chemical-vapor sensing using optofluidic ring resonators," *Optics Letters*, vol. 33, pp. 788-790, 2008.

[38] S. Arnold, R. Ramjit, D. Keng, V. Kolchenko, and I. Teraoka, "MicroParticle photophysics illuminates viral bio-sensing," *Faraday Discussions*, vol. 137, pp. 65-83, 2008.

[39] A. M. Armani and K. J. Vahala, "Chemical and biological detectors using ultra-high-Q microresonators," *Optomechatronic Micro/Nano Devices and Components II*, vol. 6376, pp. U48-U57215, 2006.

[40] H. K. Hunt, C. Soteropulos, and A. M. Armani, "Bioconjugation Strategies for Microtoroidal Optical Resonators," *Sensors*, vol. 10, pp. 9317-9336, 2010.

[41] A. Densmore, D. X. Xu, P. Waldron, S. Janz, T. Mischki, G. Lopinski, J. Lapointe, A. Delage, E. Post, C. Storey, P. Cheben, B. Lamontagne, and J. H. Schmid, "Densely Folded Silicon Photonic Wire Biosensors in Ring Resonator and Mach-Zehnder Configurations," *2008 Conference on Lasers and Electro-Optics & Quantum Electronics and Laser Science Conference*, Vols 1-9, pp. 1947-19483638, 2008.

[42] F. Vollmer and S. Arnold, "Whispering-gallery-mode biosensing: label-free detection down to single molecules," *Nature Methods*, vol. 5, pp. 591-596, 2008.

[43] D. X. Xu, M. Vachon, A. Densmore, R. Ma, A. Delage, S. Janz, J. Lapointe, Y. Li, G. Lopinski, D. Zhang, Q. Y. Liu, P. Cheben, and J. H. Schmid, "Label-free biosensor array based on silicon-on-insulator ring resonators addressed using a WDM approach," *Optics Letters*, vol. 35, pp. 2771-2773, 2010.

[44] V. M. N. Passaro, F. Dell'Olio, B. Casamassima, and F. De Leonardis, "Guided-wave optical biosensors," *Sensors*, vol. 7, pp. 508-536, 2007.

[45] K. De Vos, J. Girones, S. Popelka, E. Schacht, R. Baets, and P. Bienstman, "SOI optical microring resonator with poly(ethylene glycol) polymer brush for label-free biosensor applications," *Biosensors & Bioelectronics*, vol. 24, pp. 2528-2533, 2009.

[46] C. A. Barrios, B. Sanchez, K. B. Gylfason, A. Griol, H. Sohlstrom, M. Holgado, and R. Casquel, "Demonstration of slot-waveguide structures on silicon nitride/silicon oxide platform," *Optics Express*, vol. 15, pp. 6846-6856, 2007.

[47] A. Ramachandran, S. Wang, J. Clarke, S. J. Ja, D. Goad, L. Wald, E. M. Flood, E. Knobbe, J. V. Hryniewicz, S. T. Chu, D. Gill, W. Chen, O. King, and B. E. Little, "A universal biosensing platform based on optical micro-ring resonators," *Biosensors & Bioelectronics*, vol. 23, pp. 939-944, 2008.

[48] C. Y. Chao, W. Fung, and L. J. Guo, "Polymer microring resonators for biochemical sensing applications," IEEE Journal of Selected Topics in Quantum Electronics, vol. 12, pp. 134-142, 2006.

[49] P. Rabiei and W. H. Steier, "Micro-ring resonators using polymer materials," Leos 2001: *14th Annual Meeting of the IEEE Lasers & Electro-Optics Society*, Vols 1 and 2, Proceedings, pp. 517-518907, 2001.

[50] C. Y. Chao and L. J. Guo, "Design and optimization of microring resonators in biochemical sensing applications," *Journal of Lightwave Technology*, vol. 24, pp. 1395-1402, 2006.

[51] M. Balakrishnan, M. Faccini, M. B. J. Diemeer, E. J. Klein, G. Sengo, A. Driessen, W. Verboom, and D. N. Reinhoudt, "Microring resonator based modulator made by direct photodefinition of an electro-optic polymer," *Applied Physics Letters*, vol. 92, pp. -, 2008.

[52] H. P. Lee, J. J. Park, H. H. Ryoo, S. G. Lee, O. B. Hoan, and E. H. Lee, "Resonance characteristics of waveguide-coupled polyimide microring resonator," *Optical Materials*, vol. 21, pp. 535-541, 2003.

[53] A. Leinse, M. B. J. Diemeer, A. Rousseau, and A. Driessen, "A novel high-speed polymeric EO modulator based on a combination of a microring resonator and an MZI," *IEEE Photonics Technology Letters*, vol. 17, pp. 2074-2076, 2005.

[54] S. Y. Cho and N. M. Jokerst, "Polymer microrings integrated with thin film InGaAs MSM photodetectors for Sensor-on-a-Chip applications," *2006 International Conference on Indium Phosphide and Related Materials Conference Proceedings*, pp. 222-225446, 2006.

[55] D. X. Dai, B. Yang, L. Yang, Z. Sheng, and S. L. He, "Compact Microracetrack Resonator Devices Based on Small SU-8 Polymer Strip Waveguides," *IEEE Photonics Technology Letters*, vol. 21, pp. 254-256, 2009.

[56] T. M. Benson, S. V. Boriskina, P. Sewell, A. Vukovic, S. C. Greedy, and A. I. Nosich, "Micro-optical resonators for microlasers and integrated optoelectronics - Recent advances and future challenges," *Frontiers in Planar Lightwave Circuit Technology Design, Simulation, and Fabrication*, vol. 216, pp. 39-70287, 2006.

[57] G. T. Paloczi, Y. Y. Huang, A. Yariv, and S. Mookherjea, "Polymeric Mach-Zehnder interferometer using serially coupled microring resonators," *Optics Express*, vol. 11, pp. 2666-2671, 2003.

[58] B. H. Ong, X. Yuan, S. Tao, and S. C. Tjin, "Photothermally enabled lithography for refractive-index modulation in SU-8 photoresist," *Optics Letters*, vol. 31, pp. 1367-1369, 2006.

[59] B. Y. Shew, C. H. Kuo, Y. C. Huang, and Y. H. Tsai, "UV-LIGA interferometer biosensor based on the SU-8 optical waveguide," *Sensors and Actuators a-Physical*, vol. 120, pp. 383-389, 2005.

[60] M.H M. Salleh, A. Glidle, J.M Cooper, "Characterization of SU8 Polymer Gapless Disk Resonators Using Visible Wavelength Light Source", *Optics and Photonics 2010 (Photon10)*, University of Southampton, U.K, 23rd– 26th August 2010.

[61] H. K. Hunt and A. M. Armani, "Label-free biological and chemical sensors," *Nanoscale*, vol. 2, pp. 1544-1559, 2010.

[62] I. M. White, H. Y. Zhu, H. Oveys, and X. D. Fan, "Bio/chemical sensors based on liquid core optical ring resonators - art. no. 62230F," *Micro (MEMS) and Nanotechnologies for Space Applications*, vol. 6223, pp. F2230-F2230216, 2006.

[63] J. T. Robinson, L. Chen, and M. Lipson, "On-chip gas detection in silicon optical microcavities," *Optics Express*, vol. 16, pp. 4296-4301, 2008.

[64] S. P. Wang, A. Ramachandran, and S. J. Ja, "Integrated microring resonator biosensors for monitoring cell growth and detection of toxic chemicals in water," *Biosensors & Bioelectronics*, vol. 24, pp. 3061-3066, 2009.

[65] E. S. Hosseini, S. Yegnanarayanan, A. H. Atabaki, M. Soltani, and A. Adibi, "High Quality Planar Silicon Nitride Microdisk Resonators for Integrated Photonics in the Visible Wavelength Range," *Optics Express*, vol. 17, pp. 14543-14551, 2009.

[66] Yellow Spring Instrument Inc, USA. [Online]. Available: http://www.ysi.com

[67] World Health Organization [Online]. Available: http://www.who.int/

[68] GE Healthcare, USA [Online]. Available: http://www.biacore.com

[69] Frost and Sullivan Ltd, UK. [Online]. Available: http://www.frost.com

[70] Corning Inc, USA [Online]. http://www.corning.com/

[71] ForteBio Inc, USA [Online]. http://www.fortebio.com/

[72] Farfield Group Ltd, UK [Online]. http://www.fairfieldgroup.com/

CHAPTER 2

Theory and Simulation

Introduction

This chapter is divided into two sections. In the first section, the optical micro resonator concept and parameters related to biosensing activity are presented. The second section discusses the simulation performed in order to investigate the output response behaviour of the microring resonator. In general, this section aims to give an overview about the principle of an optical micro resonator and highlight the important output characteristics that must be understood and considered when designing optical biosensing devices based on micro-resonators.

2.1 Micro-resonator: The Theory

The resonator concept is related to the confinement of light inside a resonator structure. There are several geometries that can be used as resonator structures including spheres, cylinders, disks and rings[1][2][3]. However for reasons of ease of fabrication, in this thesis, only the ring and disk geometry have been considered as dielectric resonator structures. A dielectric waveguide allows light to propagate and be confined inside the structure when the core, of

refractive index n_1, is surrounded by a medium (or cladding) of refractive index n_2 and IR(n_1) > IR(n_2).

The circulating light inside the micro resonator structure experiences total internal reflection (TIR) at the interface or boundary between the core and medium under certain specific conditions[4][5]. In general, the TIR phenomenon occurs when light from the higher refractive index core strikes the lower refractive index boundary at an angle greater than the critical angle measured relative to the interface (Equation 2.0).

$$\theta_c = \arcsin\left(\frac{n_2}{n_1}\right) \qquad (2.0)$$

where θ_c is the critical angle, n_1 is the core refractive index, and n_2 is the refractive index of cladding or surrounding media. The ratio $\left(\frac{n_2}{n_1}\right)$ needs to be less than 1, in order to satisfy the TIR condition. As discussed below, if we consider the wave functions that describe the reflected and circulating light inside the resonator structure, these superimpose on each other either constructively or destructively, depending on the wavelength. Importantly for sensing applications, a consequence of TIR, is the development of an evanescent field along the dielectric boundary. This evanescent field can interact with molecules on the waveguide surface or bulk solution, exhibits exponential decay with increasing distance from the core-cladding interface. This phenomenon was initially observed by Lord Raleigh in 1912 and can be analysed as a whispering gallery mode (WGM).

2.1.1 Whispering Gallery Mode (WGM)

The WGM phenomenon has been behind the development and construction of microring resonator building blocks for a variety of applications, especially in the telecommunication field e.g. dropping filters, switches and converters [6][7][8]. Besides uses associated with communication wavelengths, devices based on this phenomenon have been demonstrated to have versatility and advantages that can be utilised in biosensing applications e.g. the surface plasmon resonance (SPR) sensor.

In order to utilise the capability of microring resonator structures as optical sensors, a bus waveguide must be introduced to couple the input light and collect the output light spectrum that is determined by the resonator pattern behaviour (see **Figure 2.1**). In this configuration, the light is evanescently coupled into and out of the resonator structure via the gap between the bus waveguides and resonators.

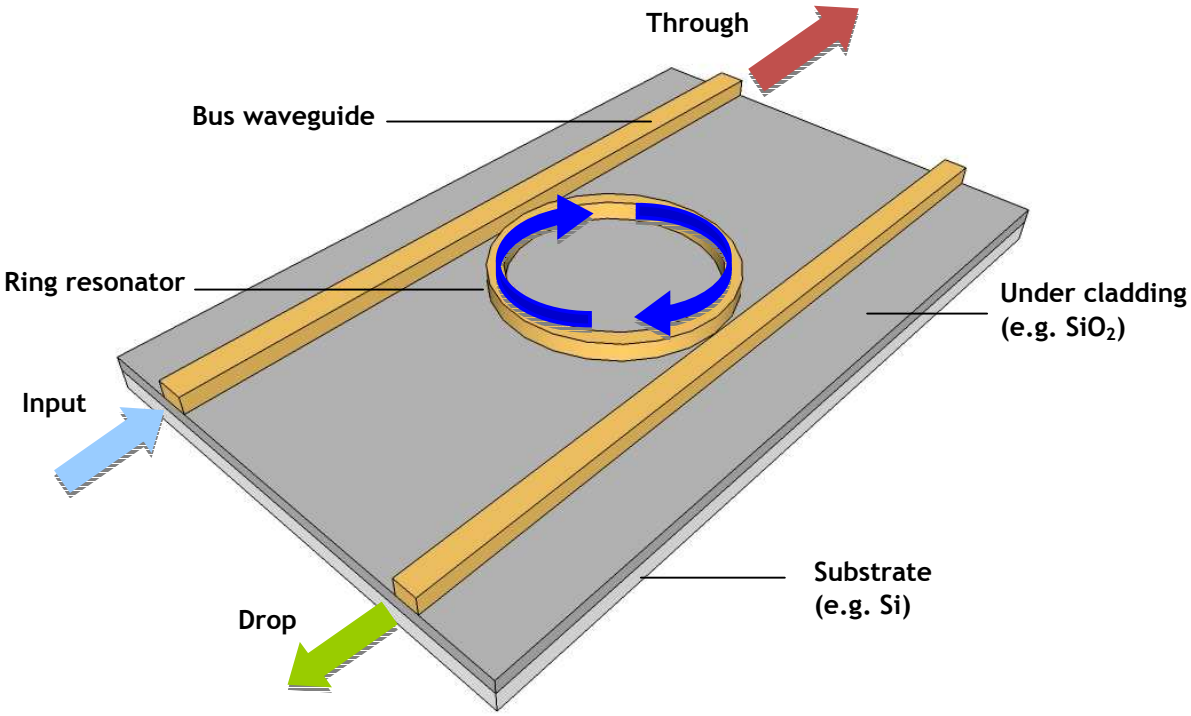

Figure 2.1: Schematic diagram of the microring resonator in 3D image. The arrows show the direction of propagated light inside the straight bus waveguide and resonance coupled circulating light inside the microring structure. Input (light blue) light is injected from the cleaved facet bus waveguide, the light is coupled and circulating inside (blue) the ring resonator, and coupled out to 'through' (red) and 'drop' (green) port.

The mode operation of the device in **Figure 2.1** can be understood in phenomenological term as follows; light is injected into the input bus waveguide when it reaches the narrow gap adjacent to the ring, a certain fraction (κ_1) of the light will be coupled into the ring resonator structure. This then circulates inside the ring resonator structure before a fraction (κ_2) of the light couples back out into the drop port waveguide. Another fraction of the circulating light will also couple back out into the input bus waveguide. Light coupled from the bus waveguides into the ring will interfere with light already circulating inside the ring. This will be either cause constructive or destructive interference depending on the wavelength (see below). This interference pattern builds up the light intensity inside the microring resonator as the circulating light continuously receives a fraction of light from input waveguide until a steady state is reached where the amount of light coupled in equals the amount of light coupled out into 'through' and 'drop' waveguide (together with scattering losses). Inside the ring resonator, the enhanced field generates constructive superposition and can be exploited in optical biosensing.

In order to generate the constructive superposition of the ring resonator, the wavelength needs to satisfy the resonance condition of;

$$2\pi R n_{eff} = \lambda m \qquad (2.1)$$

where R is the radius of the microring resonator, n_{eff} is the effective refractive index of the ring resonator material, λ is the resonance wavelength and m is an integer representing the mode. Only wavelengths that satisfied Equation 2.1 are coupled into the microring resonator structure whilst other wavelengths are propagated through the bus waveguide and detected on the through port monitor [5][6][8].

2.1.2 Free Spectral Range (FSR)

An important parameter that characterises the microring resonator structure for sensing applications is the free spectral range (FSR). The FSR parameter determines the spacing distance between two resonance peaks of the micro-resonator structure, and it is defined as below: -

$$FSR = \frac{\lambda_{res}^2}{n_{eff}(2\pi R)} \qquad (2.2)$$

where λ_{res} represents the resonance wavelength, n_{eff} is the effective refractive index of the ring resonator and R is the radius dimension of the ring resonator. The $2\pi R$ term is the circumference of the ring resonator structure. Clearly, the FSR value will vary as different regions of the spectrum. A narrow FSR distance will exist at shorter wavelengths, such as in the visible spectrum (at 300 nm - 800 nm) compared to the wider FSR values found at a longer wavelength region (e.g. in the Near Infrared (NIR) region between λ = 800 – 2500 nm). The FSR parameter is illustrated in **Figure 2.2**.

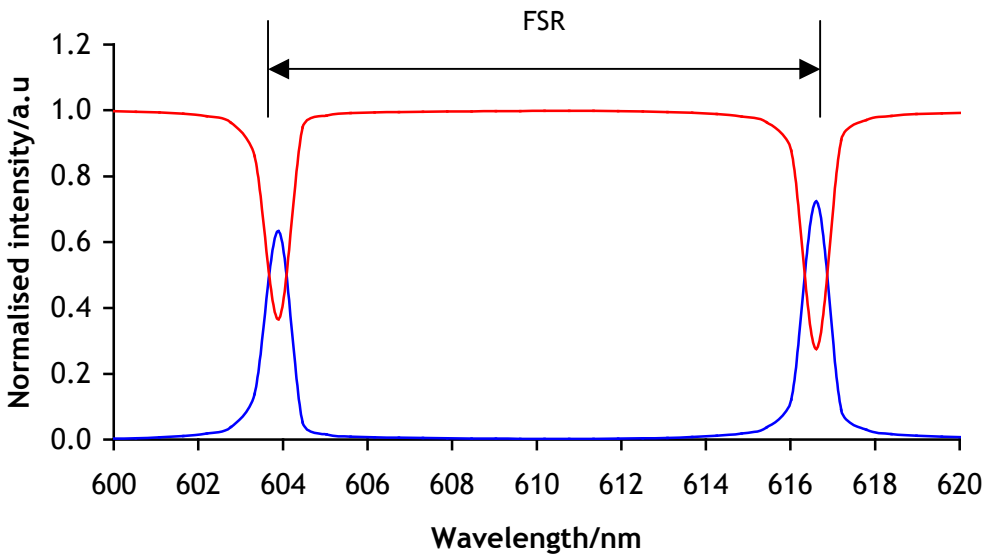

Figure 2.2: The illustration of FSR, spacing distance between two adjacent resonances either from 'through' port (red) or 'drop' port (blue) within the range of λ = 600 - 620 nm. This simulation result is obtained from a 3 μm ring radius, resulting 13.45 nm of FSR.

2.1.3 Effective Refractive Index (n_{eff})

The effective refractive index plays a major role in the micro resonator optical sensing. There are several software packages that are commercially available to calculate the effective refractive index of a system. The effective refractive index is defined as:

$$n_{eff} = \frac{\beta\lambda}{2\pi} \quad \text{or} \quad n_{eff} = \frac{\beta}{k} \qquad (2.3)$$

where β represents the propagation constant, λ is the wavelength (nm), *k* is the reciprocal of wavenumber. In this work, a beam propagation method (BPM) simulation (RSoft Design Group, USA) was utilised as a tool in order to determine the effective refractive index of waveguide structures.

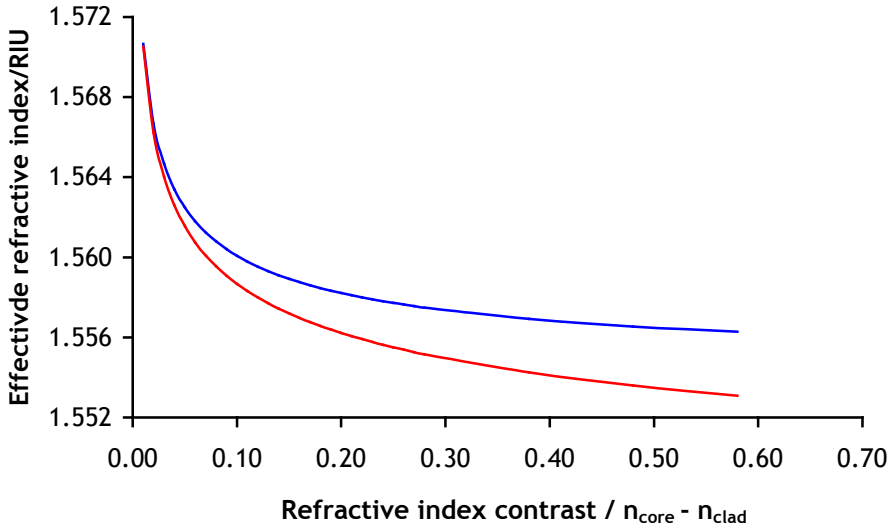

Figure 2.3: The effective refractive index, n_{eff} of the waveguide against the difference refractive index between core (n_{core}) and cladding or surrounding media (n_{clad}). The result obtained when the dimension of waveguide is 1 μm (width) x 1 μm (high). The different effective refractive index for transverse electric (TE) (blue line) and transverse magnetic (TM) (red line) showed an increasing value upon the refractive index contrast.

Figure 2.3 above shows the dependence of the calculated value of effective refractive index upon the refractive index difference between core and cladding or surrounding media. The waveguide core structure refractive index (n_{core}) was set at 1.58 (the value of a SU8 polymer film). Meanwhile, n_{clad} that represented refractive index of the surrounding media was varied from 1.00 to 1.56. The refractive indices of water and bioanalyte (such as proteins for example) were estimated at 1.33 and 1.44 respectively and therefore lie within this range. By using the effective index module in the simulation software, it was observed that the calculated effective refractive index for TE and TM polarization modes were inversely proportional to the refractive index contrast between surrounding media and the core waveguide. In brief, changes in refractive index of the surrounding media will cause a change of the effective refractive index of the waveguide.

This concept can be utilised in biological detection using the optical micro-resonator. Analytes interaction on the surface of the ring resonator waveguide causes the effective index of the ring resonator material to change. This change then has an effect on the resonance wavelength peak position. According to Equation 2.1, since the ring radius parameter and mode number integer have a constant value, the sensing equation can be described as follows: -

$$\frac{\Delta\lambda}{\lambda} = \frac{\Delta n_{eff}}{n_{eff}} \qquad (2.4)$$

where $\Delta\lambda$ is the resonance wavelength shift or displacement; λ is the resonance wavelength for a particular mode; Δn_{eff} is the effective refractive index changes and n_{eff} is the effective refractive index of the ring resonator structure[9]. According to Equation 2.4, the resonance wavelength shifts linearly, dependent on changes in the effective refractive index changes of the ring resonator structure. These shifts in wavelength can be detected using an optical spectrum analyser (spectrophotometer) coupled to the output waveguide.

2.1.4 Evanescent Field Penetration Depth

When the light propagates through a waveguide by TIR, the different refractive index at the dielectric surface boundaries generates an evanescent field. The intensity of this field decays exponentially with the increasing distance from the dielectric surface. This evanescent field is utilized in micro resonators to achieve the resonance wavelength coupling at particular gap spacing. At the same time the evanescent field is exploited in sensing. The evanescent field generated depends on the incident angle, refractive index difference and the wavelength. The equation for evanescent field decay penetration and penetration depth[8] is as described as follows:-

$$I_{(z)} = I_{(o)} e^{-\frac{z}{d}} \qquad (2.5)$$

where $I_{(z)}$ is the intensity at the perpendicular distance z from the surface, $I_{(o)}$ is the intensity at the interface and *d* is the penetration depth. While the penetration depth is described as: -

$$d = \frac{\lambda_o}{4\pi\left(n_{(1)}^2(\sin\theta)^2 - n_{(2)}^2\right)^{1/2}} \qquad (2.6)$$

where λ_o is the incident wavelength, $n_{(1)}$ is the refractive index of the waveguide (at higher value), $n_{(2)}$ is the refractive index of the medium (surrounding media) and θ is the incident angle where the condition $\theta_c < \theta < 90^o$ is satisfied. According to Equation 2.6 above, the evanescent penetration depth (d) is directly proportional to the incident wavelength when the TIR condition is satisfied.

2.2 Simulation

As an initial step, prior to the physical fabrication of devices as described in subsequent chapters, it is crucial to perform simulations of designs using modelling software in order to predict the behaviour of a device. Several design parameters can be then optimised to meet specified criteria before fabrication of real devices is conducted. In this chapter, a number of simulations are illustrated to show the relationship between the designs, theoretical calculations and output results. One of the main sources of propagation losses in a curved waveguide configuration (e.g. a ring or disk) is associated with the 'leakage' of light due to curvature (bending) of the waveguide. At a simple level, this can be understood in terms of loss of total internal reflection. In many instances, these bending losses define the shape of structures that can be used. Thus, the main objectives of the simulation are as follows: -

1. To estimate the minimum 'bending' loss of a defined pattern.

2. To characterize and investigate the resonance wavelength behaviour corresponding to different design parameters such as waveguide width, ring radius and gap distance prior to physical fabrication of device.

2.2.1 Introduction

The BeamPROP software (Rsoft Design Group, USA) version 5.1 is a universal simulation package that is capable of computing the propagation of light waves in arbitrary waveguide geometries. This software is closely integrated with the RSoft CAD tool and can be used as the simulation engine for optical device and integrated circuit design. This software incorporates finite-difference BPM techniques for the simulation algorithm, in conjunction with the RSoft graphical user interface (GUI) for device layout and simulation study. This software offers features such as parameter sweeping and graphical display of parameters of interest for analysis.

2.2.1.1 Bending Loss Simulation

The main objective for this aspect of the study was to determine the minimum bend radius that can be used in the ring resonator geometry (see **Figure 2.2**) in order to reduce the losses of the propagated light to an acceptable value (see later). The simulated structure consists of a curved waveguide with a variable radius, preceded by a straight section (see **Figure 2.4**).

In the RSoft CAD window, the variable parameters such as free space wavelength, background index and index difference are set. The defined variables the drawing geometry is as follows: -

Table 2.1: Defined parameters of the simulation process.

Variable	Value	Comment
Linear input (Lin)	*300 nm*	Length of input waveguide
Radius (r)	*1000 nm*	Radius curvature of arc
Length of bend	*2πr x angle (°)/360*	Length of the arc segments and the factor *2πr* x Angle (°)/360 is present because the variable angle is in degree
Background index	*1.46*	Refractive index value of background (silica = 1.46)
Index difference	*0.12*	Different value of refractive index of waveguide
Free space wavelength	*0.633 μm*	Injecting wavelength in micron

Initially, the direct beam propagation method was used to simulate the actual curved waveguide device. However, when performing the direct simulation of curved waveguides with large angles, this method was unstable. To overcome this problem, a simulated-bend method was used. The simulated-bend method has been verified to be more precise when the radius of curvature (r) was greater than the width (w) of waveguide [19].

Indeed it was found that the results for both the direct and simulated bend simulation were similar. The advantage with simulated-bend method was it could be used with very large radius bends. For an example, the simulated-bend method can accommodate bends of up to 90° angle compared to the actual bend method that can only accommodate a 20° bend. With the minimum plotting features in the simulated-bend method, the simulation time can be significantly reduced even when the scan parameter functions are used. Several parameters such as the width of the waveguide and free space wavelength were simulated to investigate the behaviour of the bending structure. However, this simulation was unable to consider the parameters such as scattering, absorption and insertion losses that also determine the propagated light inside the bending structure.

The scan results were plotted to gain an impression of the influence of parameter changes on the output of a candidate device design (see **Figure 2.4**). The refractive index of the structure and surrounding media were kept constant at 1.58 and 1.00 respectively.

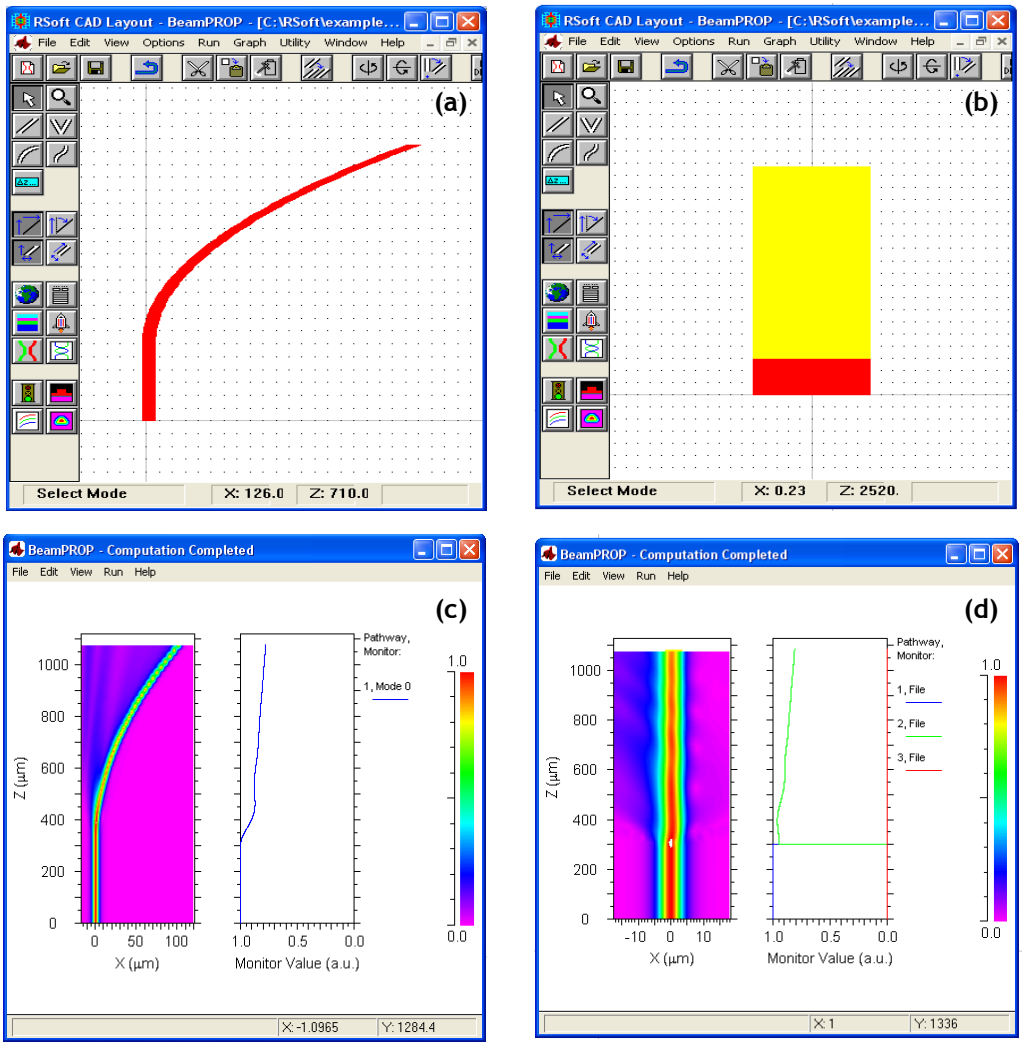

Figure 2.4: Bending losses simulation by using Rsoft CAD BeamPROP software: (a) The actual bend features by using actual arc bend; (b) simulated-bend method with straight position taper; (c) simulation result of actual arc bend method and; (d) simulation results obtained by using simulated-bend method.

For example, **Figure 2.5** illustrates the normalised intensity at the output of the waveguide corresponding to different waveguide widths and increasing bending radius from 10 μm to 500 μm. The simulations were performed at λ = 633 nm to represent a visible wavelength, commonly available as a cheap laser source. Generally, the normalised output value increased exponentially as the radius increases from 0 to 30 μm. The output reaches the maximum transmission (i.e. minimal bending loss) at a radius of 100 μm. From the simulation graph when the width of the waveguide is beyond 0.2 μm, in order to achieve 90% of the output transmission, the minimum bending radius that can be utilised was approximately 40 μm.

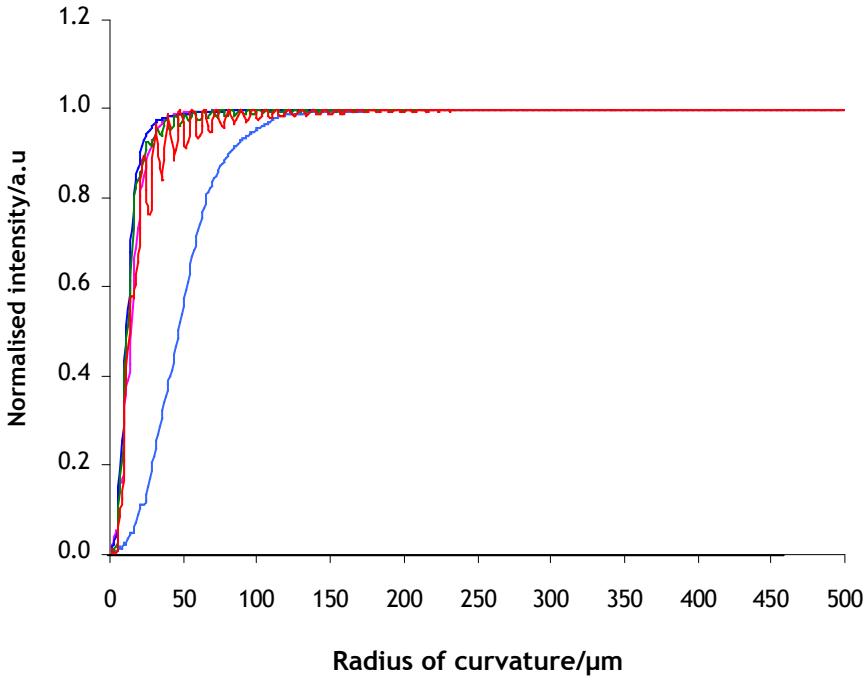

Figure 2.5: Simulation result from the output monitor value at different waveguide widths against the increasing value of the bending radius. The input wavelength was set at λ = 633 nm to represent the visible wavelength. Various dimension of width such as 0.2 μm (light blue line), 0.4 μm (magenta line), 0.6 μm (blue line), 0.8 μm (green line) and 1.0 μm (red line) were simulated.

Similar simulations were performed for λ = 1550 nm, to reflect the NIR region response. **Figure 2.6** illustrates the simulation result for output waveguide response when the bending radius was increased from 0 to 200 μm. The input wavelength was set at λ = 1550 nm and the refractive index parameter was kept constant at $n_{SU\text{-}8}$ = 1.58. Here it was found that the output transmission was very low intensity for waveguide widths of 0.4 μm and 0.2 μm. This suggests that more light can couple out from the narrow structure into the surrounding media. The normalised output intensity that resulted in 50% of intensity being transmitted consisted of 0.8 μm and 1.0 μm widths with bending radii of 37 μm and 40 μm respectively. Note, the smaller width waveguides suffered stronger attenuation, as the ring radius was decreased.

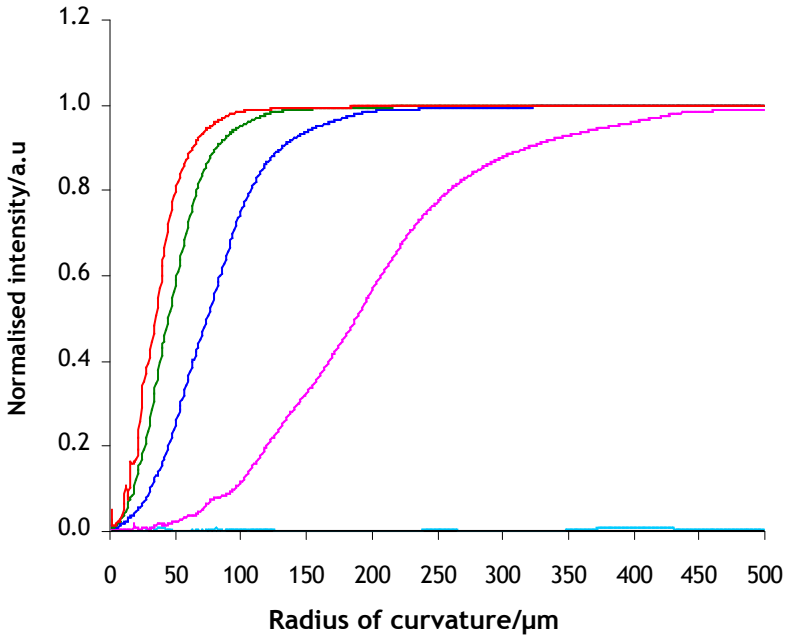

Figure 2.6: Comparison of simulation results from the output monitor upon the increasing value of the bending radius. The simulation is performed at width dimension of 0.2 μm (light blue line), 0.4 μm (magenta line), 0.6 μm (blue line), 0.8 μm (green line) and 1.0 μm (red line). The free space wavelength was set at λ = 1550 nm, to represent the NIR region.

The comparison between of λ = 633 nm and λ = 1550 nm at different width of waveguide is showed in **Figure 2.7**.

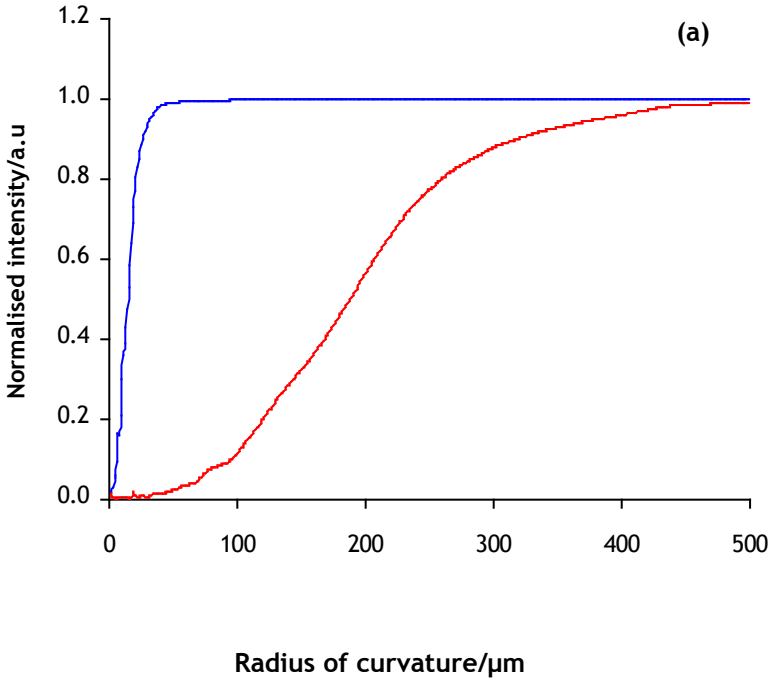

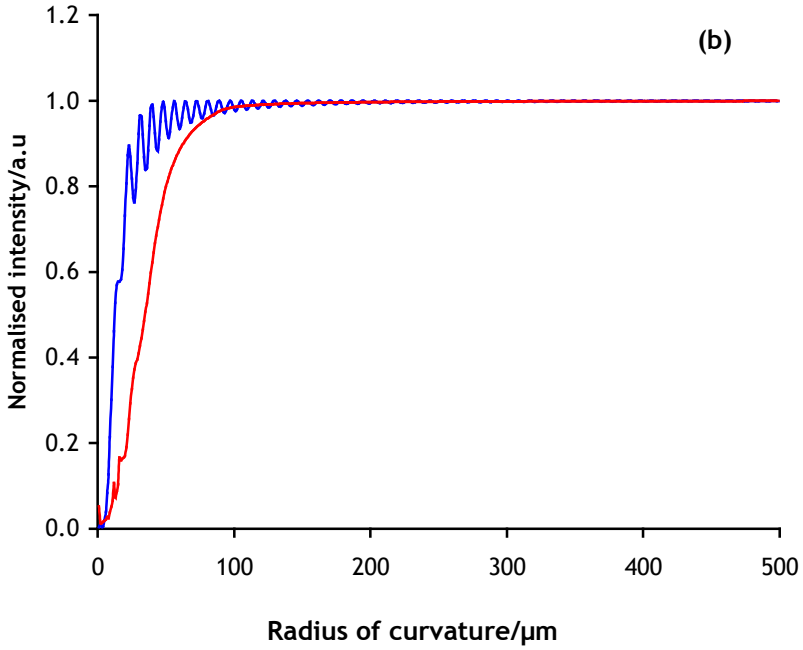

Figure 2.7: Comparison of simulation results for output monitor value/a.u between the wavelengths of λ = 633 nm (blue line) and λ = 1550 nm (red line) with (a) 0.4 μm of waveguide width and (b) 1.0 μm of waveguide width.

Figure 2.7 shows a comparison at 633 nm and 1550 nm for selected waveguide widths taken from Figure 2.5 and Figure 2.6. For the 0.4 μm waveguide (**Figure 2.7(b)**), the smallest radius of curvature suitable to obtain 90% transmission was approximately 40 μm at 633 nm, while a bending radius of nearly 300 μm is needed for λ = 1550 nm. In order to achieve 50% transmission intensity, the minimum radius of curvature at λ = 633 nm wavelength should be around 40 μm while approximately 200 μm radius can be used for λ = 1550 nm of wavelength. **Figure 2.7(b)** displays the comparison of bending losses against the increasing bending radius for both wavelengths when the waveguide width is 1.0 μm. Here, the normalised transmission intensity reached up to 90% when the bending radii are approximately 35 μm and 68 μm for λ = 633 nm and λ = 1550 nm respectively.

From these simulation results, the radius curvature that gives acceptably low bending losses with minimum bending losses is ~ 35 μm for visible wavelengths and ~ 68 μm in the NIR range.

2.2.1.2 Materials and Methods

The SU-8 (Microchem Corp, USA) actual bending pattern waveguides were fabricated onto Si/SiO_2 (University Wafer, USA) wafer substrates in JWNC cleanroom facilities. Fabrication parameters such as the width of the waveguide (1 μm) were set to be similar to the simulation

parameter. The radius of bending pattern ranged from 10 μm to 200 μm, with the increments of 10 μm. The different radii of the bending structures were tested by using an experimental setup that consisted of a HeNe laser, 5mW (CVIMelles Griot Corp, USA), a lens fiber (Advanced Fiber Products Ltd, UK) and an optical powermeter (Ophir Optronics Ltd, Israel). The bending patterns and experimental setup are illustrated as follow:-

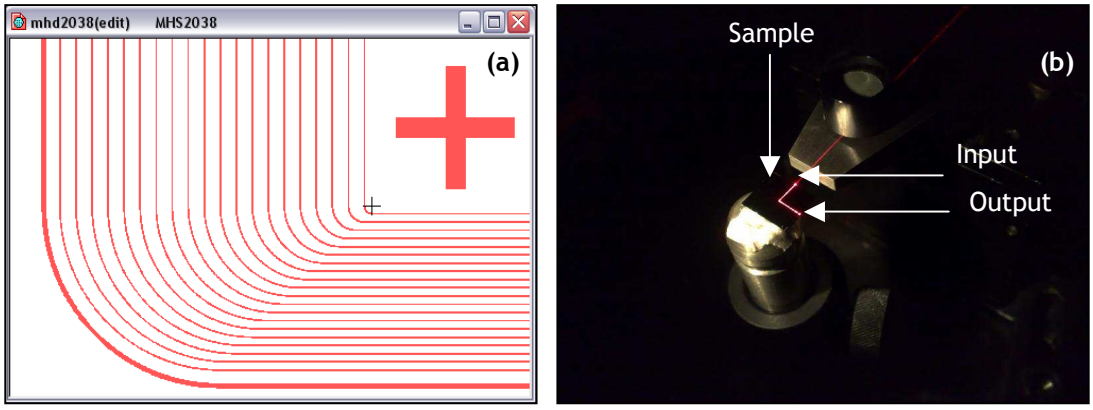

Figure 2.8: Experimental setup for minimum bending losses measurement. (a) Bending radius pattern that was fabricated on the substrate and (b) Experimental setup with X-Y-Z translation stage, SU-8 waveguide on Si/SiO_2 substrate, HeNe laser as illumination source and lens fiber input.

2.2.1.3 Experimental Assessment of Bending Losses

The previous section (2.2.1.1) suggested that acceptably low bending losses required curvature of at least 35 μm (when using λ = 633 nm). However, the simulation method did not take into account real parameters such as temperature, impurities absorption and scattering from the sidewall roughness, all of which are capable of affecting the output transmission. Therefore, laboratory experiments were conducted to investigate influence on the transmission output of the bending radius of fabricated waveguide structures.

The experiment was performed using 3 separately fabricated substrates and the average values were presented in **Figure 2.8**. Both side were cleaved and inspected under the microscope before performing the experiment. The injected light was focused into the input waveguide by using the lens fiber. Then the output power was detected by power meter on the 90° degree side of the substrate (see **Figure 2.8(b)**). Every output (mW) reading from each bending radius pattern was collected and plotted in **Figure 2.9** for comparison with simulated result.

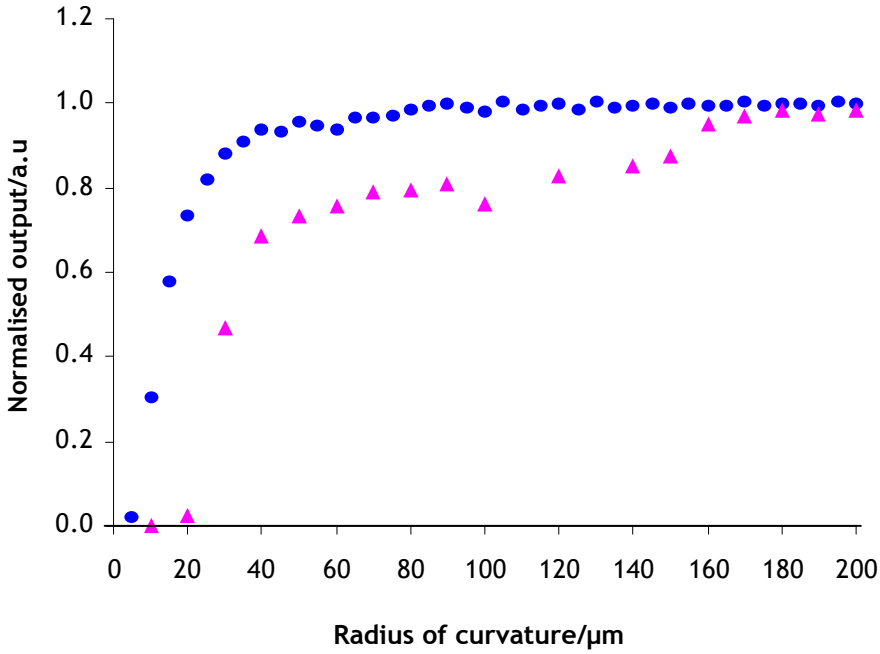

Figure 2.9: Comparison of the average normalised value of the simulation(●) and experiment(▲) results upon the increasing radius of curvature.

Figure 2.9 illustrates the output signal of both simulation and experimental results as a function of the radius of curvature, when using a λ = 633 nm HeNe laser as a source. From the experimental observations, the transmission values were lower than anticipated from the simulation results. This was most likely to be because of sidewall roughness scattering, insertion losses during the end-butt coupling and unwanted debris on top of the waveguide itself. Not withstanding these effects, the trend of the experimental results was almost identical to the simulation result; at 40 μm geometries, the experimental result shows a transmission of 0.7 or 70% of the maximum value (i.e. the transmission when r > 160 μm) compared to the simulation result that had reached almost 0.9 or 90% for this radius of curvature.

In brief, according to the simulation and experimental results obtained above, it was found that the minimum bending radius that could be used was approximately 30 - 40 μm. Thus, a 40 μm radius was selected to be utilised throughout this work in order to minimise the bending losses of the propagated light. In order to characterise the behaviour of the resonance wavelength response of different designs, another commercial finite-difference time-domain (FDTD) software (Lumerical Solutions, Canada) was used that allowed parameters including ring radius, waveguide width, gap distance and refractive index of surrounding media to be varied. The results and discussion for standard ring resonator configurations are given in **Appendix A.2.1.**

2.3 Single and Double-cascaded Resonators

2.3.1 Introduction

In the optical micro resonator biosensing principle, the biological interaction is measured by monitoring the resonance wavelength peak shift. Different configurations (**Figure 2.10**), which were considered, include the structures below:

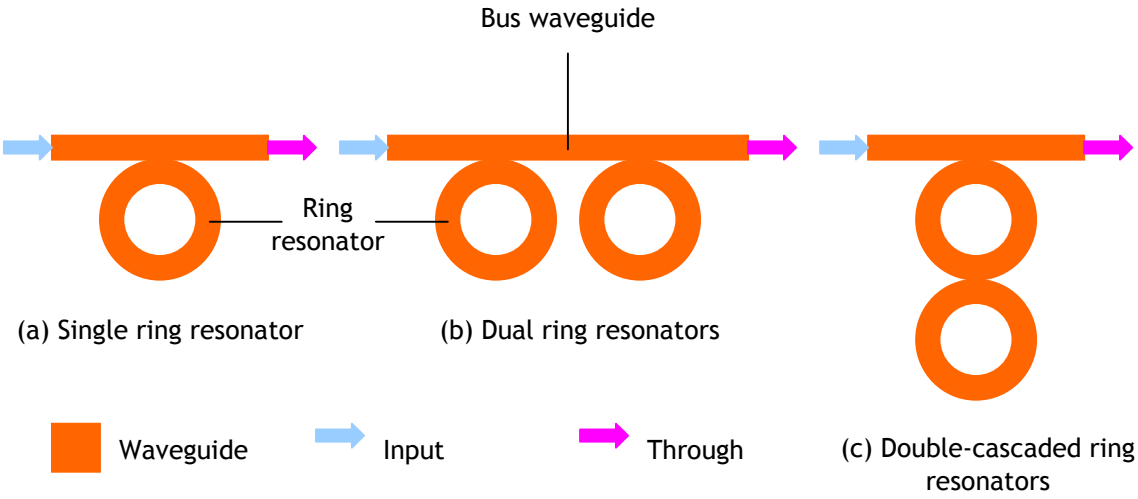

Figure 2.10: Schematics of gapless ring resonator configurations at (a) single ring resonator with 'input' and 'through' port; (b) Dual ring resonators arrangement where two identical resonators are located horizontally next to each other between input and through channel and (c) double-cascaded ring resonators, were arranged next to each other between 'input' and 'through' port.

Usually, the spectroscopic output response for a micro-resonator contains a periodic series of peaks[11] of uniform amplitude as shown in **Figure 2.11**. Within a narrow wavelength range, the spacing between peaks is similar. Thus, it is crucial to make sure that the shift of the resonance peaks series that occurs when the refractive index around the resonator changes (see **Section 2.1.3**), can be distinguished from the original pattern of the peaks. Therefore, sufficient FSR spacing is needed in order to confidently measure the resonance wavelength shift. When using the visible wavelength, devices with a relatively larger radius show the narrow FSR constrain the degree of wavelength shift that can be measured. A wider FSR can be achieved by reducing the radius, but in this case the bending losses would increase excessively.

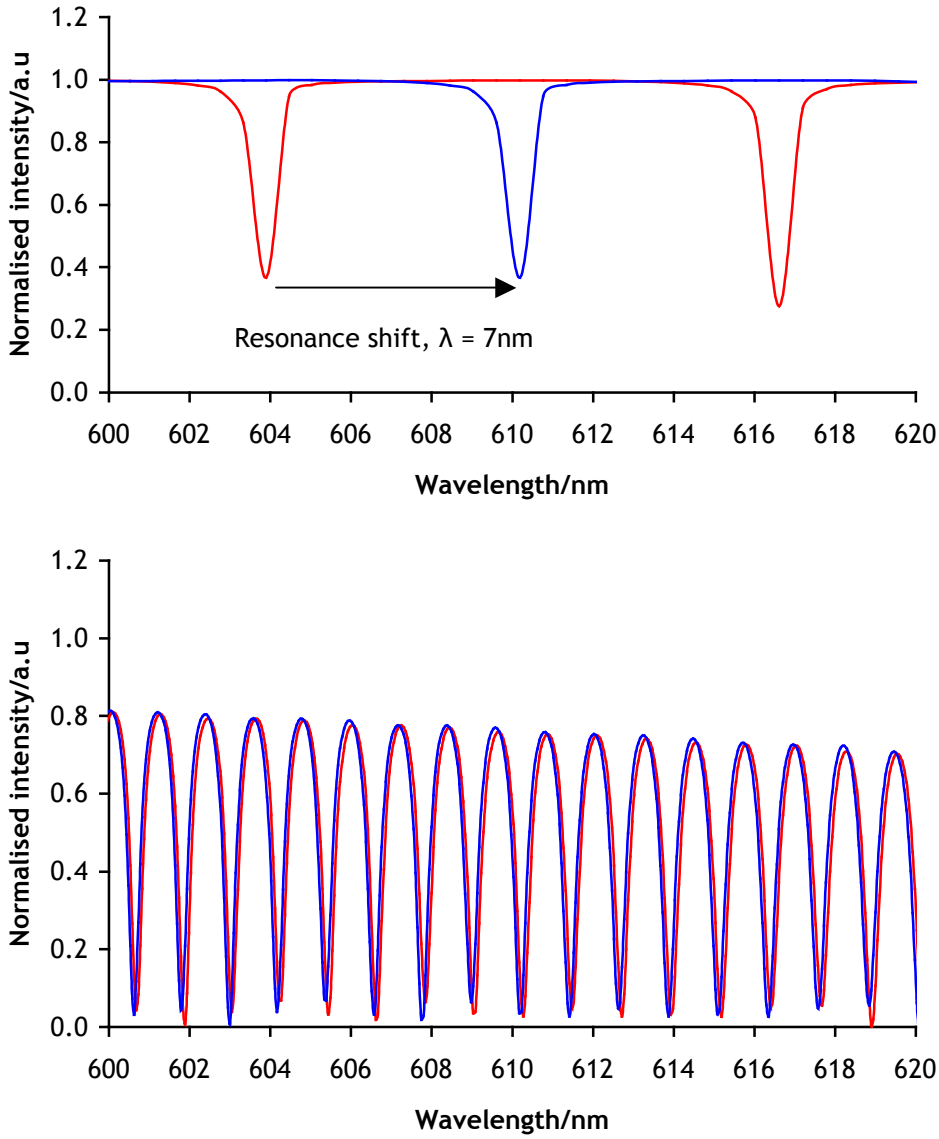

Figure 2.11: Both of the resonance wavelength shift occurred when the refractive index of surrounding media is altered from air, n_{air} = 1.00 (red line) to water, n_{water} = 1.33 (blue line) at different radius dimension. (a) The ring radius is 3 μm, given the FSR value of 13.45 nm and (b) The ring radius at 30 μm, resulting the FSR value of 1.16 nm. The wider original FSR pattern demonstrates straightforward resonance shift detection compared to narrow FSR pattern, seem to be overlapped to neighbouring resonance wavelength.

2.3.2 Discussion

In order to obtain a wider FSR spacing without sacrificing the minimum-bending radius, the vernier effect[5][13] was applied. The vernier phenomenon occurs when two different resonance patterns interact with each other. Since the resonance wavelength pattern consists of periodic peak of amplitude, the combined response from two resonance patterns where the peaks spacing is slightly different results in the possibility of certain features of the output spectra being enhanced. When resonance wavelengths coincide. Meanwhile, at other non-coinciding resonance wavelengths features are suppressed (see **Figure 2.12**).

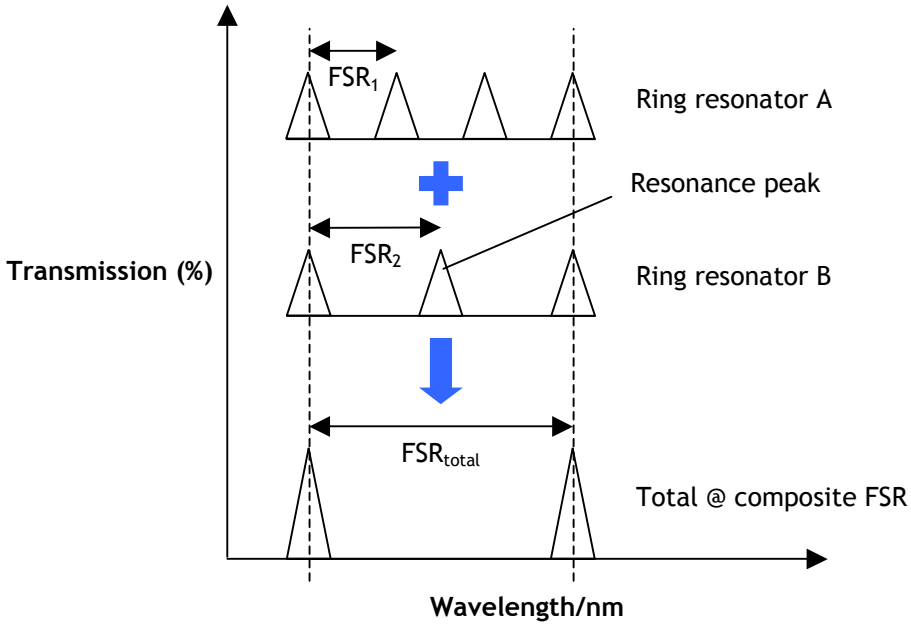

Figure 2.12: Illustration of vernier principle when two different FSR interact. The radius for ring resonator A structure is larger than the radius of ring resonator B. These structures result in a narrow FSR value for ring resonator A and wider FSR value for ring resonator B. When both structures were arranged in a cascaded position, the composite FSR is observed.

By utilising this technique, a wider FSR can be achieved without acquiring higher bending losses through having to make rings of smaller radius. Several common techniques that have been applied to obtain wider FSR value by exploiting the vernier effect including asymmetrical arrays[14], series-coupled racetrack resonator[15], parallel-cascaded[16], vertically triple coupled[17] and double-ring[13,18].

In this work, the double-ring technique was chosen to increase the FSR value within visible wavelength range. Calculation of the anticipated resonance patterns was performed using

SigmaPlot 8.0 (Systat Software Inc, USA) software and single resonator simulations carried out with FDTD Solution Lumerical software. The double-ring technique consisted of two ring resonators with different radii located between the input and drop port waveguides[13] as shown in **Figure 2.13**. Each of the rings supported different resonance patterns. The expanded FSR value as a result of vernier effect is given by the following equation[5][13]: -

$$FSR_e = N_a.FSR_a = M_b.FSR_b \qquad (2.7)$$

where FSR_e is total or composite FSR value and N_a and M_b have to be integers. When Equation (2.7) was satisfied, the vernier effect causes enhancement of selected resonance peaks in both resonators and the suppression of the other intervening peaks. As a result, a wider FSR value can be obtained. In the work described in this thesis, one of the resonators was selected to be 40 μm radius to avoid the extensive bending losses (as informed by section 2.2). The other resonator radius dimension was calculated, after deciding a desired specific FSR value (FSR_e) and inserting this obtained using Equation (2.7). For example, from the calculation, the composite radius dimension for resonator A and resonator B is 40.000 μm and 45.758 μm respectively; they have FSRs of at 1.2355 nm and 1.1111 nm of FSR respectively for 700 nm. This arrangement gives an overall FSR value of approximately 10 nm. These calculations have been made for ring resonator structures and similar results were also obtained for disk resonator structures.

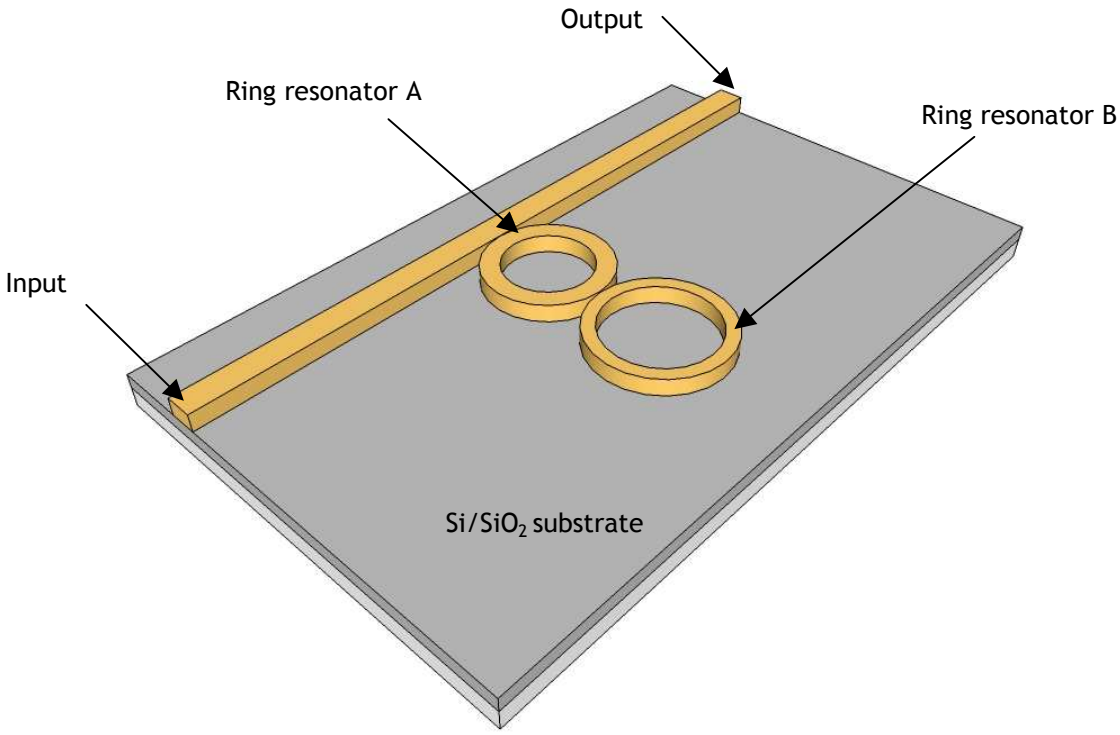

Figure 2.13: The schematic diagram of double-cascaded gapless ring resonators. This arrangement was set to overcome the narrow FSR in the visible wavelength region. Resonator A and resonator B were set at 40.000 μm and 45.758 μm respectively.

Figure 2.13 illustrates the configuration of double-cascaded gapless ring resonator to increase the FSR value. In order to minimise the sidewall roughness that occurs on the inside of the inner boundary of the ring, the ring structure was replaced by the disk geometry and gapless spacing was utilised in the physical fabrication process (discussed in **Chapter 3**).

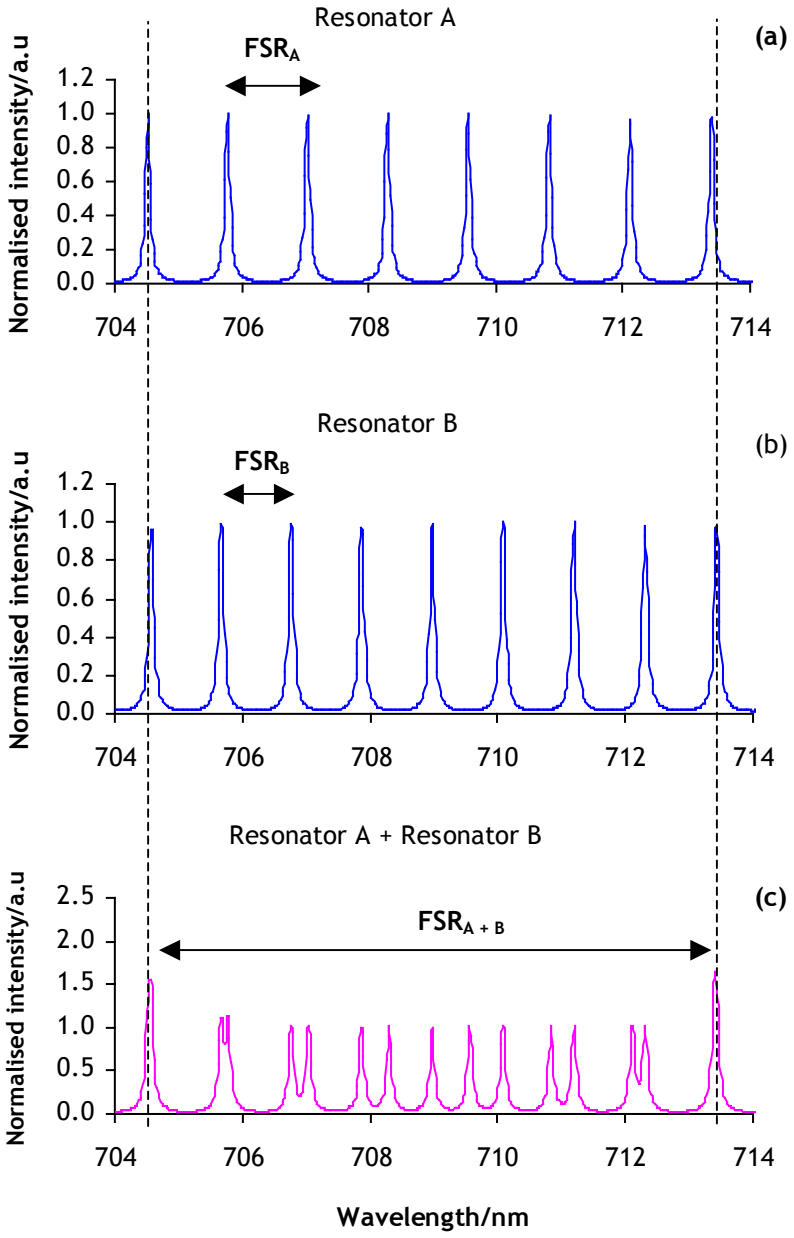

Figure 2.14: The resonance wavelength pattern from the output waveguide within the range of λ = 704 – 714 nm. (a) The radius size for resonator A was at 40.00 μm; (b) The radius size for resonator B was at 45.758 μm and (c) Combination of two resonators to form a double-resonator.

Figure 2.14 shows the normalised intensity of the resonance wavelength pattern obtained from different ring radius and double-ring resonator structure. **Figure 2.14(a)** demonstrates the output response with the FSR value of 1.26 nm when the radius was set at 40.00 μm. In contrast, **Figure 2.14(b)** exhibits the FSR value of 1.08 nm at the radius of 45.758 μm. Meanwhile, **Figure 2.14(c)** shows the output response from the combination of two different radii, which caused the Vernier effect and the FSR value was increased to 8.86 nm. The composite FSR varies with the wavelength and the composite FSR is reduces from 8.86 nm at (λ = 700 nm) to 6.44 nm (approximately λ = 600 nm).

As a proof of concept, the double-cascade ring resonator with ring radii at 40 μm and 45.758 μm was physically fabricated and characterised. These results indicated that, the vernier effect calculation accurately predicted the expanded FSR in a fabricated device containing two rings of slightly different radius.

2.4 Summary

In conclusion, the general theories of micro resonator and related parameters have been discussed in this chapter. Simulations using the FDTD approach were performed in order to gain an overview of the device behaviour against the related parameters. The gapless structures demonstrated promising potential that could be exploited and fabricated to overcome the difficulty in a sub-micron gap device. An acceptable bending loss was determined to be in structures of at least 40 μm radius and a significant resonance shift was also found to occur when the medium was changed from air to water, but the resonance patterns for a single ring or disk structure were difficult to distinguish. Thus a cascaded, or vernier, structure was designed in order to generate a more complex resonance pattern.

References

[1] S. Z. Deng, W. Cai, and V. N. Astratov, "Numerical study of light propagation via whispering gallery modes in microcylinder coupled resonator optical waveguides," *Optics Express*, vol. 12, pp. 6468-6480, 2004.

[2] K. C. Zeng, L. Dai, J. Y. Lin, and H. X. Jiang, "Optical resonance modes in InGaN/GaN multiple-quantum-well microring cavities," *Applied Physics Letters*, vol. 75, pp. 2563-2565, 1999.

[3] F. Vollmer, D. Braun, A. Libchaber, M. Khoshsima, I. Teraoka, and S. Arnold, "Protein detection by optical shift of a resonant microcavity," *Applied Physics Letters*, vol. 80, pp. 4057-4059, 2002.

[4] A. Ramachandran, S. Wang, J. Clarke, S. J. Ja, D. Goad, L. Wald, E. M. Flood, E. Knobbe, J. V. Hryniewicz, S. T. Chu, D. Gill, W. Chen, O. King, and B. E. Little, "A universal biosensing platform based on optical micro-ring resonators," *Biosensors & Bioelectronics*, vol. 23, pp. 939-944, 2008.

[5] Heebner, J., Grover, R. and Ibrahim T.A. Optical Microresonators: Theory, Fabrication and Applications; Springer Series in Optical Sciences; Springer-Verlag London, U.K 2008

[6] B. E. Little, S. T. Chu, H. A. Haus, J. Foresi, and J. P. Laine, "Microring resonator channel dropping filters," *Journal of Lightwave Technology*, vol. 15, pp. 998-1005, 1997.

[7] T. A. Ibrahim, W. Cao, Y. Kim, J. Li, J. Goldhar, P. T. Ho, and C. H. Lee, "All-optical switching in a laterally coupled microring resonator by carrier injection," IEEE Photonics Technology Letters *IEEE Photonics Technology Letters*, vol. 15, pp. 36-38, 2003.

[8] K. Okamoto, Fundamental of Optical Waveguide (Second Edition), Academic Press: London, U.K, 2008.

[9] S. Y. Cho and N. M. Jokerst, "Polymer microrings integrated with thin film InGaAs MSM photodetectors for Sensor-on-a-Chip applications," 2006 International Conference on Indium Phosphide and Related Materials Conference Proceedings, pp. 222-225446, 2006.

[10] Rsoft BeamPROP™ 5.1: Tutorial 2 – Simulating S-Bend. Available: BeamPROP™ User Guide (1993-2003).

[11] B. E. Little, S. T. Chu, W. Pan, D. Ripin, T. Kaneko, Y. Kokubun, and E. Ippen, "Vertically coupled glass microring resonator channel dropping filters," *IEEE Photonics Technology Letters*, vol. 11, pp. 215-217, 1999.

[13] K. Oda, N. Takato, and H. Toba, "A Wide-Fsr Wave-Guide Double-Ring Resonator for Optical Fdm Transmission-Systems," *Journal of Lightwave Technology*, vol. 9, pp. 728-736, 1991.

[14] G. Griffel, "Vernier effect in asymmetrical ring resonator arrays," *IEEE Photonics Technology Letters*, vol. 12, pp. 1642-1644, 2000.

[15] R. Boeck, N.A.F. Jaeger, N. Rouger, and L Chrostowski, "Series-coupled silicon racetrack resonator and the Vernier effect: theory and measurement," *Optics Express*, vol. 18, no.24, pp. 25151-25157, 2010.

[16] R. Grover, V. Van, T. A. Ibrahim, P. P. Absil, L. C. Calhoun, F. G. Johnson, J. V. Hryniewicz, and P. T. Ho, "Parallel-cascaded semiconductor microring resonators for high-order and wide-FSR filters," *Journal of Lightwave Technology*, vol. 20, pp. 872-877, 2002.

[17] Y. Yanagase, S. Suzuki, Y. Kokubun, and S. T. Chu, "Box-like filter response and expansion of FSR by a vertically triple coupled microring resonator filter," *Journal of Lightwave Technology*, vol. 20, pp. 1525-1529, 2002.

[18] S. Suzuki, K. Oda, and Y. Hibino, "Integrated-Optic Double-Ring Resonators with a Wide Free Spectral Range of 100 Ghz," *Journal of Lightwave Technology*, vol. 13, pp. 1766-1771, 1995.

[19] Rsoft Design Group [Online]. Available: http://www.rsoftdesign.com/

[20] MicroChem Corp, USA [Online]. Available: http://www.microchem.com/

[21] University Wafer, USA [Online]. Available: http://www.universitywafer.com/

[22] CVI Melles Griot Corp, USA [Online]. Available: http://www.cvimellesgriot.com/

[23] Advance Fiber Products Ltd, UK [Online]. Available: http://www.afpgco.com/

[24] Ophir Optronics Solutions Ltd, Israel [Online]. Available http://www.ophiropt.com/

[25] Lumerical Solution Inc, Canada [Online]. Available: http://www.lumerical.com/

[26] Systat Software Inc, USA [Online]. Available: http://www.sigmaplot.com/

CHAPTER 3

Material and Fabrication

Introduction

In this chapter, the materials and processes that were used in the fabrication of polymer micro resonator sensors are described. This includes the extensive optimisation of the fabrication process in order to improve the yield of SU-8 polymer waveguides. The chapter begins with brief description of the general fabrication steps, the SU-8 polymer material and the design tool. For drawing the fabrication pattern, electron beam lithography patterning, the

general and specific physical processes involved in fabrication. At the end of the chapter, scanning electron microscopy (SEM) images of the final devices are presented.

3.1 General Fabrication Procedure

The general sequence of device fabrication is explained (see **Figure 3.1**) starting from the design process to the construction of an actual device that was utilised in an experiment. There were three separate environments where this research was performed: (1) In the cleanroom facilities, cleaning of the substrates, spinning the SU-8 resist, photolithography and resist development process were carried out; (2) In the laboratory, surface modifications of SU-8 surface, fabrication of microfluidic channels and protein immobilization protocol were conducted and finally (3) in the optical laboratory where an experimental setup was used to characterize and measure the output signal from the sample (discussed in **Chapter 4**).

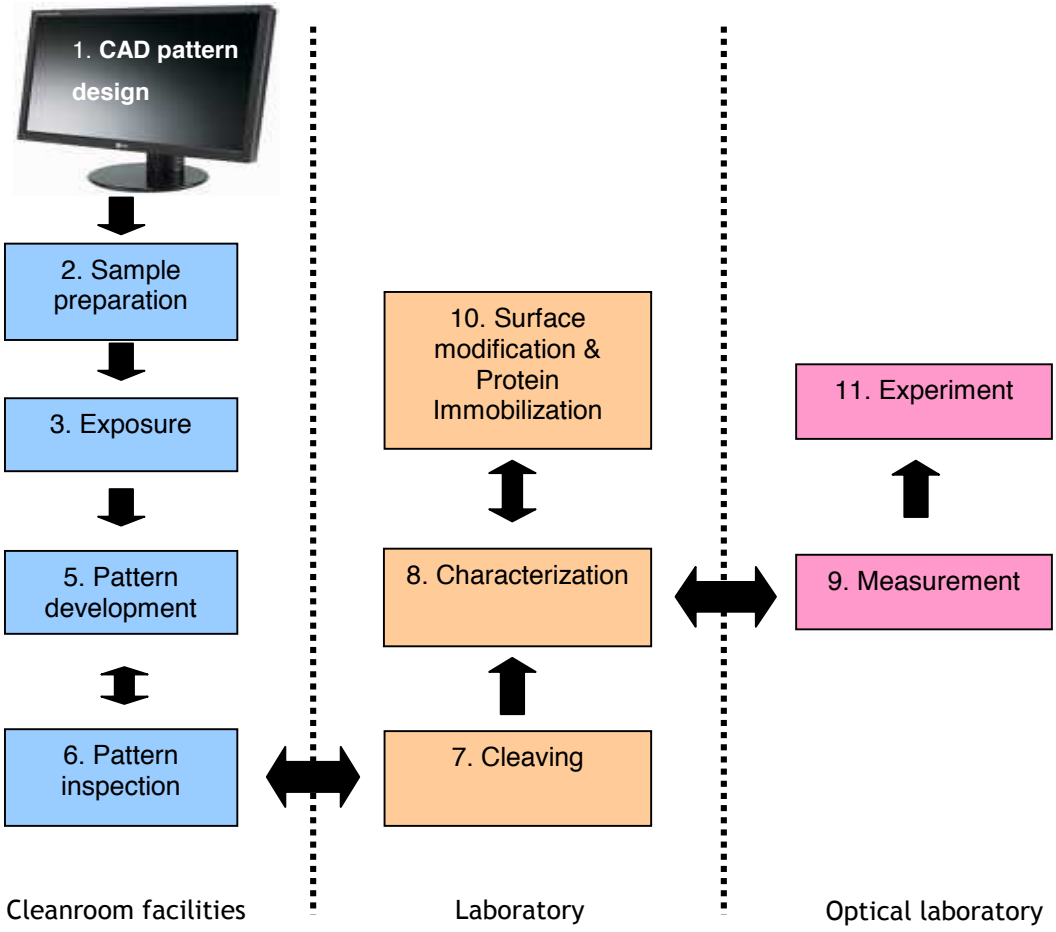

Figure 3.1: General procedure and cycle of device fabrication and measurement. Waveguide inspection is usually performed at every step of fabrication processes to make sure that the substrate is reliable for experiment.

3.2 Device Fabrication Process

3.2.1 Materials and Methods

In the fabrication process, SU-8 polymer resist (Microchem Corp, USA) is used to fabricate a polymer waveguide structure. Acetone and isopropyl alcohol (IPA) used for the substrate cleaning process were purchased from Fisher Scientific and Sigma-Aldrich respectively. Microposit 2-methoxy-1-methylethyl acetate (EC solvent) developer was obtained from Shipley European Ltd, UK. SU-8 resist is spun onto the specific dimension of diced Si/SiO_2 (University Wafer, USA) using a programmable spinner (Headway Research Inc., USA). Cleaning and development process were performed under laminar flow hood conditions in the James Watt Nanofabrication Centre, Glasgow University (JWNC) cleanroom. Surface inspection is performed using optical microscopy Leica NM20 (Leica Microsystem, Germany) and Zeiss Axiotron (Zeiss, Germany) were used to check the physical fabricated SU-8 pattern after development processes (the maximum resolution is approximately 200 nm). In order to examine the detail of the fabricated structure until 1.5 nm of resolution, an Hitachi S-4700 scanning electron microscopy (SEM) (Hitachi High-Tech Co., Japan) is used and has a capability of angle tilting up to 60^{o} and it was important for examining a side wall roughness

3.2.2 Fabrication Step

The fabrication of SU-8 polymer resonators pattern consists of several major steps as shown in **Figure 3.2**. Each step is performed in the JWNC cleanroom facilities. For the mask aligner (MA6) (SUSS Micro Tec AG, Germany) equipment, direct procedure was used after several training sessions. However, an electron beam writer (Vistec Lithography Inc, USA) is conducted by a technician, providing with required parameters from the user.

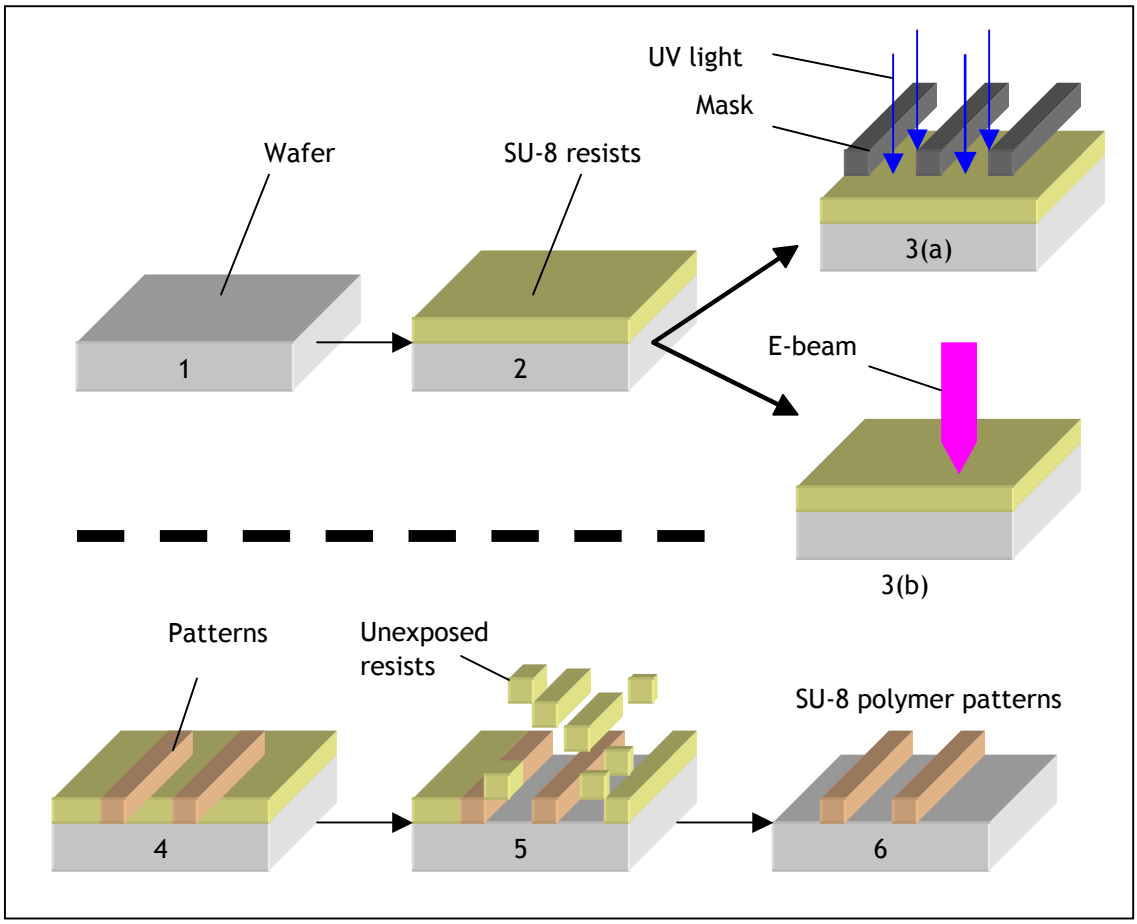

Figure 3.2: Fabrication process: 1. Wafer was cleaned; 2. Resist was spun at 3000 rpm for 30 sec; 3(a) Sample was exposed to UV light with mask plate; 3(b) sample was patterned by electron beam writer (Vistec VB6); 4. Post-exposure bake (PEB) for 2 minutes; 5. Development process with EC solvent for 2 minutes and rinsed with IPA. At this stage, the exposed area will be remained and unexposed area will be dissolved in the EC solvent solution; 6. Samples were placed onto the hotplate for 3 steps of hard bake for 1, 1 and 3 minutes at 65 ^{o}C, 95 ^{o}C and 180^{o}C, respectively.

Silicon wafers from University WAFER Ltd, USA with 3.5µm of oxide layer were cut into (20 x 20 mm) pieces and used as the substrates. Fabrication steps began with designing the waveguide pattern using computer aided design (CAD) software at a desktop computer. The substrates were prepared and SU-8 polymer resist was spun on the diced silicon wafers in the JWNC cleanroom environment. Next, prepared substrates were exposed to ultra-violet (UV) light through a mask or used in direct write EBL process before proceeding to the resist development stage. For development, a specific developer (EC Solvent) was used to dissolve the unwanted resist after exposure. Polymer patterns were inspected using an optical microscope during and after the development process. If the patterns seemed to be under developed, the development process was repeated until a particular pattern was fully defined.

After the development process was completed, the substrates were cleaved so as to give a clean end facet on the polymer waveguide. After cleaving, substrates were examined again under the microscope to ensure that the end faces of the cleaved substrates were cut at 90^{o} had flat end facets for both input and output waveguide coupling. The quality of both flat end facet waveguides was important for good coupling efficiency. The waveguide were then characterised using an experimental setup that consisted of an objective lens, an optical spectrum analyser SPEX 500M (Horiba, Japan), a HeNe laser 5mW (CVI Melles Griot, USA) as an alignment light source and a halogen display or optic lamp 12V, 100W (Osram, Germany) as a broadband light source (discussed in **Chapter 4**). For selected designs, having established that a waveguide had specific characteristic of physical (e.g. flat cleaved facet) and optical properties (e.g. above minimum intensity counts), it was then subjected to the surface modification procedure in order to carry out further experiments and bioanalyte detection.

3.3 Pattern Design

There were a number of steps that had to be performed before the physical fabrication process in a cleanroom. Firstly, Tanner L-Edit Software Version 12.61 developed by Tanner EDA, USA was used to design sample and micro-resonator waveguide patterns (see **Figure 3.2**). This provided an easy approach to enable small changes in design to be effected without needing to re-layout the whole desired structure. Photolithography masks were used to make simple waveguide patterns whereas electron beam lithography (EBL) was used to fabricate the resonator structure. Along with better resolution, EBL allowed iteration of different designs during the optimization process, saving cost and time compared to repetitive mask plate making. Desired patterns, drawn using Tanner L-edit, were converted into graphic design system (GDSII) file for transfer to the EBL tool[1].

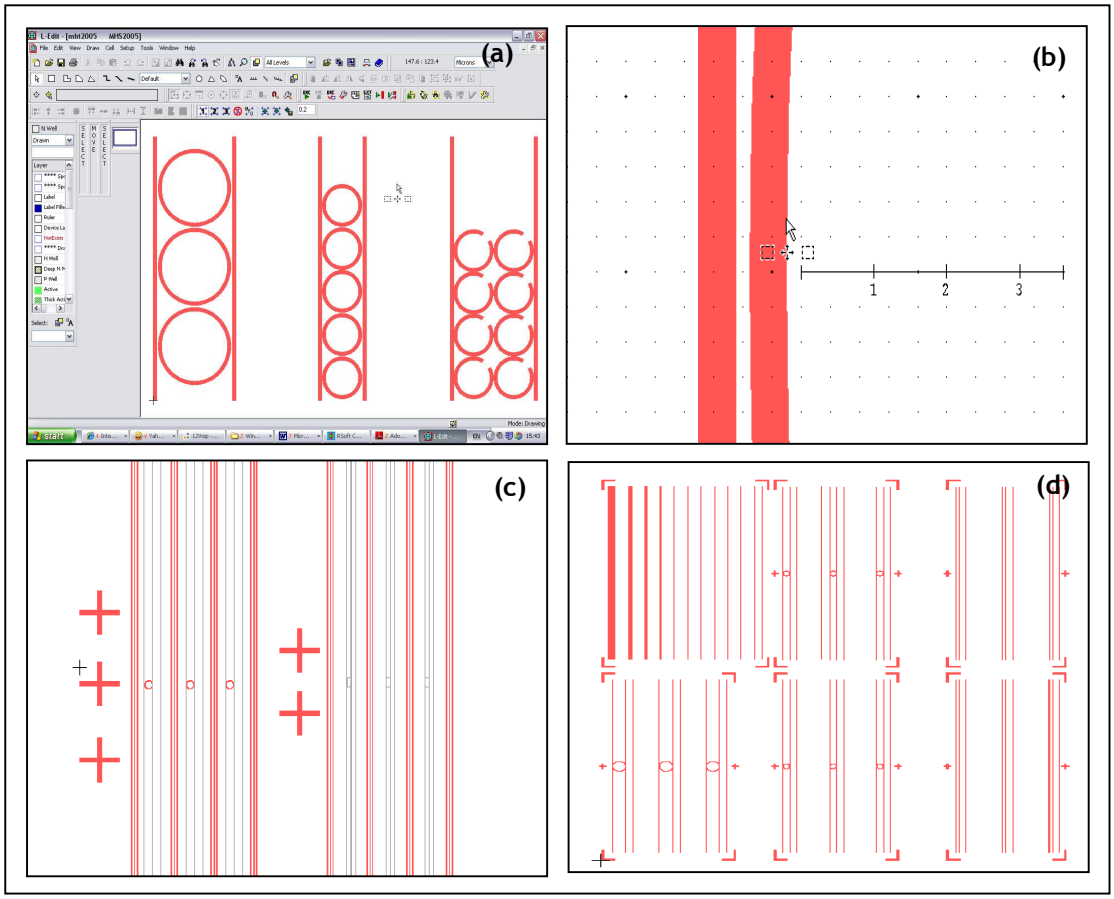

Figure 3.3: Shows the L-Edit CAD Software. a) The control panel and main interface, b) Gap drawing with ruler, c) Duplicate image of a straight waveguide and d) the full pattern of waveguide, ready for GDSII conversion.

3.4 Materials

3.4.1 SU-8

SU-8 polymer resist (see **Figure 3.4**) is a negative photoresist originally developed by IBM Research Zurich Laboratory in 1996. When the resist is exposed to UV light, polymerisation occurs through the acid catalysed cross-linking of the epoxy groups. Since cured SU-8 is chemically and thermally stable[2], SU-8 polymer resist has been used extensively in microelectromechanical systems (MEMS) and micromachining, UV-LIGA, microfluidics channel and rapid prototyping[3-7]. It also has excellent optical properties[8][9][10] that are related to its high refractive index and low scattering losses, making it suitable for waveguide sensor structures [11][12][13]. An advantage of using SU-8 lies in rapid processing and prototyping, especially during the patterning and development, when compared to the silicon or silica-based process. Which may need several fabrication steps including extensive deep dry etching. Importantly, this resist can also be polymerised by exposure to an electron beam (in EBL).

SU-8 solutions are prepared in an organic solvent. SU-8 2 series dissolved in γ-butyrolactone (GBL) from Microchem Corp, USA was used as received. The thickness of resist layer was controlled by the viscosity of its dilution and the spin speed. The SU-8 2 series resist was spun at 3000 rpm for 30 sec; as a result the waveguide structure obtained was ~1μm after development.

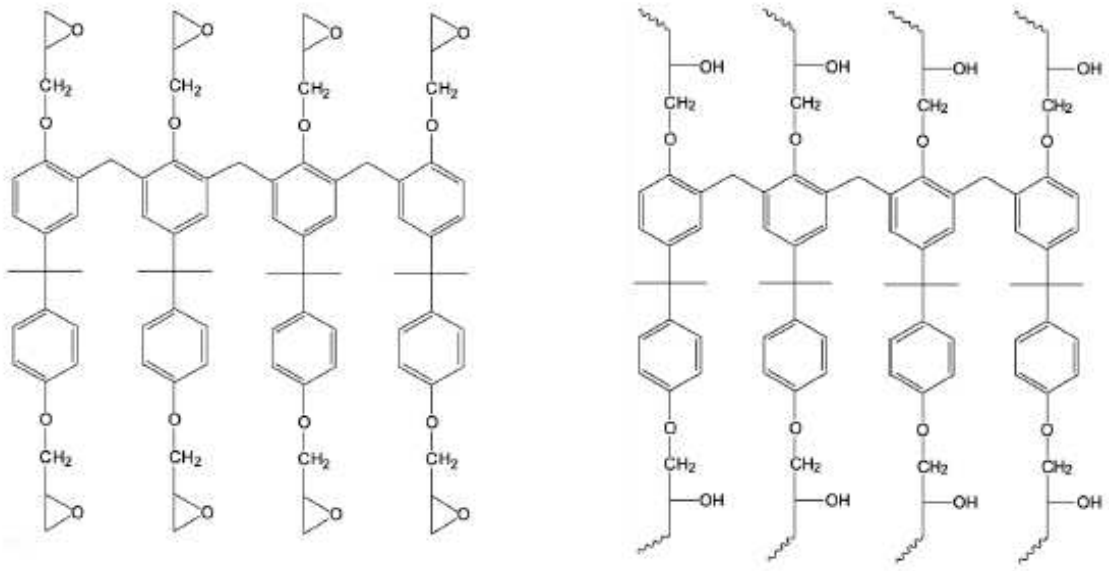

Figure 3.4: The molecular structure of SU-8 resist: - (a) monomer – before crosslinking, (b) polymer – after crosslinking reaction *(Courtesy image Silvan Schmid, 2003)*

3.4.2 Cleaning and Development Chemicals

Acetone and isopropyl alcohol (IPA) that used for substrate cleaning process was purchased from Fisher Scientific and Sigma-Aldrich respectively. Microposit EC solvent developer was obtained from Shipley European Ltd, UK. Cleaning and development process were performed under laminar flow hood conditions in the JWNC cleanroom.

3.5 Lithography

Photolithography and EBL technique were used in order to construct simple and complex SU-8 polymer waveguide structures. Both options were available in the JWNC for device fabrication patterning. They are described in this section and followed by a description of the dose test experiment to obtain suitable fabrication parameters.

The dose test is an important step in any fabrication process based on resists exposure. This step is usually carried out at a preliminary stage prior to device fabrication. The result from

the dose test was used to avoid over-exposure or under-exposure. Dose tests were performed for both lithography tools in the JWNC, namely the mask aligner (MA6) and electron beam writer (VB6). Although a material datasheet provided by MicroChem Ltd. Datasheet guideline doses for EBL sizes still need optimisation due to the different sizes of features, as well as different substrates, developer and equipment used in this project.

3.5.1 Photolithography

The SUSS MicroTec Mask Aligner (MA6) was designed for high-resolution laboratory photolithography and small-scale production. According to the MA6/MA8[15] user manual, substrates up to 6 mm of thickness can be used for photolithography. It has five different programmable exposure modes such as proximity, soft contact, hard contact, vacuum contact and flood exposure. With a ~350 nm wavelength lamp, the resolution capability was approximately 1.5 μm.

The mask plate was fitted into the upper vacuum stage and the substrate was loaded onto the substrate stage below. Both of them were attached to their own stage by vacuum system. Precise alignment was performed by using the x-y-θ stage to move the substrate to match the mask plate pattern. A top-side alignment (TSA) microscope was used to magnify and align the mask pattern into the exposed area. The exposure time was altered prior to the illumination process.

3.5.1.1 Photolithography Dose Test

Due to reflection and absorption of the underlying substrate, the optimal dose for SU-8 exposure on Si and glass will be different. The exposure time of the SU-8 layer on the glass was varied from 20 – 60 s. The exposure patterns were developed and then viewed under microscope. From the inspection images, patterns appeared for exposure time upwards of 35 sec for both glass and wafers. 35 s was chosen as the optimal time to avoid broadening of the designed pattern due to over exposure (see later). It was also found that better pattern definition could be obtained if a UV filter was used to remove the excessive light energy below 350 nm. Thus a UV filter (BG12-SCHOTT) was used to obtain a 2 μm gap as shown in **Figure 3.5**.

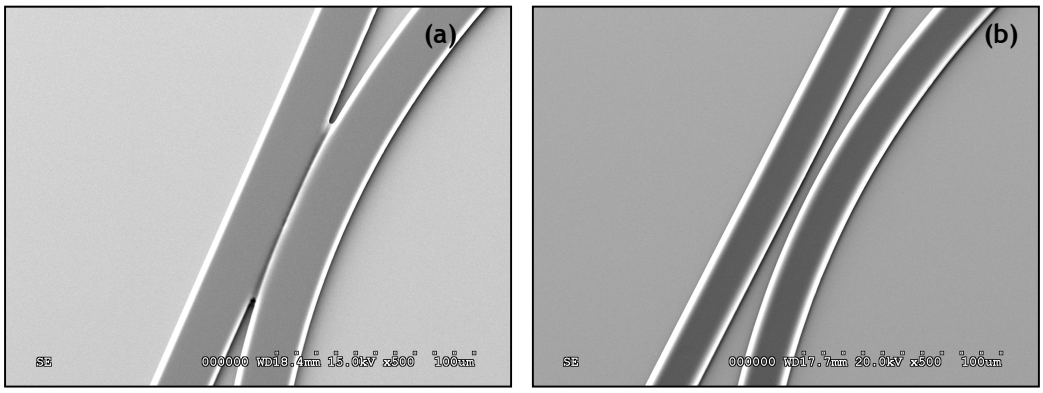

Figure 3.5: SEM images of the gap between ring resonator and waveguide at 35 sec exposure time using mask aligner (MA6). (a) Without the UV filter and (b) with the UV filter (BG12-SCHOTT).

It was found that the reason for the merging of the closely spaced attachment of the gap spacing seemed to be the high absorption of SU-8 at the shorter wavelength ~ below 350 nm, in which the upper layers were highly exposed (without the UV filter) compared to the lower layer of the resist. **Figure 3.5 (a)** shows that the top layer of straight waveguide and ring resonator were attached to each other. However, when the UV filter was used during exposure, it cut down the intense wavelengths below 350 nm that emitted from the UV lamp and gave much better gap definition and edge quality.

3.5.2 Electron beam lithography (EBL)

Photolithography is a process used to transfer the desirable patterns/structures into the substrate by using light to generate an acid catalyst that cross-links the resist and then discriminatively removing the unwanted part of resist layer. Instead of using light, an electron beam can also be used to generate the acid catalyst. This offers higher resolution patterning of smaller structures since electrons have much more shorter wavelengths around (~ 10^{-12} m) compared to the light (UV light, λ = ~ 300 nm) commonly used in the conventional photolithography instrument.

This is particularly important when patterning small, closely spaced features such as the gap in a ring-resonator structure. Here, patterning with a mask plate and conventional photolithography, the small gap on patterned masks could result in the diffraction of light and thus lead to developed patterns that showed diffraction effects, especially when the required structures were smaller than 2 μm.

Although a higher resolution can be obtained by using EBL, the time of patterning takes several hours, which is more time consuming compared to the mask aligner. In addition, factors such as electron scattering in the resist, as well as charging and proximity effects need to be considered before a pattern can be written. These can influence the exposure dose and result in unwanted exposed areas. As with photolithography, usually the final structures become larger than the defined pattern when overexposure has occurred.

3.5.2.1 EBL Dose Test

Three dose test ranges were submitted to the VB6 for electron beam writing. These were from (50-1000) μC/cm^2 for the first batch, (10-50) μC/cm^2 for the second batch and 1 - 10 μC/cm^2 for the third batch. The pattern and layout of a typical dose test sample is shown in **Figure 3.6**.

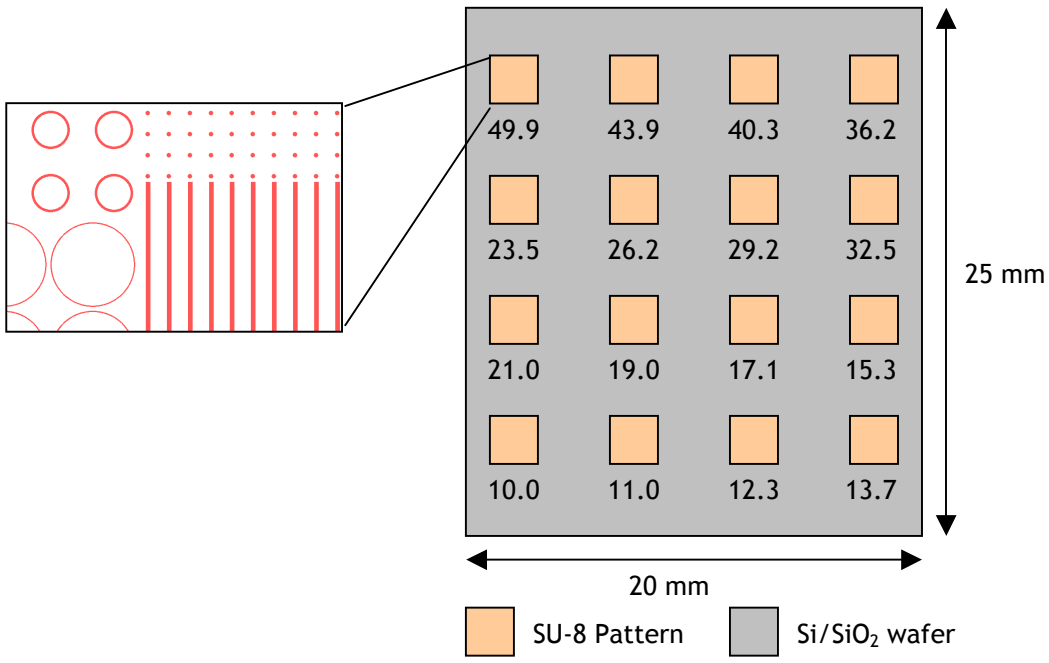

Figure 3.6: Dose test job submission to electron beam lithography VB6. Arrays of varied electron beam charge value 10-50 μC /cm^2 were applied to investigate the accurate exposure dose for SU-8 resist.

The developed patterns were viewed by both optical and SEM S-4700 (Hitachi, Japan) to determine the quality of the developed structures. These images were compared with drawing dimensions to verify for example, whether an expansion or thinning of the structure had occurred during the development procedure. According to the images obtained, over-exposed patterns expanded and merged into each other, if there was a gap between two closely positioned structures. Meanwhile, under-exposed patterns peeled off during the development

process due to the monomers not fully cross-linking during the exposure process, especially at the SU-8 substrate interface. The optimal dosage resulted in a smooth sidewall, precise shape and clean gap spacing after the development process.

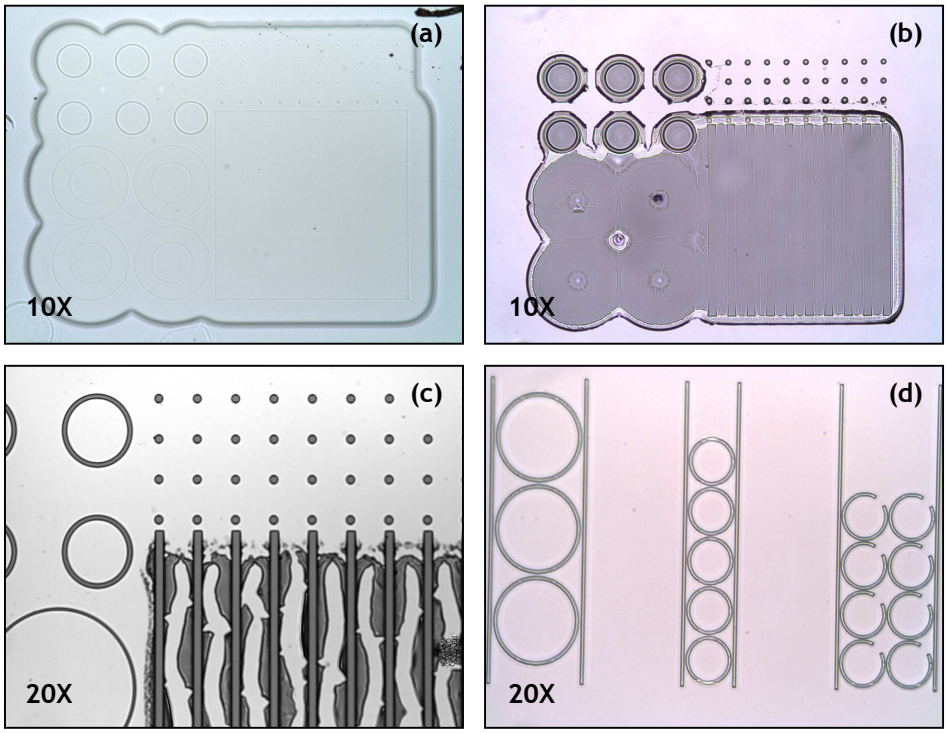

Figure 3.7: Images of the dose test pattern from the Leica microscope after the development process and hard bake: - (a) 1000 μC /cm^2, (b) 50 μC /cm^2, (c) 10 μC/cm^2 and (d) 2.5 μC/cm^2.

Results of a typical dose test are shown in the optical images of **Figure 3.7**. Figure 3.7(a) shows the effect when an electron beam dose of 1000 μC/cm^2 is used. It can be seen that the patterns (dots, lines and rings) were bulged or swollen. **Figure 3.7(b)** demonstrates the effect when the dose was reduced to 50 μC/cm^2. Here it can be seen that there is a pattern of widely spaced dots but larger features are still over exposed. Reducing the dose to 10 μC /cm^2 improved the ring structures, but long lines were still over exposed as shown in **Figure 3.7(c)**. However, when the exposure dose was further lowered to 2.5 μC/cm^2, it can be seen in **Figure 3.7(d)** that the defined patterns and gaps appeared completely. Below the 2.5 μC/cm^2, no visible pattern was formed (under exposed). Thus, the optimal dose for SU-8 polymer was around 2.5 μC/cm^2.

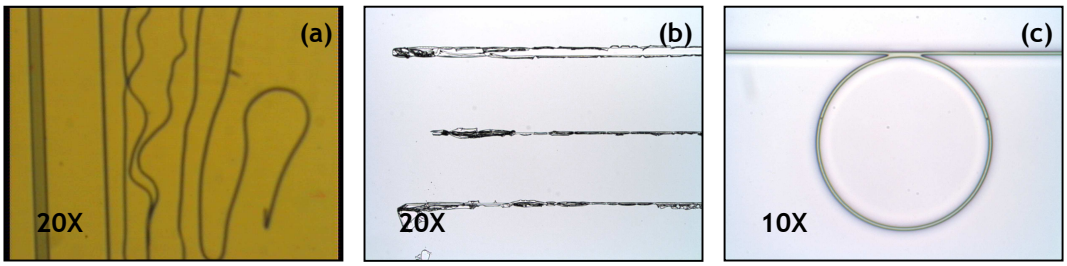

Figure 3.8: Microscope images showing the result after the development process: - (a) Dose used at 1.0 μC/cm^2, (b) Resist residue after dose development process and (c) clean gapless ring resonator structure development process.

As an illustration of what can occur when the resist is under or over exposed, **Figure 3.8** shows the microscope images of a SU-8 pattern on a Si/SiO_2 wafer after the recommended development processing. As shown in **Figure 3.8(a)**, the SU-8 structures peeled off during the development process when the exposure dose was set at 1.0 μC/cm^2. At this low dose, the underneath of the SU-8 resist layer was 'under-dose' exposure. As a result, not much cross-linking occurred in the region of the polymer underneath compared to the top layer the polymer coating. Straight waveguides that represented the top area of the pattern were clearly visible during post exposure bake (PEB) at 65^{o}C and 95^{o}C. However, when the substrate was soaked in the developer and agitated, the 'under-dose' exposed area was dissolved and the entire pattern peeled off.

If the dose was too high, so as to cause 'over-dose', electrons that scattered in the substrates underneath the structure will lead to a build up of polymer cross-linking to the edge of a straight waveguide. This material appeared at the edge of the defined structure and added to the sidewall roughness, as shown in **Figure 3.8(b)**. On the other hand, as shown in **Figure 3.8(c)** with the suitable dose between 2.0-3.0 μC/cm^2, a defined and clean structure was obtained even when the development period in the solvent was longer than the recommended time given in the datasheet. Finally, a hard bake process is recommended as the last stage of the development process, was used to further cross-link the resist and make it durable and robust for subsequent processing. Both hard baked and non-hard bake substrate were tested for 5 minutes cleaning with IPA in an ultrasonic bath to assess adhesion. It was observed that, without the hard bake procedure, SU-8 patterns swelled and peeled off easily. However, with the hard bake process, the SU-8 patterns were unaffected by sonication.

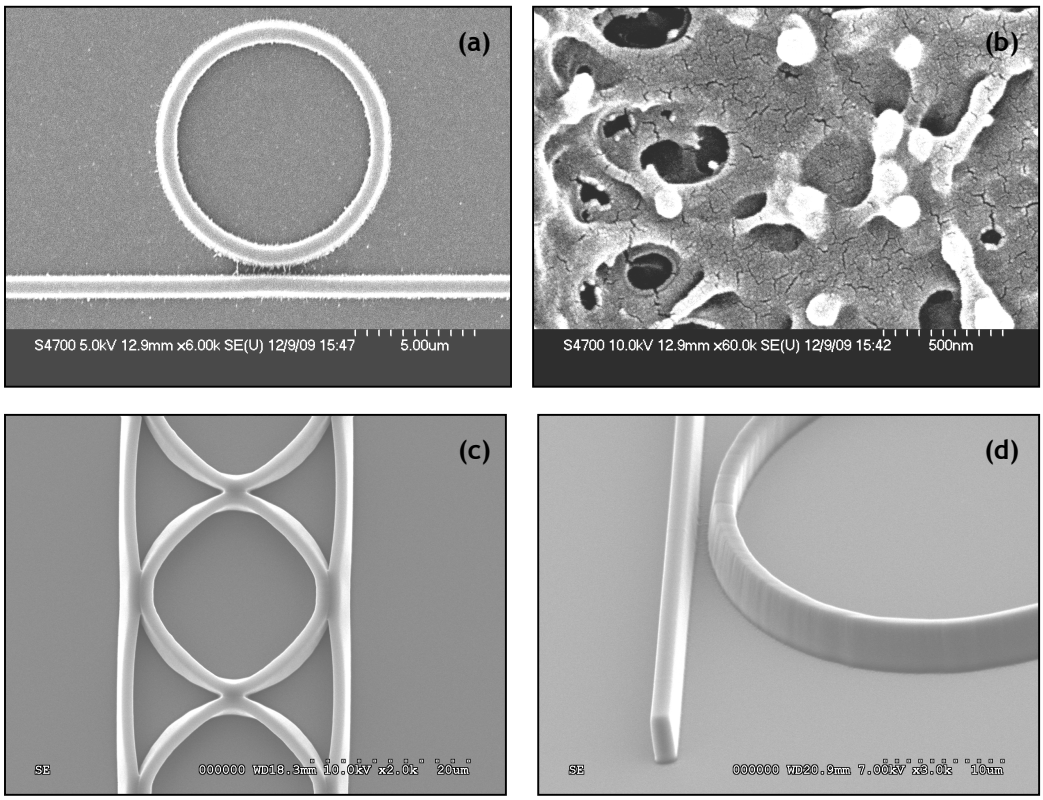

Figure 3.9: SEM images of microring resonator. a) Over dose pattern after development process, b) Unwanted debris, c) Ring resonator with 200 nm gap after hard baked process and d) 45^{o} degree of angle view.

Finally, for further detailed inspection of the ring resonator patterns, SEM equipment was used. As can be seen in **Figure 3.9 (a)**, when the dose is too high, there is unwanted debris between the straight waveguide and the ring resonator. **Figure 3.9 (b)** shows an enlarged image of the debris between the gap spacing at 60X magnification, clearly showing the unwanted crosslinking debris accumulated at the sidewalls of both ring and straight waveguide structures. After several attempts were made to fabricate structures with 200 nm gaps, it was constantly found that SU-8 polymer structures expanded and bulged too much, leading to the loss of the 200 nm gap defined in the original e-beam pattern. Typically, two important structures (a ring and straight waveguide) have become attached to each other the end of the development and hard baked processes, as can be seen in **Figure 3.9(c)**. Eventually, after multiple iterations, it was found that the minimum gap spacing that could be fabricated with optimal dose and development procedures, that also had low sidewall roughness was 300 nm, as shown in **Figure 3.9(d).**

3.6 General Protocol for Preparing, Exposing and Developing Pattern

3.6.1 Materials and Methods

SU-8 polymer resist (Microchem Corp, USA) is purchased and used to fabricate a polymer waveguide structure. Silicon wafer (with 3.5 μm oxide layer) is acquired from University Wafer, USA as substrate. Acetone and isopropyl alcohol (IPA) that used for substrate cleaning and rinsing process was purchased from Fisher Scientific, USA and Sigma-Aldrich, USA respectively. Microposit EC solvent developer (Shipley European Ltd, UK) was used. Cleaning and resist development process were performed under laminar flow hood conditions in the JWNC cleanroom.

3.6.2 Cleaning

A silicon wafer with 3.5 μm of silicon oxide (SiO_2) was cleaved into substrates of (20 x 20 mm). These substrates were cleaned from dust and wafer debris accumulated during scribing, by using a N_2 gas gun. They were then ultrasonically cleaned for 5 minutes in acetone and then for 5 min in isopropyl alcohol (IPA) before being washed in RO water for another 5 minutes. Subsequently, the substrates are dried under a N_2 flow and put into the oven at the temperature of 180^{o}C for 10 minutes to fully dry. Finally, the substrates were placed in an oxygen plasma asher (Gala Instrumente, Germany) for 5 minutes at 120 W to remove any remaining organic or inorganic residues.

3.6.3 Resist Spinning

SU-8 resist was used throughout the project. It was important to make sure the substrates were fully dried before SU-8 resist was applied. The substrate was positioned on the top of spinner chuck. Next, the SU-8 resist was dispensed from the small bottle onto the centre of the substrate and allowed to spread to the edge of the substrate. Then the resist was spun at 3000 rpm for 30 s to obtain a 1μm thickness structure (final thickness after development process). Particular thickness was obtained by changing the spinner speed or viscosity. After spinning, the substrate was placed onto a 95^{o}C hotplate for a soft bake process at 5 min. This step was essential to evaporate the remaining solvent in the SU-8 resist layer before proceeding with the exposure process. The soft bake also helped to avoid the resist sticking to the mask plate when the hard contact option was used on the mask aligner.

3.6.4 Patterning

The particular details of photolithography and EBL patterning have been discussed in **Section 3.5**.

3.6.5 Development Process

After exposure with photolithography or electron beam, the substrates were placed onto a hotplate for a post-exposure bake. The substrates were left on the hotplate for 1 minute at 65^{o}C followed by 1 minute at 95^{o}C. This sequence was carried out to avoid resist stress and cracking. Usually, the SU-8 patterns were visible in the resist after post-exposure bake if the electron beam or photolithography dose had been sufficient to cause cross-linking. After post-exposure bake, the substrates were developed using EC solvent for 2 minutes, followed by a 1 minute with IPA and drying by N_2 gun. The final step involved hard bake at 180^{o}C on a hotplate for 5 minutes.

3.7 Images of Optimal Device Structures

For a 200 nm gap ring resonator design, after extensive patterning trials and optimisation of the fabrication procedure, only a small number of substrates showed the good result of having a clear gap spacing corresponding to the initial L-edit layout design. In others, the straight waveguide and ring resonator structure had merged. According to the fabrication results, it was found to be impractical to fabricate resonators with high aspect ratio structures with 200 nm gap using the fabrication protocol and facilities available. In **Chapter 2**, the influence of gap spacing and the efficiency of coupling between the straight waveguide and the ring structure are discussed. In this work, simulations suggested that an optimal gap separation of 60 nm would be appropriate for visible wavelength devices. Clearly, the fabrication results shown in this chapter indicate that the methods are impractical, using the techniques available. To confirm this, two working substrates (200 nm gap) were tested with visible light, but no resonance signal could be detected. To overcome this fabrication constraint and difficulty, a gapless ring and disk structure was developed and small-scale simulations were made to compare the resonance results of gap and gapless structures. These simulation results have been discussed in Chapter 2, while the experimental characteristic of the gapless structure are discussed in **Chapter 4**. The working fabricated device is shown in **Figure 3.10**.

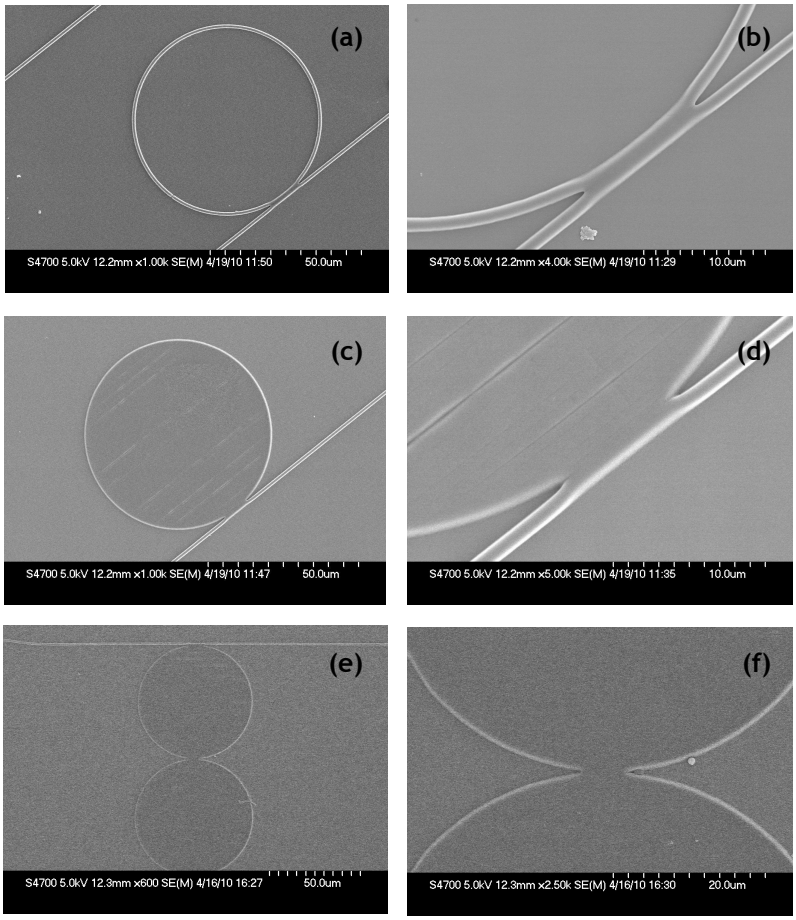

Figure 3.10: SEM images of gapless resonator structures. (a) and (b) Ring resonator; (c) and (d) Disk resonator at 40 μm of radius; (e) Double-cascaded disk resonator (DDR) with different diameter and (f) Enlarged area of DDR at the disk intersection.

3.8 PDMS Microfluidic Channel

In practical sensing applications, delivering a certain volume of fluid onto the sensing surface is an important consideration. Among the liquid manipulation techniques, micron scale channels are one of the most common methods to handle a small volume (micro, nano, pico-litres) of fluid for detection[13][14][15]. This requires the fabrication of a micro channel coupled to mechanical pumps and tubing to move analyte solutions. The flow rate of liquid can be controlled and mixing of two different media can be performed for continuous detection. In this research, polydimethylsiloxane (PDMS) (Slygard ® 184, Dow Corning) was used as the material to fabricate channel structures.

In order to fabricate the microfluidic channel using the PDMS polymer, a suitable pattern mould was designed and fabricated. The replica moulds for the PDMS channel were made using photolithographically defined SU-8 structures on silicon substrates as shown in **Figure 3.11**.

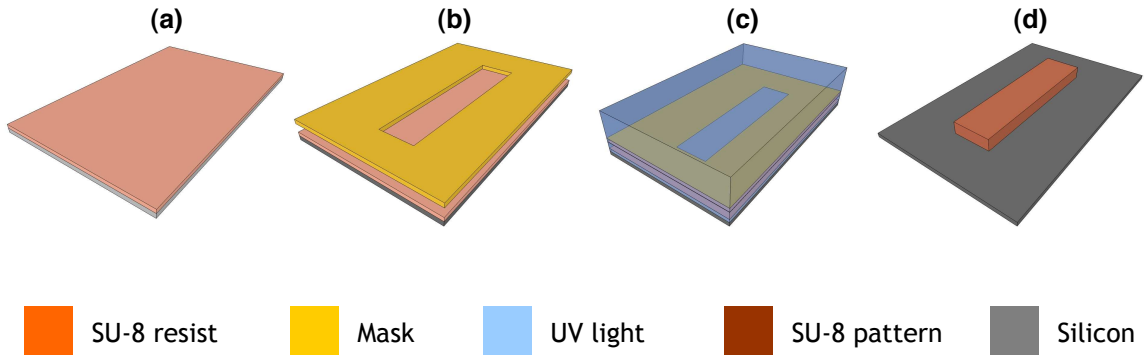

Figure 3.11: Fabrication diagram of SU-8 polymer mould for the PDMS microfluidic channel. (a) Sample was spun with SU-8 25; (b) Mask pattern was aligned; (c) UV light exposed by using MA6 instrument and (d) SU-8 pattern appeared after development process.

Figure 3.11 details the SU-8 fabrication steps to make the master mould for PDMS microfluidic channel. This straightforward processes involved resist spinning, exposure, development process and hard bake. The dimension pattern of the SU-8 mould structure was 1 mm x 20 mm x 500 µm of thickness. The mould was placed inside the glass petri dish 100 mm x 15 mm (Corning Ltd, USA) to provide a receptacle for the PDMS monomer solution. The overall processes flow to make PDMS channel device is shown in **Figure 3.12**.

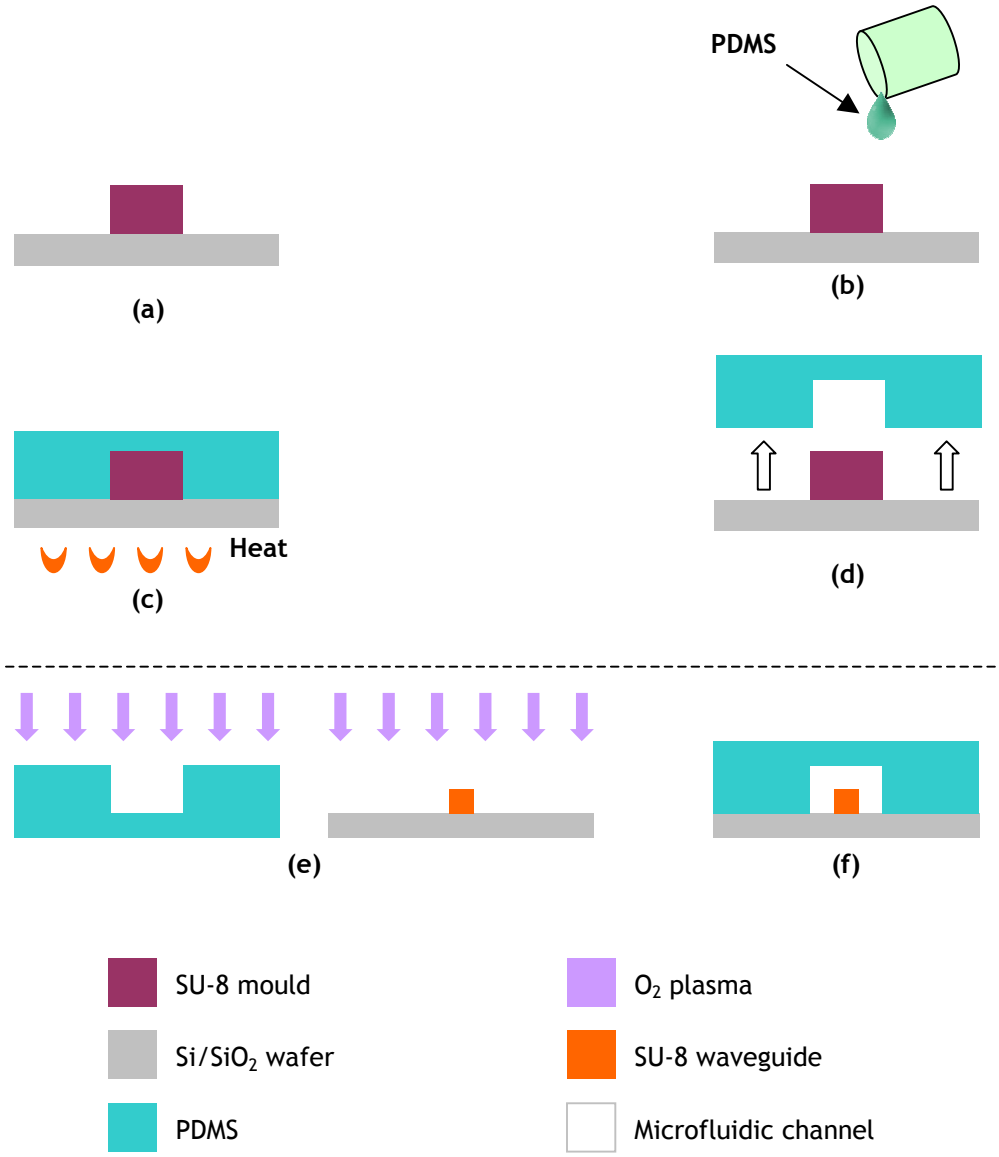

Figure 3.12: Schematic steps of microfluidic channel fabrication. (a) SU-8 mould structure, (b) Prepared PDMS was poured onto mould, (c) The curing process, (d) Peeling off the structure using a scalpel, (e) PDMS surface and SU-8 pattern were sonically cleaned, then exposed to O_2 plasma, (f) PDMS and substrate surface bonding.

Figure 3.12 (a) shows the developed SU-8 structure that will be used as a mould to fabricate a microfluidic channel. The PDMS was prepared by mixing the monomer with a curing agent in the ratio of 10:1. These compound were mixed for 5 minutes and then degassed inside vacuum desiccator to remove air bubbles from the mixture. The degassed PDMS mixture was poured onto the SU-8 mould**, Figure 3.12 (b)**. This was then placed in the oven for 5 hours at 60^{o}C to be cured as shown in **Figure 3.12 (c)**. The PDMS structure was peeled off from the mould**, Figure 3.12 (d)**. Prior to bonding the substrates, the PDMS microfluidic channel and SU-8

waveguide substrate were cleaned with methanol and isopropanol (IPA) in an ultrasonic bath before dried with a nitrogen gun. Both of the PDMS microfluidic channel and the SU-8 waveguide substrate were then placed into the oxygen plasma asher, facing upward, **Figure 3.12 (e)**. The asher control was set to 100W for 30 sec. After plasma treatment, the PDMS microfluidic channel was aligned to the SU-8 substrate and pressed firmly together for 10 sec with tweezers, as illustrated in **Figure 3.12 (f)**. Finally, polytetrafluoroethylene (PTFE) tubing and a syringe needle (BD Microlance, 22G, 0.7 x 13 mm) were used to connect the channel to a syringe so as to introduce liquids and samples.

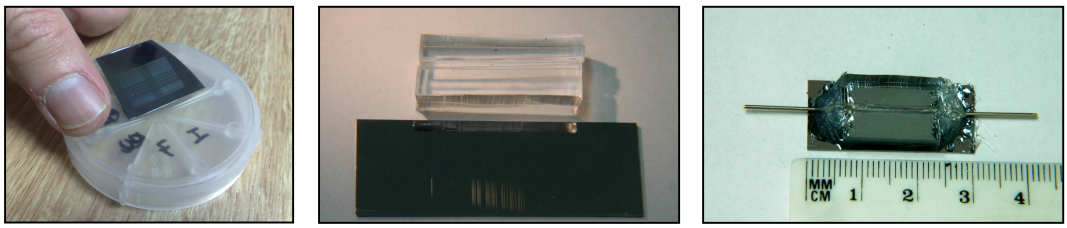

(a) **(b)** **(c)**

Figure 3.13: Images of the substrate after the development process. (a) Substrates with SU-8 patterns before cleaving step; (b) Prepared PDMS and SU-8 pattern for surface binding; (c) SU-8 substrate with working PDMS channel for measurement. Sensing surface was inside the microfluidic channel; inlet and outlet were also shown.

Figure 3.13 shows the images of the fluid device after all of the cleanroom fabrication processes. Note, the optical characteristics of substrates were tested by using an experimental setup (see **Figure 4.4, Chapter 4**) to verify the resonance patterns before being bonded to the PDMS channel. They were then re-tested after bonding to the PDMS microfluidic channel. This second set of tests on the final device showed that the resonance patterns were unaffected by the PDMS superstructure.

3.9 Summary

The main aim for this chapter was to describe the steps needed to fabricate ring resonator devices and the efforts undertaken improved the reproducibility and repeatability of the SU-8 fabrication procedure. A combination of using EBL to define the micro resonator structure and PDMS moulding to create the microfluidic channels produced a final device that can be used for further characterization and experimental work. Although fabrication difficulties and reproducibility of making small gap spacing structure with SU-8 polymer have been reduced, nevertheless gapless resonator structures were selected as the prudent chosen route to make the resonator devices used in the assay investigations described in subsequent Chapters. Straightforward SU-8 polymer fabrication steps (without dry etching and multi-stage processing

required by Si), has resulted in a rapid process for making a resonator device that can be surface modified for sensing purposes, with the whole process flow taking 1-2 days per device.

References

[1] S. Thoms and D. S. MacIntyre, "Electron Beam Lithography Course." [Online]. Available: http://www.elec.gla.ac.uk/jwnc/internal.php?module=ebeam&cmd=vb6docs

[2] B. Li, M. Liu, and Q. F. Chen, "Low-stress ultra-thick SU-8UV photolithography process for MEMS," Journal of Microlithography Microfabrication and Microsystems, vol. 4, pp. -, 2005.

[3] H. Lorenz, M. Despont, N. Fahrni, N. LaBianca, P. Renaud, and P. Vettiger, "SU-8: a low-cost negative resist for MEMS," Journal of Micromechanics and Microengineering, vol. 7, pp. 121-124, 1997.

[4] S. Toumikoski, "Fabrication of SU-8 microstructures for Analytical Microfluidic Applications," Doctoral Dissertation, Helsinki University of Technology (DTU), 2003.

[5] A. S. Holland, V. S. Balkunje, A. Mitchell, M. W. Austin, M. K. Raghunathan, and G. Kostovski, "Effects of design geometry on SU-8 polymer waveguides," Smart Structures, Devices, and Systems Ii, Pt 1 and 2, vol. 5649, pp. 186-194, 864, 2005.

[6] S. Silvan, "Immobilization of DNA and protein to polymerized SU-8 photoresist investigated with micro array assays," Diploma Thesis, Technical University of Denmark (DTU), 2003.

[7] E. A. Shields, F. Williamson, and J. R. Leger, "Electron-beam lithography for thick refractive optical elements in SU-8," Journal of Vacuum Science & Technology B, vol. 21, pp. 1453-1458, 2003.

[8] M. Nordstrom, D. A. Zauner, A. Boisen, and J. Hubner, "Single-mode waveguides with SU-8 polymer core and cladding for MOEMS applications," Journal of Lightwave Technology, vol. 25, pp. 1284-1289, 2007.

[9] B. H. Ong, X. C. Yuan, and S. C. Tjin, "Adjustable refractive index modulation for a waveguide with SU-8 photoresist by dual-UV exposure lithography," Applied Optics, vol. 45, pp. 8036-8039, 2006.

[10] L. N. Jiang, K. P. Gerhardt, B. Myer, Y. Zohar, and S. Pau, "Evanescent-Wave Spectroscopy Using an SU-8 Waveguide for Rapid Quantitative Detection of Biomolecules," Journal of Microelectromechanical Systems, vol. 17, pp. 1495-1500, 2008.

[11] D. X. Dai, B. Yang, L. Yang, Z. Sheng, and S. L. He, "Compact Microracetrack Resonator Devices Based on Small SU-8 Polymer Strip Waveguides," IEEE Photonics Technology Letters, vol. 21, pp. 254-256, 2009.

[12] M. Balakrishnan, M. Faccini, M. B. J. Diemeer, E. J. Klein, G. Sengo, A. Driessen, W. Verboom, and D. N. Reinhoudt, "Microring resonator based modulator made by direct photodefinition of an electro-optic polymer," Applied Physics Letters, vol. 92, pp. -, 2008.

[13] J. C. McDonald and G. M. Whitesides, "Poly(dimethylsiloxane) as a material for fabricating microfluidic devices," Accounts of Chemical Research, vol. 35, pp. 491-499, 2002.

[14] J. N. Lee, C. Park, and G. M. Whitesides, "Solvent compatibility of poly(dimethylsiloxane)-based microfluidic devices," Analytical Chemistry, vol. 75, pp. 6544-6554, 2003.

[15] S. Talaei, O. Frey, P. D. van der Wal, N. F. de Rooij, and M. Koudelka-Hep, "Hybrid microfluidic cartridge formed by irreversible bonding of SU-8 and PDMS for multi-layer flow applications," Proceedings of the Eurosensors Xxiii Conference, vol. 1, pp. 381-384, 1546, 2009.

[16] MicroChem Corp, USA [Online]. Available: http://www.microchem.com/

[17] Vistec Lithography Inc, USA. [Online]. Available: http://www.vistec-litho.com

[18] SUSS MicroTec AG, Germany. [Online]. Available: http://www.suss.com/

[19] Headway Research Inc, USA. [Online]. Available: http://www.headwayresearch.com/

[20] Hitachi High Tech America, USA [Online]. Available: http://www.hitachi-hta.com/

[21] Leica Microsystem, Germany [Online]. Available: http://www.leica-microsystems.com/

CHAPTER 4

Optical Characterization

Introduction

In the previous chapter, SU8 polymer resonator device fabrication processes were described. However, before use in sensing applications, the devices must be optically characterized in order to determine their spectroscopic response. This characterization Chapter has been divided into three subdivisions. Firstly, the measurements required to determine the material properties of SU-8, including refractive index and optical absorbance, are described. Secondly, a brief overview of the layout for measuring the optical throughput of the waveguide and resonators used throughout this work is given. Then, thirdly the optical resonance response for different resonator structures and configurations is given and analysed.

4.1 Characterizing the Material Properties of SU-8

4.1.1 Introduction

In this section, the SU-8 polymer optical properties are characterised using a standard Abbe refractometer and UV-Vis absorption spectrophotometer. Whilst the manufacturers datasheets provided guideline values for these properties, experimental validation was needed since the processing recipes used have been altered during the course of process optimisation (see **Chapter 3**) for this work.

4.1.2 Materials and Methods

Generally, SU-8 polymer waveguide and micro-resonator were fabricated in the cleanroom. The Abbe Refractometer 60 (Bellingham and Stanley, UK) is used to determine the refractive index of the SU-8 polymer after the development process. Meanwhile, a spectrophotometer was used to identify the absorbance properties of SU-8 (as well as the PDMS polymer). These two properties play an important role in determining the interactions of the materials with light propagating in a waveguide, in the visible wavelength region. The absorptivity parameter was measured by a Hitachi U-2000 optical spectrophotometer (Hitachi Corp, Japan). Finally, the detection sensitivity layer is conducted using polymethyl methacrylate (PMMA)(MicroChem Corp, USA) to estimate the thickness of sensitive layer when biological binding interaction occurs in actual experiments. The PMMA layer thickness is measured using a Veeco Dektak 6M surface profiler (Veeco, USA) in the JWNC.

4.1.2 SU-8 Properties

4.1.2.1 Refractive Index

According to the literature, the refractive index (n_{SU-8}) of SU-8 polymer is approximately 1.55. In order to utilize SU-8 polymer as a waveguide, the refractive index of the surrounding medium (e.g. cladding or analyte solutions) must be lower than the refractive index of SU-8 polymer. Thus in a typical device design, silicon oxide (SiO_2) (with n = 1.46) was used as a buffer layer between the Si substrates and the lower/bottom interface of the waveguide (see **Figure 2.1**) and the upper medium was either air 1.00, or DI water at 1.33, (all of these have a lower index than SU-8 polymer material).

With this arrangement, the light can propagate and be confined and guided in the higher refractive index SU-8 structure via the TIR. In order to determine the refractive index of the SU-8 polymer, seven samples were prepared using different processing conditions and measured by

using an Abbe refractometer (see **Appendix A.4.1**). Samples were prepared by spinning resist then exposed for 35 s, then subjected to 65°/95°C post-exposure bake and standard EC solvent development. However, after this, the hard bake was conducted at 180°C for a varying time scale for each sample (see **Table 4.1**). To avoid SU-8 resist cracking, the samples were placed on a hotplate at 65°C and the temperature was gradually increased to 95°C over the course of 1 min. The sample was then, transferred to a hotplate at a constant temperature of 180°C, for the hard bake step. Then samples were allowed to cool down to room temperature before the refractive indices were examined and further analysis was performed.

Table 4.1: Hard bake time and refractive index value for fabricated samples.

No	180°C Hard bake / min	Abbe (°) ± (0.1)	Ref n^{20} (Avg) ± (0.00098)	Ref n^{25} (Avg) ± (0.00098)
1	0	30.4	1.57851	1.57848
2	1	32.7	1.59657	1.59654
3	3	34.3	1.60814	1.60811
4	5	35.7	1.61759	1.61756
5	10	36.4	1.62204	1.62201
6	15	36.2	1.62102	1.62099
7	20	36.4	1.62238	1.62235

From the **Table 4.1**, the average refractive index values were plotted against the hard bake time (min) and shown in **Figure 4.1**.

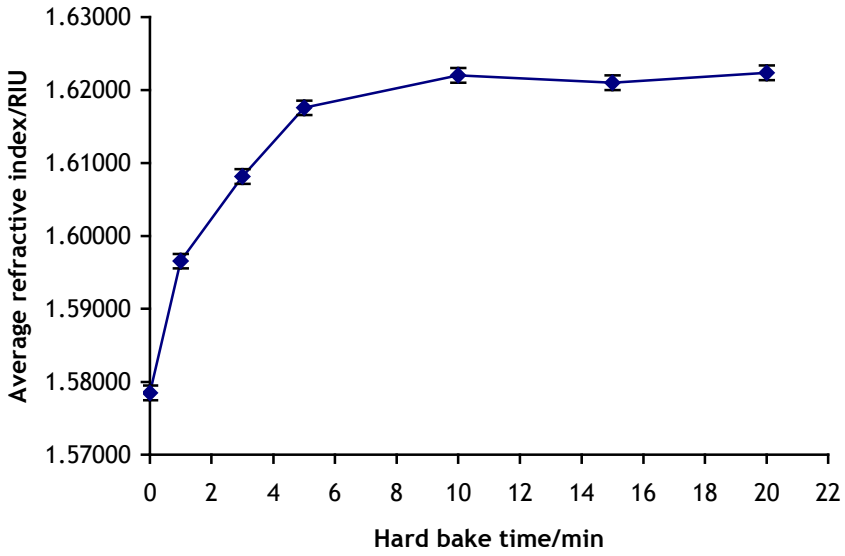

Figure 4.1: Average refractive index/RIU difference against the hard bake time/min. Hard bake duration for each sample was set at different periods for comparison. Experiments were conducted twice and the error bar of the average result was obtained from Abbe refractometer equipment at (± 0.00098). The temperature was corrected to room temperature at 25°C since the initial reference was calibrated for 20°C.

Figure 4.1 shows the average refractive index as measured by an Abbe refractometer, of SU-8 polymer samples hard baked for different periods. It can be seen that, without hard baking, the refractive index of SU-8 sample was 1.57851 ± 0.00098. When the hard bake time increased, the refractive index also increased. The increase in index levelled off when the samples were left on the 180°C hotplate beyond 5 min. This showed that the SU-8 polymer has the potential to have its refractive index tuned by regulating the hard bake period. Note, other methods that have been used to regulate the refractive index include using dual-UV exposure lithography[1][2]. In this work, reducing the pre-exposure bake period to 1 min, the refractive index was found to increase sharply after 2 min of hard baking and become constant after 20 min of hard bake. All of these observations are consistent with the increment of the refractive index being due to the solidification and densification of the SU-8 as a consequence of thermal effects, inline with the Lorentz-Lorenz equation,

$$\frac{n(t)^2 - 1}{n(t)^2 + 2} = \frac{4\pi N_A \alpha(t) \rho(t)}{3M} \qquad (4.1)$$

Where n is the refractive index, t is the baking time period, M is the molecular weight of the polymer unit, N_A is the Avogadro number, α is the polarizability of the polymer molecules, ρ is the density of the polymer[3].

Assuming that all the variables are constant except the refractive index, n and polymer density, ρ. The change of ρ during hard bake will affect the refractive index of the SU-8 polymer samples with increasing values being obtained by following longer baking times. Further investigation of the hard bake time parameter was performed by leaving two samples on the hot plate for an hour to see if any degradation of the polymer occurred. Both samples survived 1 hour at 180°C temperature. However, when the temperature was increased to 300°C, the polymer became discoloured due to oxidation or decomposition effects after 20 min.

In conclusion, it has been shown that the refractive index of SU-8 polymer increases and reaches a stable value after 5 min hard bake time.

4.1.2.2 Absorptivity

According to the literature (MicroChem Corp, USA), SU-8 polymer is transparent above λ = 400 nm and has extensive absorption below λ = 350 nm. Since the output from the white light source is from 300 nm upward, it was desirable to investigate the lowest wavelength light that could propagate through the material when it is used as a waveguide.

An Hitachi U-2000 series spectrophotometer was utilised for the UV-Vis absorption experiment. The wavelength sweep for this spectrophotometer series ranged from λ = 300 nm - 1100 nm and the photometric range was 0-2 Abs units. The spectrophotometer diagram and description can be found in **Appendix A.4.2**.

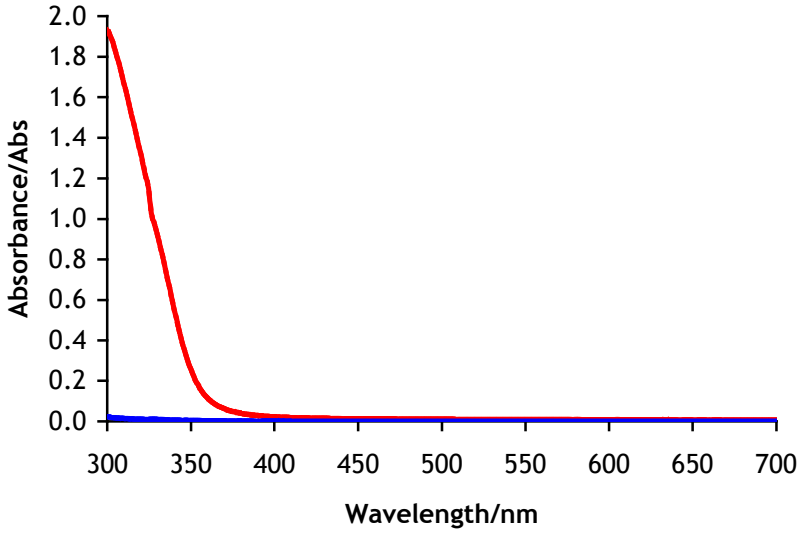

Figure 4.2: Absorbance value of 10 um layers of SU-8 polymer (red line), with 2 min of hard bake and 1 h cured PDMS (blue line) at 60°C.

As illustrated in **Figure 4.2**, the absorbance value for SU-8 polymer is low from 450 nm upwards. This shows the excellent transparency of SU-8 material within the visible wavelength region after the polymer had been cured with a 2 min hard bake process. Meanwhile, the absorbance value increased exponentially below λ = 400 nm. This result, confirmed the characteristic graph given in the manufacturer's datasheet and can be used to calculate the relationship between the minimum wavelength that will propagate in an SU-8 waveguide, and the length of the waveguide. Meanwhile, since it is also important that the PDMS that defines the microfluidic channel and also acts as a cladding over part of the SU-8 structures does not absorb light, measurements were also made of its optical transmission. These showed that the material is almost transparent from λ = 300 nm upwards. Thus, as anticipated, PDMS was suitable to be utilized as the material for the microfluidic channel.

4.1.2.3 Detection Sensitivity

Chapter 2 showed that the penetration depth of the visible wavelength of the sensor was around λ = 60 - 80 nm from the sensor surface. This means that the detection sensitivity will be limited by the thickness of the multilayer binding reaction [4]. The sensors will not responsed

to any molecules or reaction layer beyond that particular thickness. In order to experimentally measure the thickness of the detection layer, PMMA was spun onto the sensor surface and the resonance wavelength shift was measured according to the PMMA thickness layer. The resonance wavelength was recorded for each PMMA spun layer. PMMA layer was chosen because of its refractive index of 1.46, which nearly matches the assumed refractive index of the bioanalyte monolayer. PMMA polymer is also transparent to visible wavelength and convenient to fabricate as an additional layer.

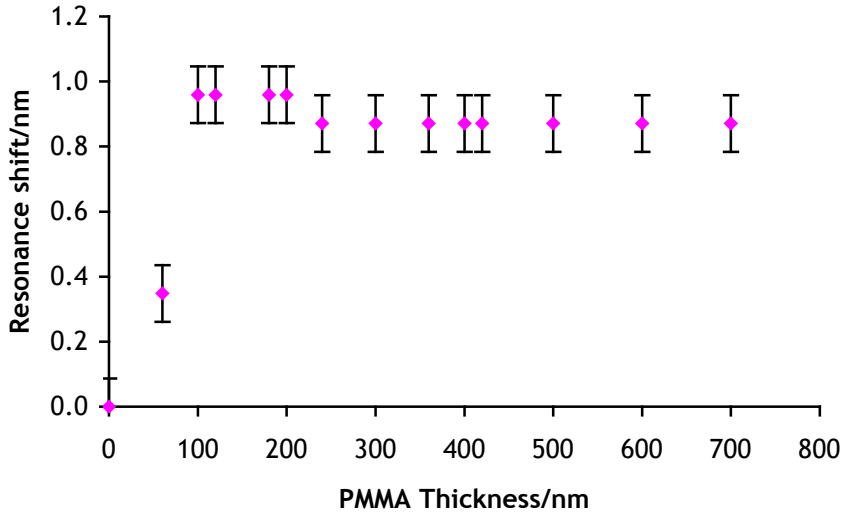

Figure 4.3: The resonance wavelength shift (nm) upon the spun PMMA polymer thickness (nm). The resonance wavelength (reference) was set without any PMMA layer, then the resonance shift is measured at each spun step. The error bar was obtained from the minimum reading of optical spectrum analyser SPEX 500M and is ±0.0087 nm.

Figure 4.3 shows the resonance wavelength (nm) due to the PMMA polymer layer on the top of the sensor surface. The thickness layer was measured by using a Dektak profilometer in the JWNC. PMMA polymer 2.5% with 2041 series was utilised in this experiment. The resonance wavelength was selected at 751.465 nm without any PMMA layer. Then, the device was spun with a PMMA layer and the thickness was measured using the profilometer. The device was placed on the experimental setup and the resonance pattern was recorded. The resist spinning, thickness measurement and resonance response acquisition were repeated until the measured resonance shift was constant.

Two samples were used and the average value shown in **Figure 4.3**. It was expected that the resonance wavelength shift would increase exponentially before it reaches a constant value. However, a 60 nm thick PMMA layer was the minimum thickness of the PMMA polymer that can

be produced in the JWNC. The resonance shift was 0.348 nm at 60 nm of PMMA layer. When the PMMA layer was increasing from 100 nm to 200 nm, the resonance shift was constant at 0.959 nm. However, when the PMMA layer was over 230 nm, the resonance wavelength shift exhibited a slight drop to 0.871 nm but it reached a constant value until the 600 nm of PMMA thickness.

This graph demonstrates that the sensing limit for this device was at most 100 - 120 nm away from the sensor surface. The resonance wavelength response changed drastically within 0 – 120 nm from the surface. Due to the constant value of the resonance wavelength shift beyond 120 nm, any changes of refractive index or analytes that interact beyond that limit will have minimal or no response at all. It is likely that the total thickness of any multi component binding assay would be smaller than 60 nm. For example, the thickness of streptavidin[5] is approximately 8.5 nm thick, while antibody[6] are ~ 4 nm, and biotin[7] was ~ 3 nm. It was assumed that any optical response was due to the analyte molecules that formed the monolayer on top of the SU-8 polymer surface.

4.2 Optical Characterization Setup

4.2.1 Materials and Methods

SU-8 (MicroChem Corp, USA) polymer resist is prepared and fabricated in the JWNC cleanroom. The fabricated devices are cleaved and the working device is then used for characterization. Devices were characterized using an optical experimental setup that consists of an optical spectrum analyser monochromator SPEX-500M (Horiba Ltd, Japan), a CCD camera DU420-BR-DD (Andor, UK), an optical fiber P1000-2-UV-VIS (Ocean optics, USA), a HeNe laser 5 mW (CVIMelles Griot, USA), a white light source Optic Lamp, 12V 100W (Osram GmbH, Germany), objective lens and various collimating lenses as shown in **Figure 4.4**.

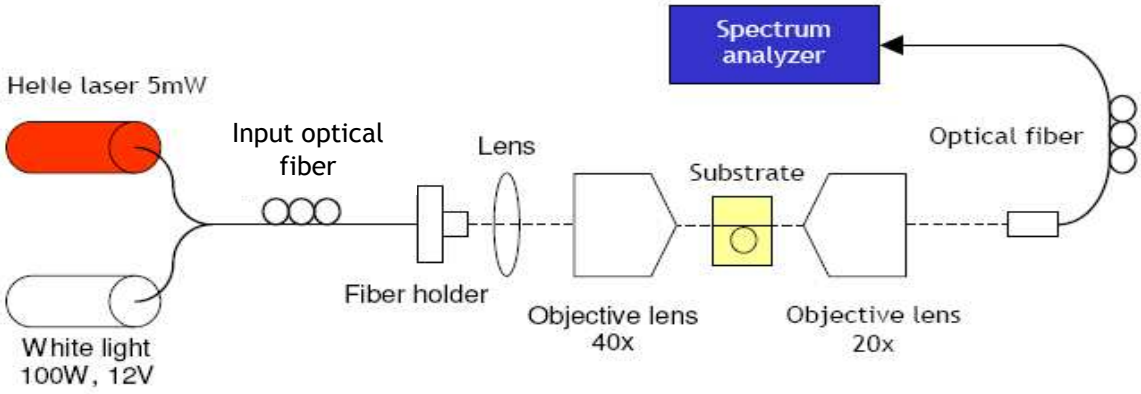

Figure 4.4: Schematic diagram of the measurement setup used for device characterization and experiments. The HeNe laser is used for input and output coupling alignment; the substrate is manipulated using a 3-axis stage to achieve the highest reading. When the maximum intensity is obtained from the spectrum analyser, the input optical fiber is switched to the white light source.

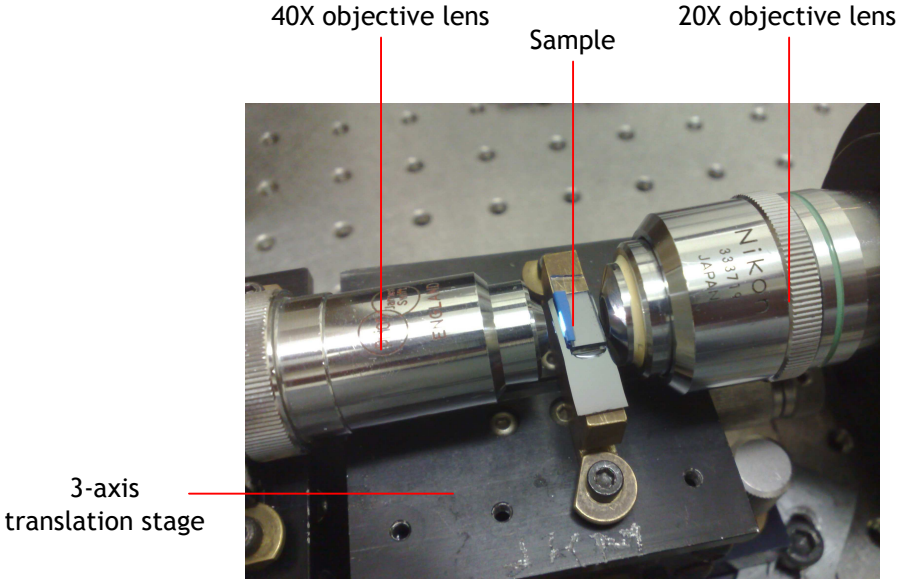

Figure 4.5: An expanded image of the light coupling section in the experimental setup with cleaved substrate. Both objective lenses are manoeuvred to be closer to the end-facet of the substrate in order to obtain good quality of focused light.

Since the light that is travelling slower in the substance than in a vacuum, the density of the liquid normally decreased with the increasing of temperature. As a result, the refractive index is also decreases. Therefore, it was necessary to apply a temperature correction to the literature given value. The corrected refractive index is approximated by (see **Appendix A.4.1**):

$$\left(RIndexT_1\right) - \left(T_1 - T_2\right)\left(0.0000078\right) = RIndexT_2$$

Generally, the devices were characterised by placing the cleaved substrate on a 3-axis translation stage (CVIMelles Griot Corp, USA) for end-butt coupling as shown in **Figure 4.5**. These translation stages were mounted directly on the optical table and precisely manipulated by using vernier micrometers. The HeNe laser was used as an illumination source for alignment by focusing through the objective lens (40x) onto the end facet of the waveguide input. The output light from the opposite side of the device was collected by a second objective lens (20x). The output light was then coupled into the SPEX-500M spectrophotometer by suitable alignment of the intermediate collection optical fiber. The focal length of the SPEX-500M spectrophotometer instrument was 0.5 meters and had a resolution was 0.02 nm when used with a 600 lines/mm grating. Collection of the output signal was maximised by monitoring the spectrum displayed in the optical spectrum analyser software. Each alignment stage was carefully adjusted in an iterative fashion. After alignment with the HeNe laser, the optical input fiber was switched to the white light source. The white light source covered the wavelength from range λ = 300 – 1100 nm and so required the SPEX-500M spectrophotometer to be operated in multi-window scanning mode.

4.2.2 The SPEX-500M Spectrum Analyser Software

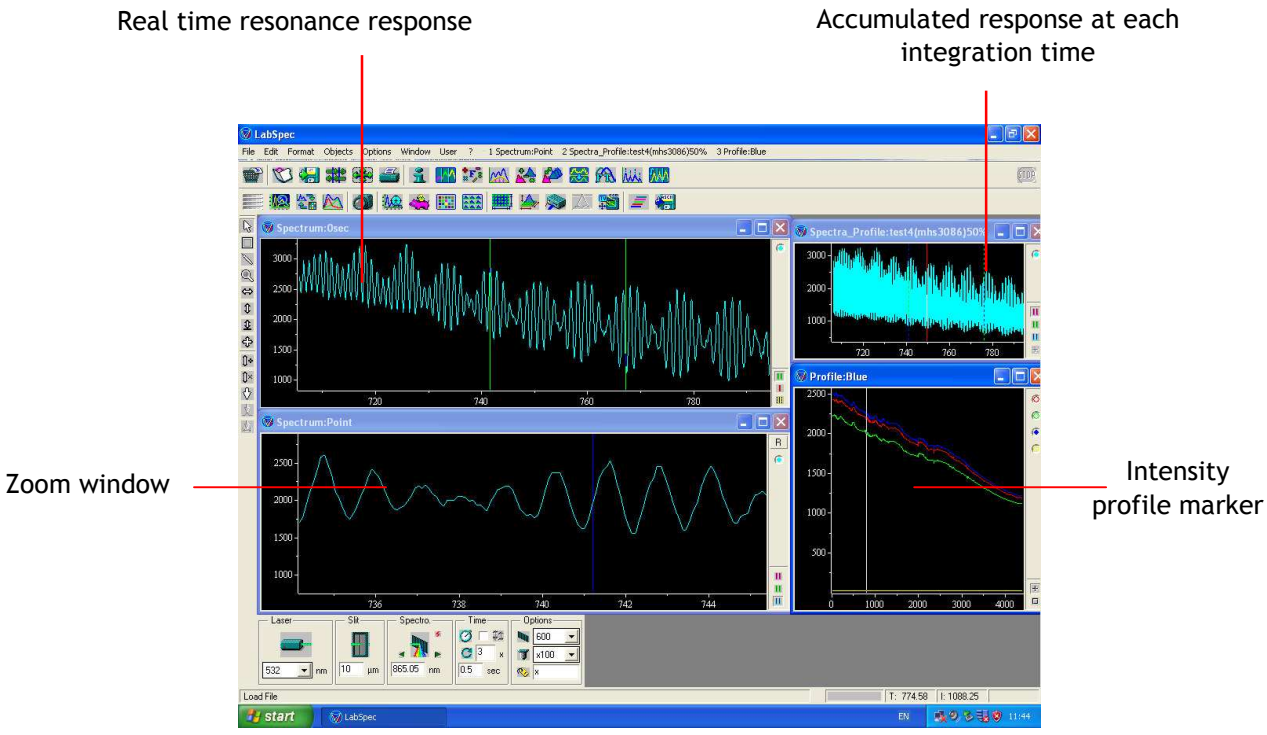

Figure 4.6: LabSpec software screen shot. Shows the resonance wavelength peak analysis and parameters tab control for the experiment. This software enables the user to run real time acquisition and off-line analysis.

Figure 4.6 shows a screen shot of the LabSpec software (**Horiba Ltd, Japan**) that was used for recording, measuring and analysing the spectroscopic output from different waveguides. By using this software, a multi-window scanning option could be used in order to measure a wide spectral range. Typically, an acquisition period took several minutes, depending on the integration time and averaging settings. Like other spectrum analysis software, LabSpec is equipped with normalization calculation, baseline correction, zoom, marker and layering for functions that can be used for off-line analysis.

According to the manufacturer's specification, the resolution of the SPEX-500M spectrum analyser is 0.02 nm. However, with the limitation of charge-coupled device (CCD) camera DU4020-BR-DD (Andor Technology, N. Ireland) during this experiment, the resolution obtained by the system was estimated as only 0.087 nm.

Figure 4.7 shows a typical spectral response for a (a) straight (reference) waveguide and (b) a resonator device, together with 'zoom' window for the 670-700 nm range (c).

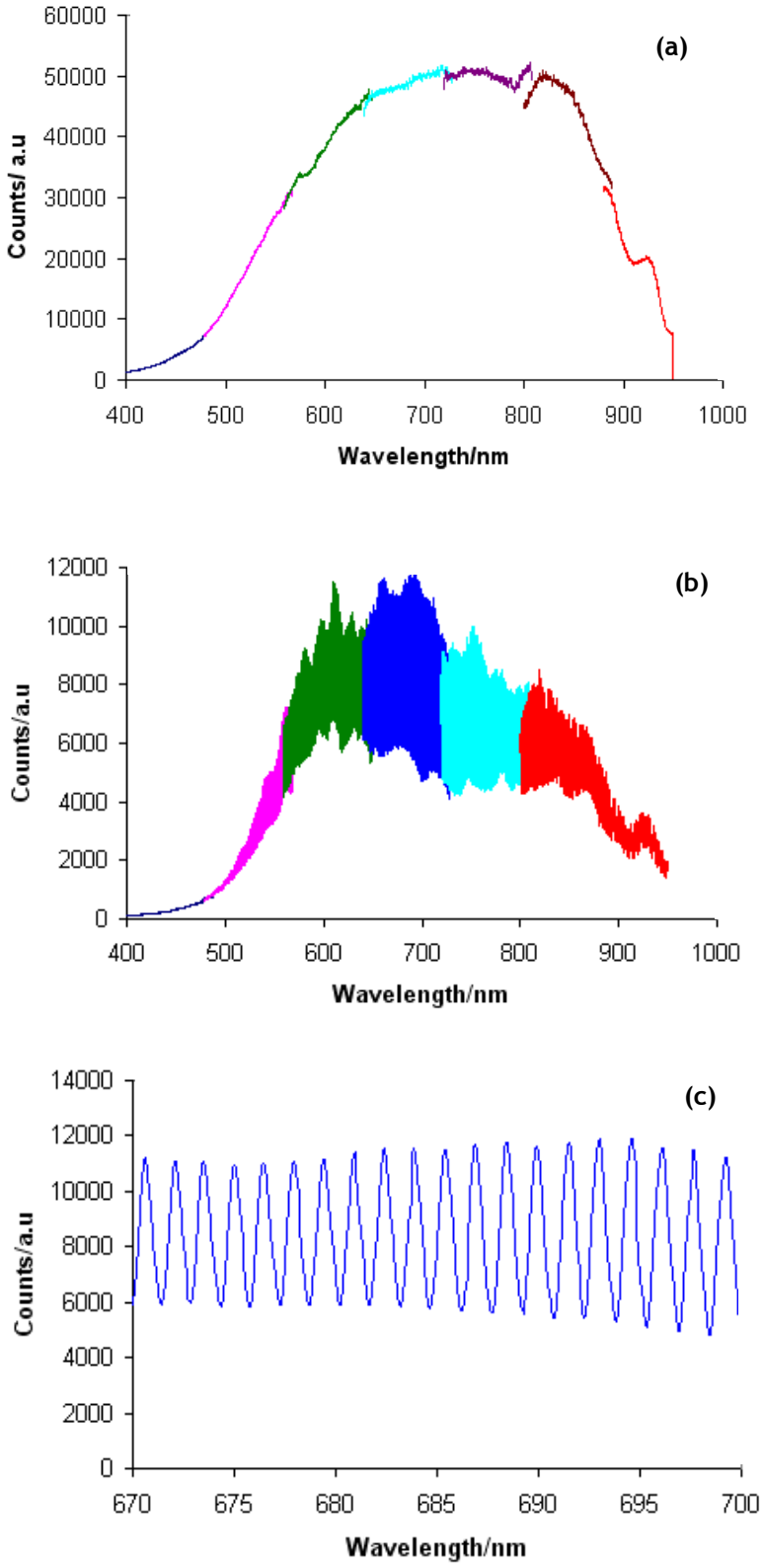

Figure 4.7: Optical response collected from the output waveguide. (a) Straight waveguide used as a reference to give the combined spectroscopic profile of the white light source, coupling optics and SU-8 waveguide; (b) The straight waveguide with one disk resonator and (c) Resonance peak within λ = 670 – 700 nm of wavelength.

Importantly, every cleaved device was tested by using this procedure. Only devices with fully developed structure, physically clean end-facet characteristics and the output intensity above 2000 counts were selected for functionalization and integration with the PDMS microfluidic channels, using the bonding steps as described in **Section 3.8**, **Chapter 3**.

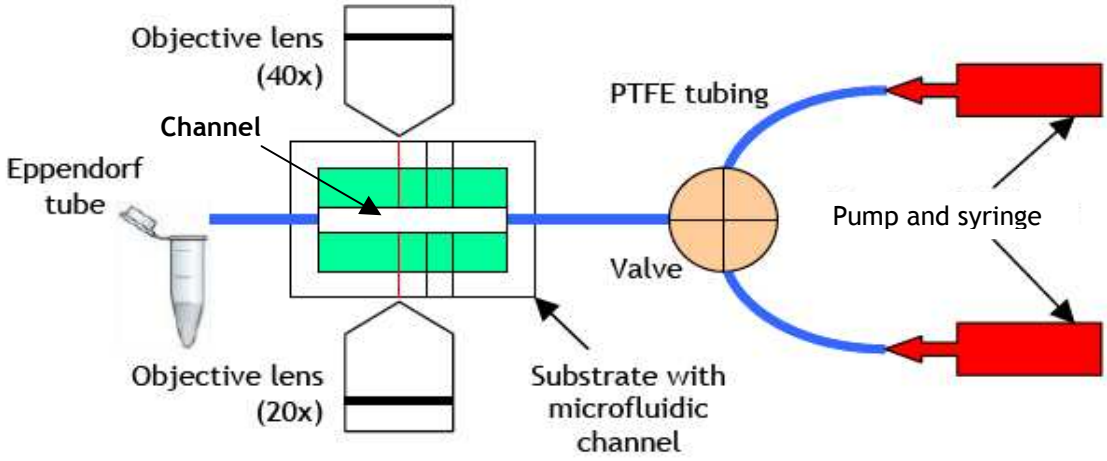

Figure 4.8: Schematic diagram of the experimental setup with the microfluidic system. Polytetrafluoroethylene (PTFE) is used as the tubing to deliver mixing solution into the channel, where the sensing area is located and aligned for measurement.

The schematic arrangement of the devices and equipment used for liquid transportation together with the other optical components is shown in **Figure 4.8**. Two 5 ml syringes were used in conjunction with two micro pumps APL1000 (World Precision Instrument Inc, USA). The maximum flow rates were determined by considering the channel size and viscosity of the fluids to make sure that the pressure did not rupture the microfluidic channel seal.

Typically, the flow rate was set at 0.050 ml/min for most experiments in this project. The syringes were connected to a control valve, so that different fluids could be selected during the experiment without disturbing the optical alignment. Finally, the fluid from the outlet channel was collected during the course of the experiment using Eppendorf® tubes so that the refractive index of aliquots of different mixtures could be analysed off-line using a standard Abbe refractometer (for comparison with shifts in the spectra observed with resonators devices, **Figure 4.9** shows a photograph of an actual microfluidic setup together with expanded schematic of a microfluidic device.

In order to make ensure a uniformity of the mixing and concentration of the solution, a magnetic bead mixing chamber was used to constantly stir the injected solution from the both pumps. Longer (~ 300 mm) of PTFE tubing for the inlet with 0.050 ml/min flow rates was used to

introduce a laminar flow into the microfluidic channel. Shorter PTFE tubing was used for the outlet to make sure that the solutions that has been probed on sensing chip was of a similar solution as the collected aliquots in the Eppendorf® tube. The distance between sensing area and collected tubing was approximately 10 mm.

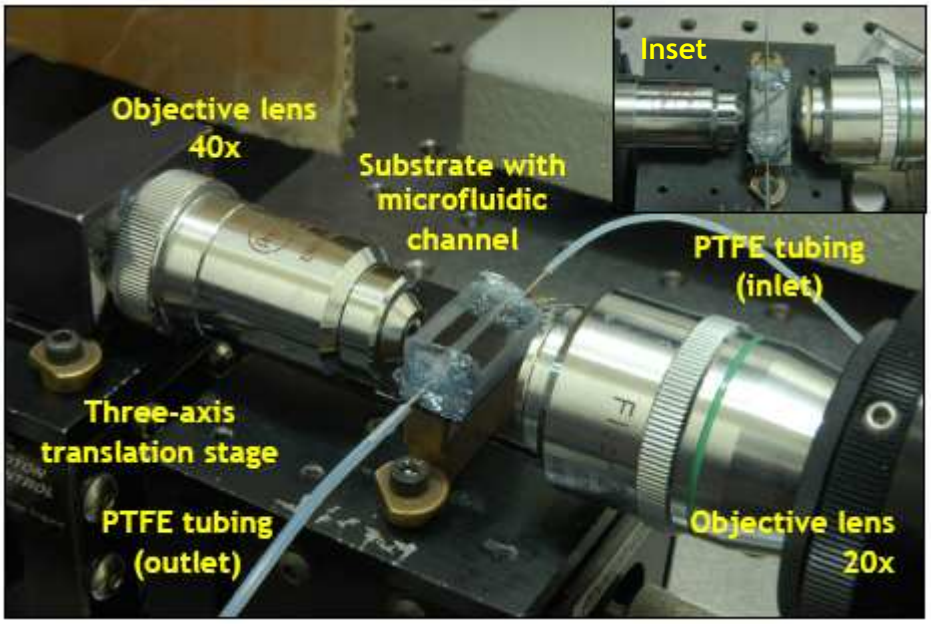

Figure 4.9(a): A part image of experimental setup with microfluidic system arrangement (inset: top view of the device).

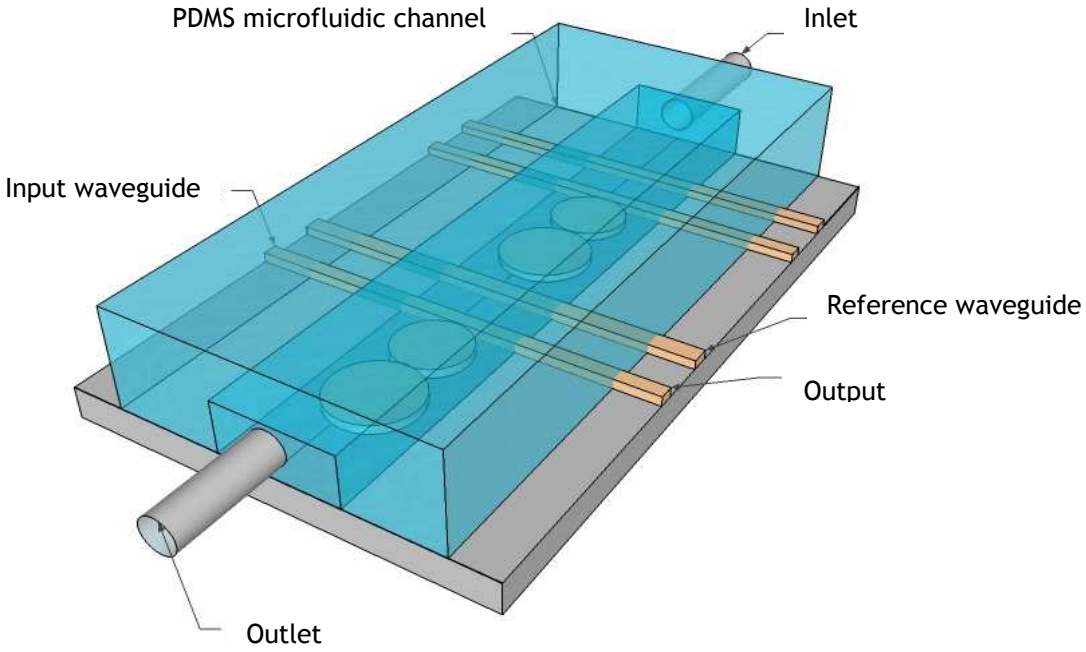

Figure 4.9(b): The three dimension (3D) illustration of the fabricated device on a Si/SiO_2 wafer integrated with microfluidic channel system. In order to seal the inlet and outlet of the

microfluidic channel, sealant 3145 RTV-Clear (Dow Corning Corp., USA) is used. The dimension of the channel is 500 µm (width) x 1000 µm (height). The PDMS microfluidic channel structure is bonded to the substrate after the cleaving process. All fabrication procedure is conducted in the JWNC cleanroom. (*Illustration is not an actual scale dimension*).

4.2.3 Polarization Dependence

Since the white light source used in this work emits unpolarized light, for comparison with ring resonator work performed using polarised lasers, it is important to investigate the effect of using either transverse magnetic (TM) or transverse electric (TE) light with the SU-8 structures that have been fabricated. To do this, a polarizer is used to control the polarization of light going into the input waveguide as shown in **Figure 4.10**.

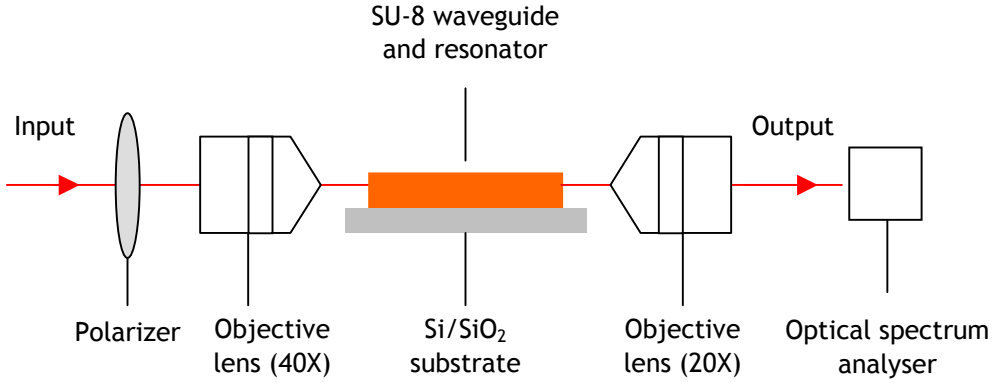

Figure 4.10: Schematic diagram of polarization experiment conducted to examine the dependency of the resonance wavelength upon the polarization of the input light. Polarizer is placed in front of the input objective lens; it was rotated according to the polarization angle (^{o}).

The light is coupled in and out of the SU-8 waveguide by objective lenses, and then the resonance output was collected by the optical spectrophotometer SPEX-500M. The polarizer is turned to 0^{o} and 90^{o} for TE and TM polarization respectively. The resonance output behaviour for both polarizations and unpolarized light is shown in **Figure 4.11**.

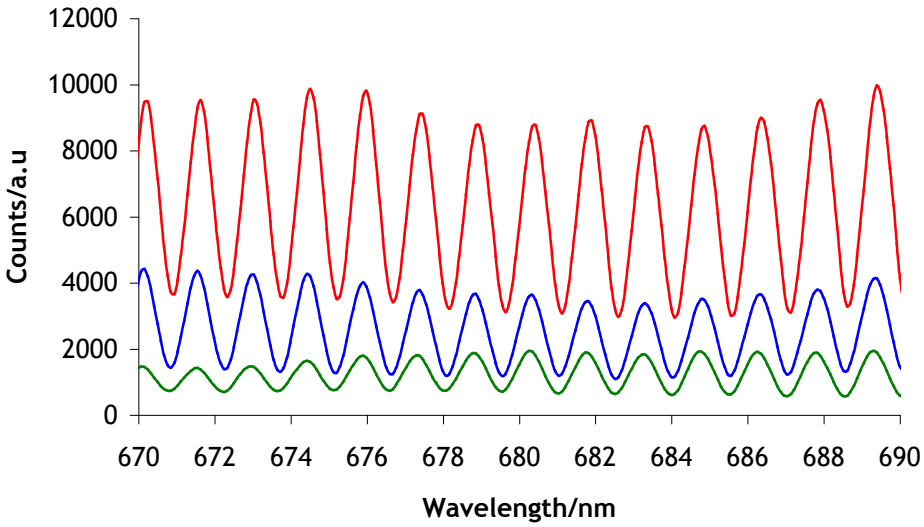

Figure 4.11: Resonance output response from a 40 μm gapless disk SU-8 resonator according to the TE polarization (blue line), TM polarization (green line) and unpolarized light (red line).

As illustrated in **Figure 4.11**, the throughput of unpolarized light is clearly the greatest of all three (9000 counts for off resonance features), compared to TE and TM polarized light transmission of only 4000 and 2000 counts respectively. The lower intensity for polarized light was in part due to the absorption of the polarizer, because at least half of the light is filtered out. The higher intensity for TE polarization light compared to TM polarized light suggests it is more highly confined inside the waveguide and resonator. The data showed that TM light underwent considerable leakage into the surrounding media (air), and this feature shows the advantage of TM polarization and can be exploited for surface sensing in an optical biosensor compared to the TE mode. It was also observed that there was a slight shift of resonance wavelength between TE and TM polarization due to the effective refractive index of different the modes during light propagation [8]. Importantly, the FSR values do not change with light polarization. From the observation, the plotted results shown that the changes of light polarization only influence the output count (intensity), but not the FSR value.

Since there were practical difficulties associated with the alignment of devices using the low throughput of TM polarised light, unpolarized light was used in the bulk experiments performed. It is appreciated however that this might have led to poorer detection sensitivity when material is absorbed on the resonator, the resonance TE and TM light are different e.g. if the shift of TM light is 0.4 nm and the shift of TE light is 0.1 nm, then the overall shift measured will be substantially less than 0.4 nm.

4.3 Characterizing the General Spectroscopic Response of Resonator Devices

Five different ring/disk resonator configurations were fabricated and characterised. Schematic of these are shown in **Figure 4.12** below and will be discussed individually in the following sections.

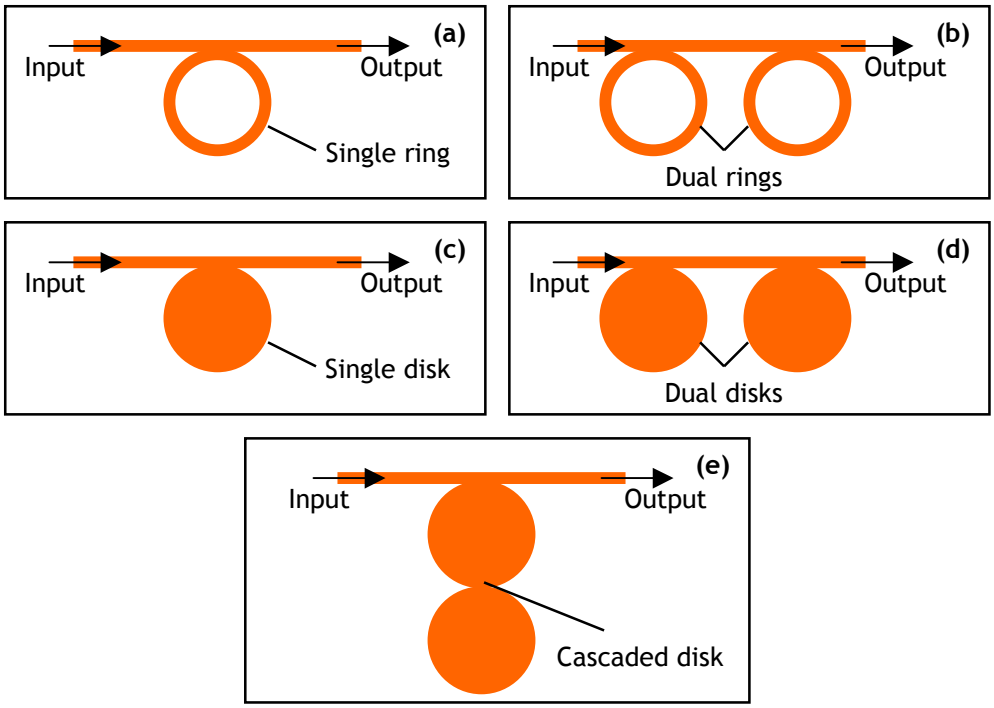

Figure 4.12: Schematic diagram of ring/disk resonator configuration. (a) Single ring; (b) Dual ring; (c) Single disk; (d) Dual disk and (e) Double-cascaded disk.

As mentioned before in the section on bending loss measurements, in order to avoid more than 50% of losses from the bending structure, simulations suggested that the curvature of the resonator structure must have a radius greater than 40 μm. To investigate this in detail, rings of three different sizes of radius have been fabricated (30, 40 and 50 μm). The first set of structures consists of gapless *ring* structures and the second set consists of gapless *disk* structures. The experimental setup employed the broad spectrum of the visible white light source, ranging from λ = 500 – 800 nm (as described in **Figure 4.4**). Generally, an integration time of 0.5 sec was used and an average of 5 spectra was collected.

4.3.1 Single Ring

In general, three sets of waveguide patterns were designed on each particular substrate and each resonator pattern has two reference waveguides for reference beam measurement and alignment. Initial experiments began with FSR measurements for the three different fabricated ring radii. Referring to the FSR equation in **Chapter 2**, the FSR value should be inversely proportional to the ring radius dimension. Thus, by increasing the dimension of the ring radius, the FSR value will decrease and vice versa.

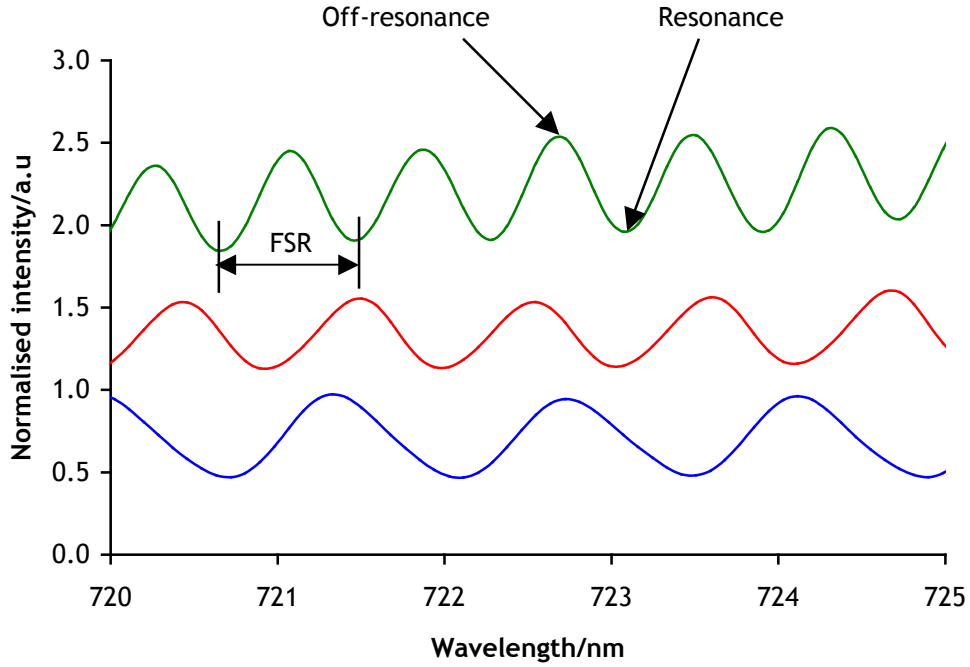

Figure 4.13: Optical response of ring resonators of different radius dimension in air. The resonance response represents the ring radii of 30 µm (blue line), 40 µm (red line) and 50 µm (green line). (Graph lines were displaced vertically for clarity).

For ring resonators of three different radii, **Figure 4.13** shows the variation in FSR value (measured as the wavelength difference between adjacent resonances). It can be observed that the FSR value reduces as the ring size increases from the smaller ring radius (30 µm) to the larger ring radius (50 µm). From the graph, measured FSR values of the ring resonator were 1.653 nm for a ring radius of 30 µm, 1.218 nm and 0.957 nm for the 40 µm and 50 µm rings respectively. Theoretical calculations (see **Equation 2.3**), predict that the FSR values should be 1.740 nm for 30µm, 1.305 nm for 40 µm and 1.044 nm for 50 µm. From the comparison of experimental and theoretical values, it can be concluded that the FSR of fabricated ring resonators was in good agreement with the calculated values. The calculated Q-factor for 30, 40 and 50 µm radii were 1381, 1182 and 1034 respectively.

Further experiments were performed to investigate the influence of a water environment as a sensing medium on the resonator response in **Figure 4.14**.

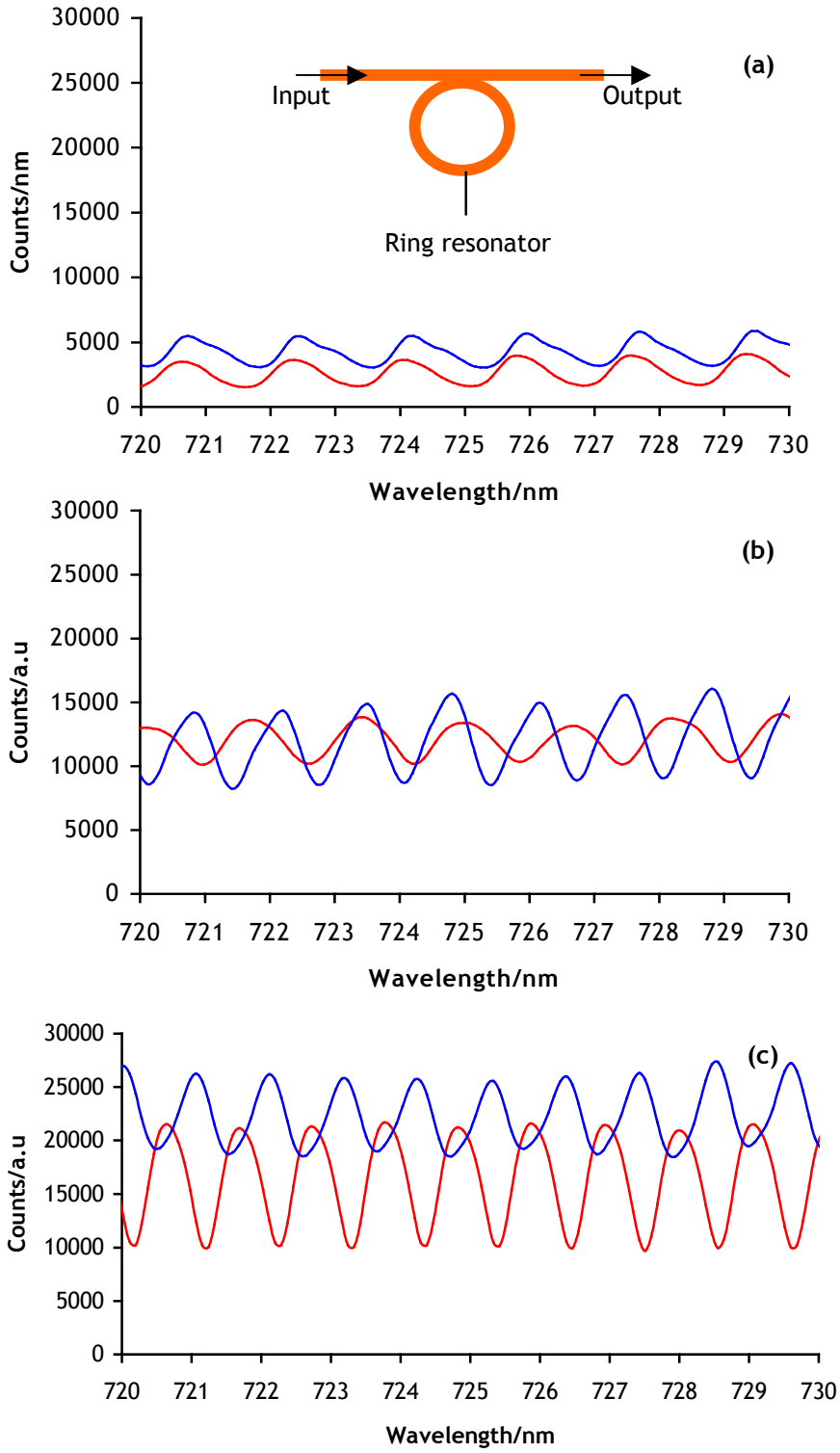

Figure 4.14: Resonance spectra collected from a single ring SU-8 resonator waveguide by different surrounding media. Air (n_{air} = 1.0) (red line) and water (n_{water} = 1.33)(blue line) medium and varied ring radii for (a) 30 μm; (b) 40 μm and (c) 50 μm.

The graphs in **Figure 4.14** shows the resonance output of gapless single ring resonator surrounded by either air or water cladding. Each spectrum was collected with the same integration time (0.5 s) and was plotted on the same graph for comparison. A significant difference in optical response can be seen by comparing the depth of resonance (defined as the difference in counts between adjacent on and off-resonance features).

For the 30 μm device (**Figure 4.14(a)**) the off-resonance transmission was ~ 3000 counts in air and depth of resonance was ~ 2000 counts. This depth of resonance increased to 3000 for the 40 μm device (**Figure 4.14(b)**) and 10,000 for the 50 μm ring (**Figure 4.14(c)**). This increase in depth with increasing ring series was also observed when the device were covered with a water droplet, here the depth went from 2000 counts at 30 μm to 5000 counts at 40 μm and 6000 counts at 50 μm.

Notably, when a droplet of DI water was pipetted onto a resonator structure, there was a significant increase in the transmitted signal for each size of resonator. A possible explanation for this is that, since the SU-8 structure becomes hydrophilic after O_2 plasma treatment, the water can spread and cover all of the ring resonator structure. This phenomenon would lead to water filling in small grooves in the sidewall roughness and narrow structure. As a result the roughness of both internal and external ring resonator surface will be reduced, leading to a reduction of light scattering[8] and improved total internal reflection (TIR) at the SU-8 boundary. In addition, the smaller difference between the core waveguide and surrounding media may increase the effective index of the waveguide and this will confine more light to propagate inside the resonator[9]. Analysis of the device with (30 μm and 50 μm) shows the similar differences.

4.3.2 Dual Rings

Figure 4.15 demonstrated that the optical resonance output of a dual ring resonator (illustrated inset) where both rings were of the same size. This configuration allows light propagating in the waveguide beyond the first ring to be filtered a second time by the second ring. This should dramatically increase the depth of resonance and help to distinguish the resonance features.

As shown in **Figure 4.15 (a) and (b)**, the depth of resonance for the 40 μm dual ring device was 6000 counts in air and 8000 counts in water. Whilst both of these values are only 2000 counts more than those for the 40 μm single ring device structure, the important different is that the off-resonance throughput for the dual ring device is much lower. This means that the normalised depth of resonance (i.e. off-resonance counts divided by resonance counts) is much larger and so resonance features can be more easily distinguished or resolved.

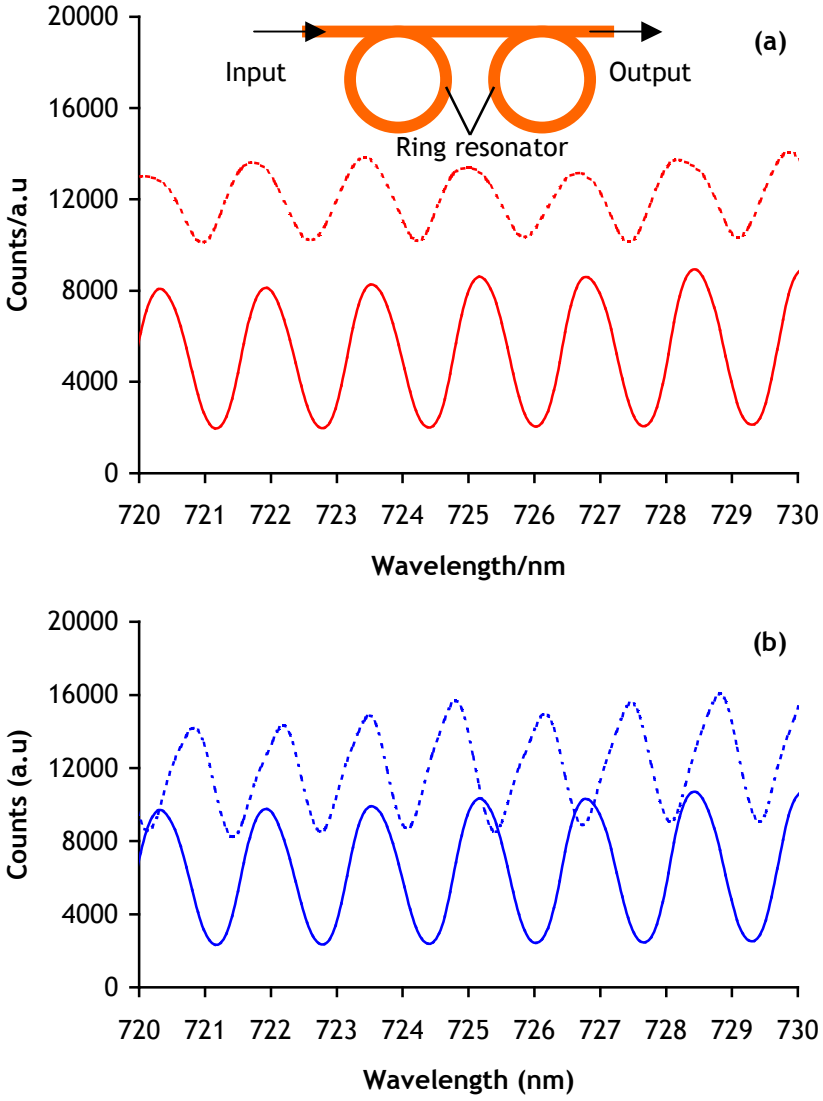

Figure 4.15: Comparison of resonance wavelength for single ring (dashed line) and dual ring resonators (solid line) upon different surrounding media, air (red line) and water (blue line).

Generally, as seen in the plotted graphs of **Figure 4.14** and **Figure 4.15**, the FSR values were unchanged when the structure was surrounded by water. Based on further investigation of one particular substrate (not shown in the thesis), the resonance wavelengths returned to their original (in air) values when the water was removed from the surface. Importantly, the SU-8 polymer structures showed no-changing or no-swelling effects when submerged in the water for extended periods of time (several hours). This attribute is important for sensing experiments involving liquid or aqueous media where the microfluidic channel was used to deliver different analytes and compounds.

4.3.3 Single Disk

A different potential resonator structure investigated was the disk resonator structure. Investigations were conducted on single disk, dual disks and double-cascaded disks resonator structures.

Figure 4.16(a) shows the comparison of resonance wavelengths for various single disk radii with air as a surrounding medium. The average off-resonance transmission for the single *disk* resonator with 40 μm radius was higher compared to that of the single *ring* resonator, shown in **Figure 4.14(a)** previously. It is thought that the reason for this is that the propagation of light inside the *disk* resonator is only confronted by the sidewall roughness of the disk's outside parameter, in contrast with *ring* resonator structures, where higher scattering of light would result from the interaction with the surface sidewall roughness of both inner and outer perimeter of the ring. As expected, similar FSR wavelength values are observed for disc radii at 1.566 for 30 μm, 1.218 for 40 μm and 0.957 for 50 μm, as for the ring structure.

Figure 4.16(b) illustrates the output resonator response when water was added onto the device. The changes average maximum peak of the resonance wavelength for 40 μm disk resonator increased significantly from 20,000 to 40,000 counts after being covered by water. This phenomenon was similar to that previously seen for ring structures (as in **Figure 4.14** and **Figure 4.15**).

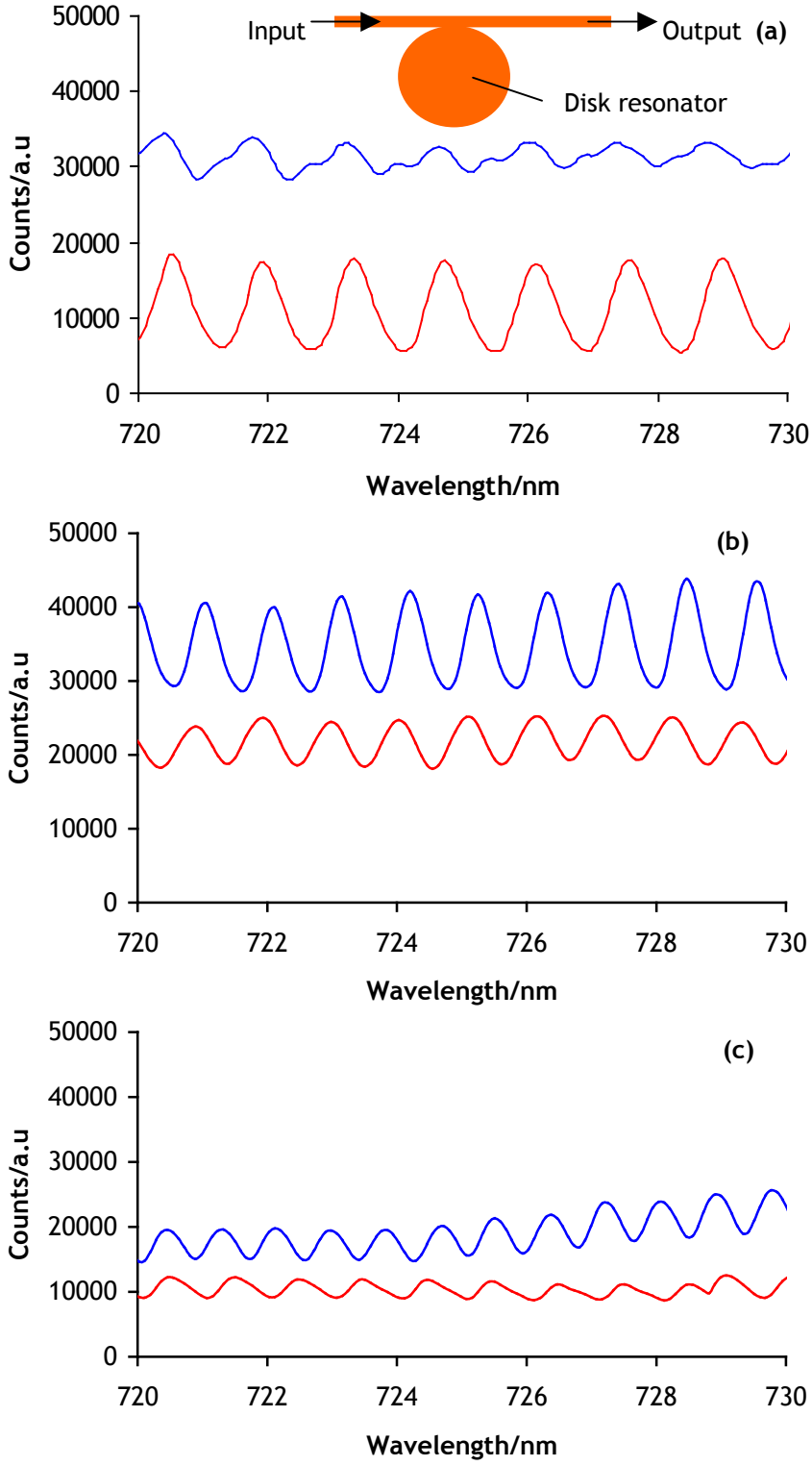

Figure 4.16: Comparison of output signal at different media, air (red line) and water (blue line) for varied radius of (a) 30 μm; (b) 40 μm and (c) 50 μm. In general, the counts value for each radius is increases when water is added into the sensing surface. The 40 μm disk radius shows the highest counts in the water condition experiment.

4.3.4 Dual Disks

Two gapless disk resonators with similar radius dimension were fabricated. These were designed to increase the separation between the average maximum and minimum peak of resonance response for better discrimination of the changes of the resonance peak during sensing experiments.

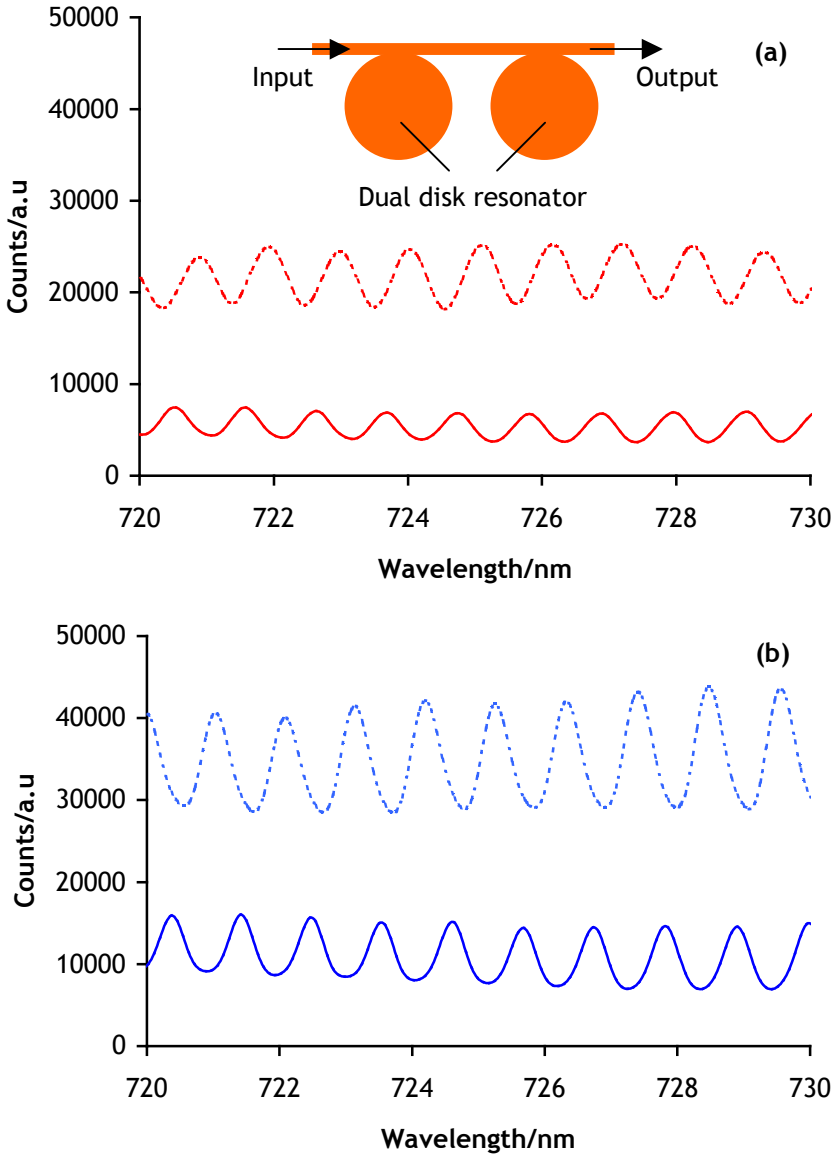

Figure 4.17: Optical response of single (dashed) dual disk (solid line) resonators structure of radius. Both disks are set at similar radius, 40 μm. The resonance pattern indicates that the sensing area is surrounded by air (red) and water (blue).

Figure 4.17 (a) shows a component of resonance output pattern of single and dual disk resonators. These similar effects were seen with the ring configurations, notably with the additional structure in the dual disk device, the propagated light encounters additional surface and sidewall roughness that cause the additional scattering. This would double the scattering loss effect [8] and decrease the output counts. As before, the normalised amplitude is bigger than for rings.

Figure 4.17(b) shows the intensity count value after water droplets were applied onto the test substrates. The comparison of outputs intensity before and after the water droplet action again shows decreasing in off-resonance transmission. The separation between off and on-resonance pattern was not as significant as in ring structures.

From analysis of these results, it can be concluded that the resonance wavelength pattern was successfully obtained from ring and disk structure of all three radius dimensions (30, 40 and 50 μm). The particular FSR obtained for each fabricated device was similar to that predicted from calculation. It demonstrated that the bending loss was the highest if the radius size was 30 μm and significantly less for 40 μm and 50 μm radii. In these latter two cases, data analysis showed that the resonance peaks were well resolved in both with air and water media. Since a larger FSR value leads to a better clarity of resonance shift in sensing experiments, 40 μm radius of resonance disk structure have been chosen, fabricated and tested for the double-cascaded disk resonator geometries discussed in the next section.

4.3.5 Double-cascaded Gapless Disk Resonator (DDR)

As discussed in **Chapter 2**, the refractive indices of the surrounding media have an important role in determining the resonance wavelength shift. According to the calculated and experimental FSR data for the 40 μm radius, the FSR within the 700 – 800 nm range was approximately 1.3 nm. In a sensing application, resonance wavelength shifts will happen when there is a difference of refractive index due to adsorption of the analytes detected by the resonators[10]. However, when a large difference of refractive index of surrounding media occurs, the resonance wavelength could shift by an amount as large as the resonator FSR or larger. This shift could lead to a problem in determining the value of the shifted resonance, since the shift in wavelength could be similar to the difference between adjacent resonance peaks in the original spectrum. A double-cascaded disk resonator was designed and fabricated (to overcome this potential difficulty).

Based on the vernier effect[11-14], a device having two touching disk resonator structures of different radii (40 μm and 42 μm) was fabricated. Gapless spacing between the straight waveguide and both disk resonators allowed the input light to propagate and directly coupled in and out onto the disk resonator structure efficiently. With the cascaded disks resonator arrangement [discussed in **Chapter 2**], the resonance response of both disk interact with each other inside the cavity, causing either suppression due to the destructive interference or enhancement due to constructive interference at specific wavelengths. This leads to the creation of a wider FSR in DDR structures and distinguishing of both very small and larger shifts in resonance correspond to the changes in surrounding refractive index.

Figure 4.18 shows a spectral scan from λ = 500 - 900 nm of a DDR structure. The output response from a single disk resonator and the DDR are plotted on the same graph to compare the output patterns.

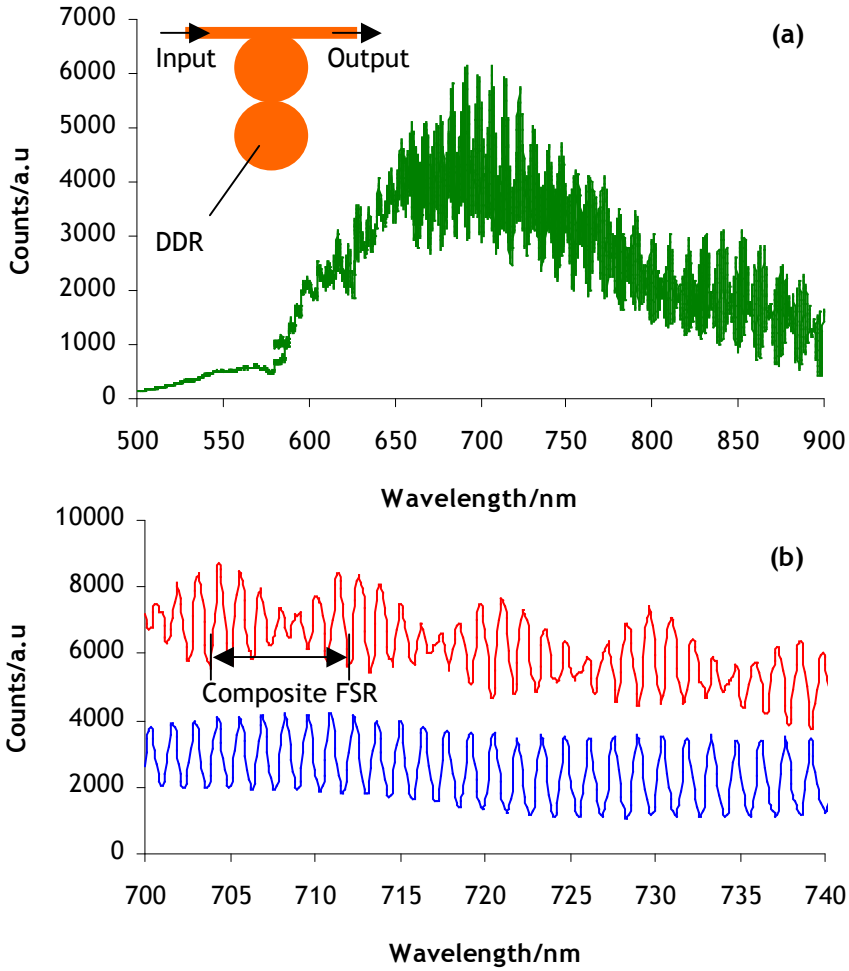

Figure 4.18: Output resonance collected from different micro-resonator configuration. (a) Full spectrum scan (green line) and (b) Optical resonance trait between dual disk (blue line) and DDR (red line).

Figure 4.18 (a) illustrates the resonance response of a DDR from 500 nm to 900 nm range of a white light source. It can be seen that the constructive and destructive interference between two dissimilar disk radii demonstrates the modulated group of resonance patterns. From the analysis, the composite FSR value was approximately 9.831 nm, compared to 10.0 nm predicted by simulations. This compares with 1.3 nm FSR for the dual disk device. **Figure 4.18 (b)** shows the comparison of the optical spectra between the 40 μm radius of the disk resonator with the DDR at the equivalent experimental parameters. The plotted data for double-cascaded disk resonator was vertically shifted for clarity.

In terms of experimental practicality, the pattern associated with the wider composite FSR provided a straightforward way to monitor resonance wavelength shifts compared to the uniformly and narrow FSR of the single and dual disk device. For example, if a large temperature drift caused a large resonance shift, this could be still detected with the wider FSR spacing since the resonance peak will not be overlapped onto the neighbouring peak when it is shifted. As with previous experiments on ring and disk structures, the intensity counts difference between on and off-resonance transmission were improved by adding the water onto the substrate (see **Figure 4.17**).

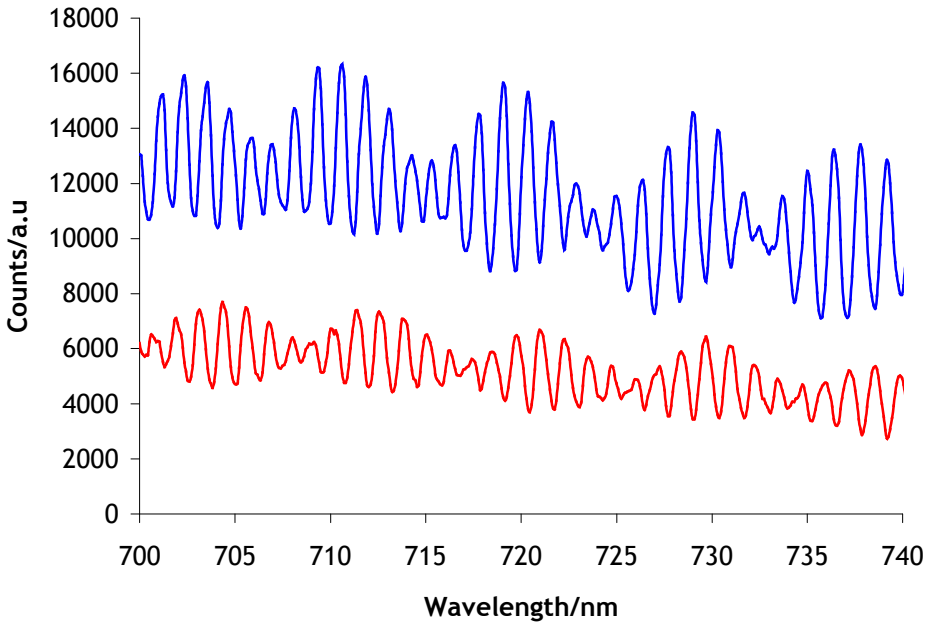

Figure 4.19: The spectra collected from the DDR by different surrounding media, air (red line) and water (blue line). Increasing counts value was observed when water is added onto the sensing surface. It was observed that the peak of composite FSR also shifted.

As shown in **Figure 4.19**, resonance spectra signals collected from the output waveguide of the DDR were compared before and after DI water was dropped onto the substrate. The average counts highlighted in the plotted graph for air was approximately 8,000. When DI water

was dropped onto the substrate, the count value increased by two-fold, leading to 16,000 counts.

4.4 Summary

Several experiments have been performed on five ring and disk geometry designs to characterise the resonance patterns. Each experiment was performed under identical conditions and acquisition parameters in order to compare the collected optical responses. Overall, single and dual resonator structures show the FSR values are similar to those calculated from theory [14] and vary according to the radius parameter. It can be seen that the output from a disk resonator device is, on average, twice that of an intensity counts over the ring resonator device. This is a consequence of the propagating light inside the ring structure being confronted by two sidewall roughness (the internal and external wall the ring of structure), compared to only one sidewall roughness of the disk resonator structure (the external wall). For all devices, it was observed that the intensity counts increased when water was added onto the substrate.

For a single resonator structure, shifts in the resonance wavelength shift were observed since the amplitude of adjacent resonance peak was similar and consequently it was difficult to reliably trace shifts of particular resonance correspond to changes in index of the solution media. However, a double-cascaded disk resonator structure showed the wider composite FSR and modulation of resonance amplitudes. This structure to the resonance pattern facilitates the ability to tracing resonance wavelength shift patterns, which is central to being able to use them as optical resonator biosensors.

References

[1] B. H. Ong, X. C. Yuan, and S. C. Tjin, "Adjustable refractive index modulation for a waveguide with SU-8 photoresist by dual-UV exposure lithography," Applied Optics, vol. 45, pp. 8036-8039, 2006.

[2] B. Y. Shew, C. H. Kuo, Y. C. Huang, and Y. H. Tsai, "UV-LIGA interferometer biosensor based on the SU-8 optical waveguide," Sensors and Actuators a-Physical, vol. 120, pp. 383-389, 2005.

[3] J. Deboer, R. J. Visser, and G. P. Melis, "Time-Resolved Determination of Volume Shrinkage and Refractive-Index Change of Thin Polymer-Films During Photopolymerization," Polymer, vol. 33, pp. 1123-1126, 1992.

[4] L. N. Jiang, K. P. Gerhardt, B. Myer, Y. Zohar, and S. Pau, "Evanescent-Wave Spectroscopy Using an SU-8 Waveguide for Rapid Quantitative Detection of Biomolecules," Journal of Microelectromechanical Systems, vol. 17, pp. 1495-1500, 2008.

[5] J. M. Cooper, J. Shen, F. M. Young, P. Connolly, J. R. Barker, and G. Moores, "The Imaging of Streptavidin and Avidin Using Scanning-Tunneling-Microscopy," Journal of Materials Science-Materials in Electronics, vol. 5, pp. 106-110, 1994.

[6] M. Lynch, C. Mosher, J. Huff, S. Nettikadan, J. Xu, and E. Henderson, "Functional nanoarrays for protein biomarker profiling," Nsti Nanotech 2004, Vol 1, Technical Proceedings, pp. 35-38501, 2004.

[7] D. Li, M. W. Frey, D. Vynias, and A. J. Baeumner, "Availability of biotin incorporated in electrospun PLA fibers for streptavidin binding," Polymer, vol. 48, pp. 6340-6347, 2007.

[8] C. Y. Chao and L. J. Guo, "Reduction of surface scattering loss in polymer microrings using thermal-reflow technique," Ieee Photonics Technology Letters, vol. 16, pp. 1498-1500, 2004.

[9] M. Nordstrom, D. A. Zauner, A. Boisen, and J. Hubner, "Single-mode waveguides with SU-8 polymer core and cladding for MOEMS applications," Journal of Lightwave Technology, vol. 25, pp. 1284-1289, 2007.

[10] R. W. Boyd and J. E. Heebner, "Sensitive disk resonator photonic biosensor," Applied Optics, vol. 40, pp. 5742-5747, 2001.

[11] R. Grover, V. Van, T. A. Ibrahim, P. P. Absil, L. C. Calhoun, F. G. Johnson, J. V. Hryniewicz, and P. T. Ho, "Parallel-cascaded semiconductor microring resonators for high-order and wide-FSR filters," Journal of Lightwave Technology, vol. 20, pp. 872-877, 2002.

[12] S. Mandal, K. Dasgupta, T. K. Basak, and S. K. Ghosh, "A generalized approach for modeling and analysis of ring-resonator performance as optical filter," Optics Communications, vol. 264, pp. 97-104, 2006.

[13] K. Oda, N. Takato, and H. Toba, "A Wide-Fsr Wave-Guide Double-Ring Resonator for Optical Fdm Transmission-Systems," Journal of Lightwave Technology, vol. 9, pp. 728-736, 1991.

[14] Heebner, J., Grover, R. and Ibrahim T.A. Optical Microresonators: Theory, Fabrication and Applications; Springer Series in Optical Sciences; Springer-Verlag London, U.K 2008

[15] Bellingham & Stanley Ltd, UK [Online]. Available: http://www.bellinghamandstanley.com/

[16] Horiba Corp, Japan [Online] http://www.horiba.com/

[17] MicroChem Corp, USA [Online] http://www.microchem.com/

[18] Veeco, USA [Online] http://www.veeco.com/

[19] Andor Technology Plc, UK [Online]. Available : http://www.andor.com/

[20] Ocean Optics, USA [Online] Available: http://www.oceanoptics.com/

[21] CVI Melles Griot, USA [Online] Available: http://www.cvimellesgriot.com/

[22] Osram GmbH, Germany [Online] Available: http://www.osram.com/

[23] Horiba Ltd, Japan [Online] Available: http://www.horiba.com/scientific/products/raman-spectroscopy/software/

[24] World Precision Instrument Inc, USA [Online] http://www.wpiinc.com/

[25] Dow Corning Corp, USA [Online] http://www.dowcorning.com/

CHAPTER 5

Biological Immobilization Protocol

5.1 Evaluating Technique for Protein Immobilization on SU-8 Substrates

5.1.1 Introduction

As briefly discussed in **Chapter 1**, one of the common ways to make a biosensor involves attaching to a sensor surface that can recognize specific biological molecules in an analyte solution. In this section, the processes that were involved in protein immobilization on the SU-8 disk resonators are described. The aims for this section are to explore the different protocols to immobilize biotin and to determine which one can be best performed for specific biotin-streptavidin binding inside the PDMS microfluidic channel placed over the optical resonator device. This involved determining the functional groups on the SU-8 polymer surface, using different protocols for immobilization, and then assessing the surface coverage. Two established methods (fluorescence microscopy and X-ray photoelectron spectroscopy (XPS)) were used for characterizing of the degree of surface functionalization. It should be appreciated that since the fabrication of the electron beam written device is relatively expensive and the optical measurements are an involved process, it is important to optimise and be confident in the surface functionalization aspect of the biosensor fabrication process. Failure to do this could give rise to misleading interpretation of optical measurements.

5.1.2 Pre-treatment Protocol

As can be seen from (**Figure 3.4, Chapter 3**), SU-8 polymers have epoxy groups and hydroxyl (-OH) groups on the surface after the development process and hard baked process. Since both of these groups are relatively unreactive, in order to immobilise biomolecules for protein binding studies, the SU-8 surface needs to be activated. Several protocols have been published on SU-8 polymer surface modification in order to introduce, for example IgG protein[1], DNA[2], human IgG[3][4], human growth hormone (hGH)[5] and mouse IgG[6]. Generally, the methods used have used techniques to generate functional groups such as hydroxyl (-OH), amine (NH_2), thiol (S-H) and aldehyde (-CHO) onto the SU-8 surface so that they can form covalent bonds with an appropriate biosensing molecule. One of the preferred methods was constructing amine groups on the SU-8 polymer surface by using an aminosilane treatment[3][6]. In that work, hydroxyl groups (-OH) were formed on SU-8 surface by dipping the substrates into a concentrated chromic acid solution ($K_2Cr_2O_7$ and sulphuric acid H_2SO_4)[3][6]. According to this treatment, the epoxy groups of the SU-8 open up due to the high acidity of the solution[1] and react with oxygen (provided by dichromate) to form hydroxyl (-OH) and carbonate (CO_2H) groups.

5.2 Optical microscopy: Fluorescein isothiocyanate (FITC)

5.2.1 Introduction

In order to determine the presence of the functional groups of SU-8 polymer after the pre-treatment processes, a simple protocol was devised based on the reaction between a fluorescent molecule and amino group that generate after O_2 plasma treatment. Thus, samples of SU-8 on either glass or Si/SiO_2 substrates were examined using fluorescence microscopy after different steps in the immobilization protocol as in **Figure 5.2**.

5.2.2 Materials and Methods

SU-8 resist (MicroChem Corp, USA) is used as a fabrication structure. For the pre-treatment step, instead of using chromic acid (which may destroy lithographic features), the samples were treated under an O_2 plasma for 30 s at 100W. They were incubated in a desiccator with 3-aminopropyl triethoxysilane (APTES 99%) (Sigma Aldrich, USA) (see **Appendix A.5.1**) under vapour conditions overnight at 65^{o}C. All samples (treated and un-treated) were incubated with fluorescein isothiocyanate (FITC) (Sigma Aldrich, USA) dissolved in dimethyl sulfoxide (DMSO) (Sigma Aldrich, USA) for 1 hour at room temperature. After rinsing and drying, they were examined under the optical microscope Axio Observer (Zeiss AG, Germany), different objective lenses (10X, 20X and 40X) with help of an FITC No.1 filter (Zeiss AG, Germany) as shown in **Figure 5.2**. Full protocol of SU-8 functional group detection can be found in **Appendix A.5.2**.

Figure 5.1: FITC reaction with a primary amine compound.

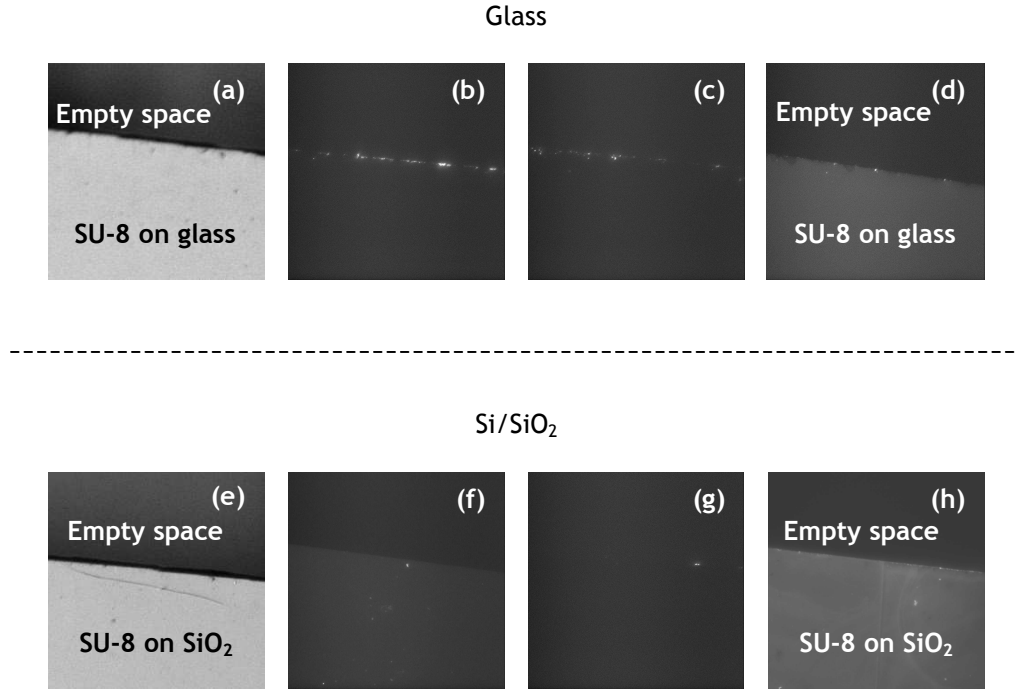

Figure 5.2: Images of glass/SU-8 and SiO_2/SU-8 samples at different treatment process at 10x magnification. (a) Bright field image of SU-8 on glass substrate, (b) Glass/SU-8 substrate and FITC; (c) Glass/SU-8 substrates, 5 min O_2 plasma and FITC; (d) Glass/SU-8 substrate, O_2 plasma, APTES 99% and FITC; (e) Bright field image of SU-8 on SiO_2 substrate; (f) Si/SiO_2/SU-8 substrate and FITC; (g) Si/SiO_2/SU-8 substrate, 5 min O2 plasma and FITC and (h) Si/SiO_2/SU-8 substrate, O_2 plasma, APTES 99% and FITC.

All of the images in **Figure 5.2** were captured at the same exposure time of 1.2 s and displayed on a 0 - 6000 intensity counts scale for comparative analysis. On this scale, the auto fluorescence of SU-8 polymer that appeared at a level of 300-600 counts is not discernable: i.e. no fluorescence image is observed in **Figure 5.2(a)** and **Figure 5.2(d)**, the control samples.

As can be seen from **Figure 5.2(b)** and **Figure 5.2(e)** when the untreated O_2 plasma samples were treated with the FITC solution, the fluorescence counts intensity increased. However, when the plasma treated samples were reacted with aminosilane, a large number of amine groups were introduced onto the surface, as evidenced by the large increase in fluorescence following FITC incubation as shown in **Figure 5.2 (c) and (f)**. From this preliminary FITC testing result, treatment of the SU-8 surface by aminosilane was a suitable means of functionalization with NH_2 groups for investigations on protein immobilization that were conducted throughout this thesis.

To test which aspects of the pre-treatment procedure in **Figure 5.2** were absolutely necessary, a further series of experiments were performed. To examine if the O_2 plasma process had been effective in breaking the epoxy groups bond or whether any remained on the SU-8 surface, a set of experiments were constructed in which ethylenediamine ($C_2H_8N_2$) (Sigma Aldrich, USA) was used as a potential surface modifier that reacted directly with epoxy groups. This was carried out because pervious work had reported, instead of hydroxyl group (-OH) on SU-8 surface after plasma treatment[7], there was a possibility that the epoxy group[8] remained intact. Thus, a protein immobilization protocol was performed with one set of samples prepared using 0.1M sulphuric acid (H_2SO_4) (Sigma-Aldrich, USA) treatment after the plasma step, and a second set prepared using ethylenediamine ($C_2H_8N_2$) treatment. Following either of these pre-treatment, the samples were then treated with APTES 98%, biotinamidohexanoyl-6-aminohexanoic acid N-hydroxysuccinimide ester (NHS-biotin)(Sigma-Aldrich, USA) and finally streptavidin with FITC conjugates [9] as shown in the grid of **Table 5.1**. As before, substrates were viewed under the microscope and fluorescence counts were recorded for analysis and comparison using ImageJ software (see **Figure 5.3**).

Table 5.1: SU-8 pattern treatments correspond to the selected steps.

Sample					
A1	O_2 plasma	H_2SO_4			
A2	O_2 plasma	H_2SO_4	APTES 99%		
A3	O_2 plasma	H_2SO_4	APTES 99%	NHS-biotin	
A4	O_2 plasma	H_2SO_4	APTES 99%	NHS-biotin	streptavidin-FITC
A5	O_2 plasma	H_2SO_4	APTES 99%		streptavidin-FITC
A6	O_2 plasma	H_2SO_4		NHS-biotin	streptavidin-FITC
A7	O_2 plasma	H_2SO_4			streptavidin-FITC
A8	O_2 plasma				streptavidin-FITC

Sample					
B1	O_2 plasma	$C_2H_8N_2$			
B2	O_2 plasma	$C_2H_8N_2$	APTES 99%		
B3	O_2 plasma	$C_2H_8N_2$	APTES 99%	NHS-biotin	
B4	O_2 plasma	$C_2H_8N_2$	APTES 99%	NHS-biotin	streptavidin-FITC
B5	O_2 plasma	$C_2H_8N_2$	APTES 99%		streptavidin-FITC
B6	O_2 plasma	$C_2H_8N_2$		NHS-biotin	streptavidin-FITC
B7	O_2 plasma	$C_2H_8N_2$			streptavidin-FITC
B8	O_2 plasma				streptavidin-FITC

Table 5.1 shows a succession of the SU-8 samples in which none, one or more of the immobilization steps has been emitted. This allows determination of which steps are crucial to efficient immobilization of streptavidin.

Figure 5.3(a) Fluorescence images of the SU-8 pattern on Si/SiO_2 substrate taken by optical microscope with FITC filter. (A0) Bright field image of SU-8 pattern (square) on the SiO_2 substrate, (A1) O_2 plasma and H_2SO_4; (A2) O_2 plasma, H_2SO_4 and APTES 99%; (A3) O_2 plasma, H_2SO_4, APTES 99% and NHS-biotin incubation; (A4) O_2 plasma, H_2SO_4, APTES 99%, NHS-biotin and streptavidin-FITC incubation.

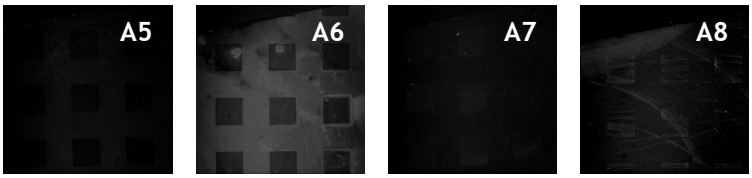

Figure 5.3(b) Fluorescence images of the SU-8 pattern on Si/SiO_2 substrate taken by optical microscope with FITC filter. (A5) O_2 plasma, H_2SO_4, APTES 99% and streptavidin-FITC; (A6) O_2 plasma, H_2SO_4, NHS-biotin and streptavidin-FITC (dark square is SU-8 pattern); (A7) O_2 plasma, H_2SO_4 and streptavidin-FITC; (A8) O_2 plasma and streptavidin-FITC incubation.

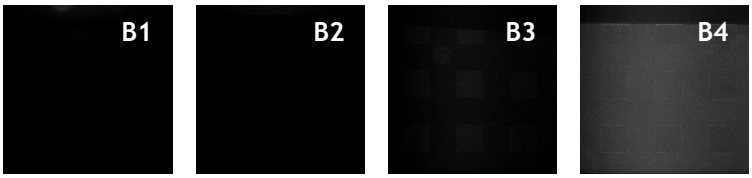

Figure 5.3(c) Fluorescence images of the SU-8 pattern on Si/SiO_2 substrate taken by optical microscope with FITC filter. (B1) O_2 plasma and ethylenediamine; (B2) O_2 plasma, ethylenediamine and APTES 99%; (B3) O_2 plasma, ethylenediamine, APTES 99% and NHS-biotin incubation; (B4) O_2 plasma, ethylenediamine, APTES 99%, NHS-biotin and streptavidin-FITC incubation.

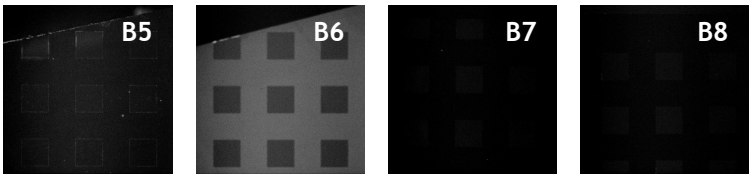

Figure 5.3(d) Fluorescence images of the SU-8 pattern on Si/SiO_2 substrate taken by optical microscope with FITC filter. (B5) O_2 plasma, ethylenediamine, APTES 99% and streptavidin-FITC; (B6) O_2 plasma, ethylenediamine, NHS-biotin and streptavidin-FITC (dark square is SU-8 pattern); (B7) O_2 plasma, ethylenediamine and streptavidin-FITC; (B8) O_2 plasma and streptavidin-FITC incubation.

Each image represents in Figure 5.3 (a-d) shows the SU-8 pattern on the SiO_2 substrates at 10x magnification. Images collected for 1.2 s and displayed on a 360-2000 intensity scale (the SU-8 autofluorescence in 100-600 counts).

In **Figure 5.3** autofluorescence counts have been subtracted using Andor Solis Imaging software (Andor Technology, UK) before analysing in ImageJ. Clearly, it can be seen that there was no fluorescence on the set of samples that had not been treated with streptavidin-FITC as in Figure 5.3 (A1-A3) and Figure 5.3 (B1-B3). However, for the samples treated with each step of the protocol, Figure 5.3 (A4) and (B4) there is a fluorescence signal over both the patterned SU-8 and background substrate areas. This was possibly because the NHS-biotin was reacted equally well with the SU-8 pattern and SiO_2 surfaces (as suggested by comparison of A4 and A6).

Importantly, it could be deduced that the streptavidin was bound via the biotin group by examining the fluorescence image of samples in which the NHS-biotin stage was omitted as in Figure 5.3 (A5 and B5).

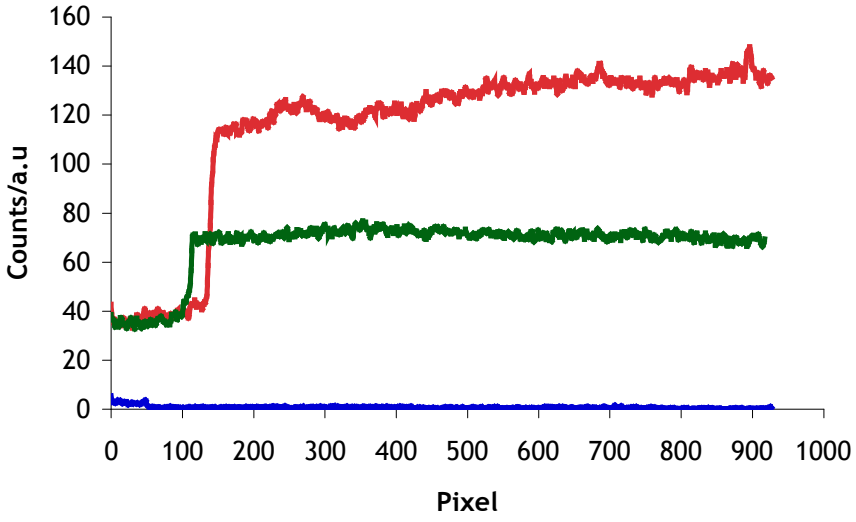

Figure 5.4: Comparison of fluorescence intensity counts across the fluorescence image substrate, A1 (blue line), A4 (red line) and B4 (green line).

To examine which of H_2SO_4 or ethylenediamine is more efficient at activating the plasma treated SU-8 surface, **Figure 5.4** illustrates the intensity counts of fluorescence signal for a line trace across the SU-8 pattern of samples subjected to the complete immobilization protocols. Also shown are the fluorescence counts for sample (A1), as reference. The plotted graph shows that the average counts for the H_2SO_4 sample (A4) was approximately 130 counts/pixel while for the ethylenediamine treated sample (B4), there were only 70 counts/pixel on average. This demonstrated that there was higher concentration of biotin-streptavidin-FITC binding on the surface of the H_2SO_4 sample (A4) compared to the sample with the ethylenediamine step (B4).

This result shows the tendency of an epoxy ring to remain open after the ashing process and form -OH groups under the higher acidity conditions of 0.1M H_2SO_4[1].

In conclusion, H_2SO_4 pre-treatment as part of the protein immobilization protocol was found to be the route to obtain the highest coverage of biotin and streptavidin on the SU-8 surface.

5.3 XPS Characterization

5.3.1 Introduction

Further experiments conducted to optimise the H_2SO_4 pre-treatment option for protein immobilization involved the use of XPS to characterise the functional group present on the SU-8 surface. SU-8 pattern was modified using the immobilization protocol [**Appendix A.5.3**].

5.3.2 Materials and Methods

Thus, a series of 19 diced SU-8 (MicroChem, USA) fabricated samples, with the dimension of 10 x 10 mm, were prepared and treated as shown in **Table 5.2** below:

Table 5.2: XPS samples at different preparation steps of immobilization protocol.

Sample							Notes
C1	SU-8	O_2 Plasma	H_2SO_4				
C2	SU-8	O_2 Plasma	H_2SO_4	APTES			
C3	SU-8	O_2 Plasma	H_2SO_4	APTES	NHS-biotin		no streptavidin-FITC
C4	SU-8	O_2 Plasma	H_2SO_4	APTES	NHS-biotin	strept-FITC	
C5	SU-8	O_2 Plasma	H_2SO_4	APTES		strept-FITC	no NHS-biotin
C6	SU-8	O_2 Plasma	H_2SO_4		NHS-biotin	strept-FITC	no APTES
C7	SU-8	O_2 Plasma	H_2SO_4			strept-FITC	no APTES - no biotin
C8	SU-8	O_2 Plasma				strept-FITC	no H_2SO_4-APTES-Biotin
C9	SU-8	O_2 Plasma	H_2SO_4		NHS-biotin		no APTES - no St
C10	SU-8	O_2 Plasma		APTES	NHS-biotin	strept-FITC	O_2 plasma 30sec @ 100W
C11	SU-8	O_2 Plasma		APTES	NHS-biotin	strept-FITC	O_2 plasma 5 min @ 100W
C12	SU-8			APTES	NHS-biotin	strept-FITC	no O_2 plasma- no H_2SO_4
C13	SU-8				NHS-biotin	strept-FITC	
C14	SU-8		H_2SO_4	APTES	NHS-biotin	strept-FITC	no O_2 plasma
C15	SU-8	O_2 Plasma					30 sec @100W
C16	SU-8	O_2 Plasma					5 min @100W
C17	SU-8	O_2 Plasma					5 min @200W
C18	SU-8	O_2 Plasma					30 sec @200W
C19	SU-8						

Each of the samples was characterised using Axio Observer (Zeiss AG, Germany) optical microscope with fluorescence filter setup, and captured images are shown in **Figure 5.5**, prior to performing the XPS measurement. From visual inspection, of Figure 5.5, the samples that have brightest fluorescence (C4, C10, C11, C12 and C14), are those in which APTES 99%, NHS-biotin, and streptavidin-FITC have been used, with or without either O_2 plasma or H_2SO_4 pre-treatment. From a comparison of these the brightest (highest) total coverage is obtained when both O_2 plasma and H_2SO_4 are used.

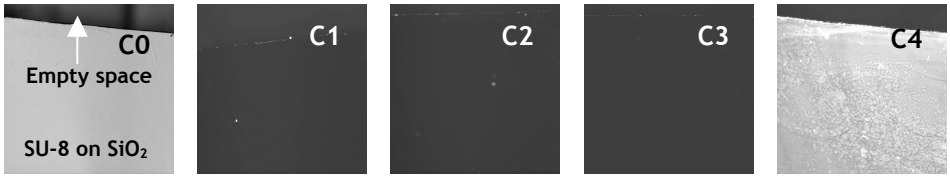

Figure 5.5(a) Fluorescence images of the SU-8 pattern on Si/SiO_2 substrate taken by optical microscope with FITC filter based on specific steps. (C0) Bright field image of SU-8 on SiO_2 (C1) O_2 plasma and H_2SO_4; (C2) O_2 plasma,H_2SO_4 and APTES 99%; (C3) O_2 plasma, H_2SO_4, APTES 99% and NHS-biotin incubation; (C4) O_2 plasma, H_2SO_4, APTES 99%, NHS-biotin and streptavidin-FITC incubation.

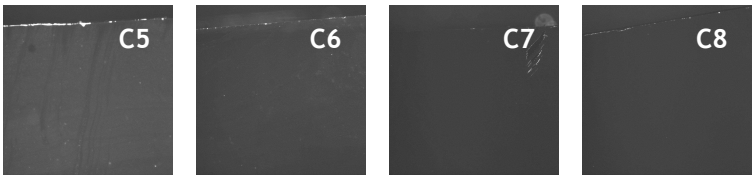

Figure 5.5(b) Fluorescence images of the SU-8 pattern on Si/SiO_2 substrate taken by optical microscope with FITC filter based on specific steps. (C5) O_2 plasma, H_2SO_4, APTES 99% and streptavidin-FITC; (C6) O_2 plasma, H_2SO_4, NHS-biotin and streptavidin-FITC; (C7) O_2 plasma, H_2SO_4, and streptavidin-FITC (C8) O_2 plasma and streptavidin-FITC incubation.

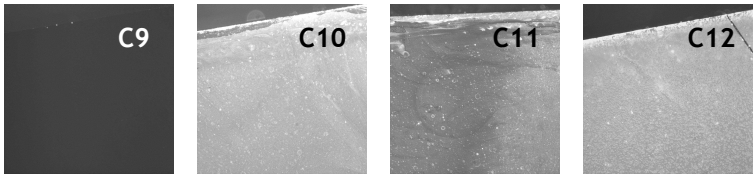

Figure 5.5(c) Fluorescence images of the SU-8 pattern on Si/SiO_2 substrate taken by optical microscope with FITC filter based on specific steps. (C9) O_2 plasma, H_2SO_4, and NHS-biotin; (C10)

O_2 plasma (30 s), APTES 99%, NHS-biotin and streptavidin-FITC; (C11) O_2 plasma (5 min), APTES 99%, NHS-biotin and streptavidin-FITC and (C12) APTES 99%, NHS-biotin and streptavidin-FITC incubation.

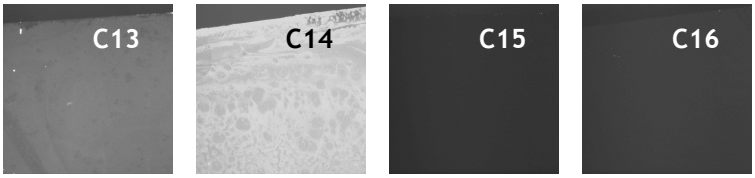

Figure 5.5(d) Fluorescence images of the SU-8 pattern on Si/SiO_2 substrate taken by optical microscope with FITC filter based on specific steps. (C13) NHS-biotin and streptavidin-FITC; (C14) H_2SO_4, APTES 99%, NHS-biotin and streptavidin-FITC; (C15) O_2 plasma (30 s, 100W) and (C16) O_2 plasma (5 min, 100W).

Figure 5.5(e) Fluorescence images of the SU-8 pattern on Si/SiO_2 substrate taken by optical microscope with FITC filter based on specific steps. (C17) O_2 plasma (5 min, 100W); (C18) O_2 plasma (5 min, 200W) and (C19) Control SU-8 (untreated).

Figure 5.5 (a-e): All images from samples are captured before the XPS instrument was used. Samples were labelled according to the Table 5.3.

5.3.3 XPS Instrument and Measurement

A Scienta ECSA 300 High resolution XPS at the National Centre of Electron Spectroscopy and Surface Analysis (NCESS) located at Daresbury Laboratory was used to assay the surface group present following different immobilization protocols. Samples were loaded into the ultra high vacuum sample chamber and the electron take off angle was fine-tuned at 13.0^o to obtain the best surface sensitivity. Scanning time and flood gun (FG) energy values were set according to the calibration procedure[10]. Survey scans were performed on the sample surface, followed by high-resolution scans over regions corresponding to specific elements such as carbon C(1s), nitrogen N(1s), oxygen O(1s) and sulphur S(2p). The integration times were typically around 20-60 min for specific regions. Further information about the XPS technique can be found in

[**Appendix A.5.4**]. Each sample scan was recorded and the collected spectrum was analysed by CasaXPS version 2.3.15 processing software (**Casa Software Ltd, UK**).

The XPS technique quantifies the binding energy of electrons emitted from the surface (that referred to photoelectron) after X-ray irradiation. This energy is characteristic of the elements and their bonding environment in the surface of the sample thus the chemical composition can be determined by measuring the binding energy peak positions.

Although all of the samples (see **Table 5.2**) were measured in the XPS machine, only a small number of experimentally significant samples will be discussed here. A basic survey scan on the sample surface gave the survey peak of element binding energy (eV), it has a broad range of binding energy (eV) started from 1200 eV until 0 eV.

Figure 5.6(a) shows the survey scan for a plasma (O_2) and acid (H_2SO_4) treated SU-8 surface as a pre-treated sample. The only elements present are C and O. Meanwhile, when the sample was treated with APTES 99%, the survey scan demonstrated that a nitrogen N(1s) species had been incorporated on the sample surface. From the detailed C(1s) region scans (**Figure 5.7(a)** and **Figure 5.7(b))**, it can be seen that there is a change in bonding of the carbon species: The count for the C-C binding peak at 285 eV and CO_2H at 287 eV were reduced after the aminosilane was introduced and a feature corresponding to the C-N binding species appeared at 286.5 eV[11-14]. Significantly, **Figure 5.7(c)** revealed that the nitrogen N(1s) species was only present in the aminosilane treated sample, further confirming that the aminosilane step was successful.

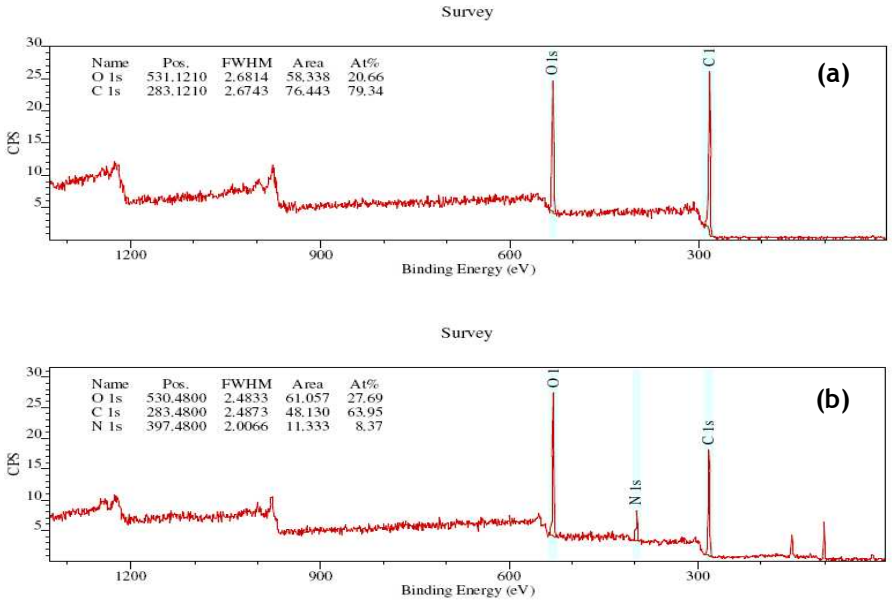

Figure 5.6: The XPS survey spectra on SU-8 samples. (a) O_2 plasma and H_2SO_4 (C1) and (b) O_2 plasma, H_2SO_4 and APTES 99% (C2).

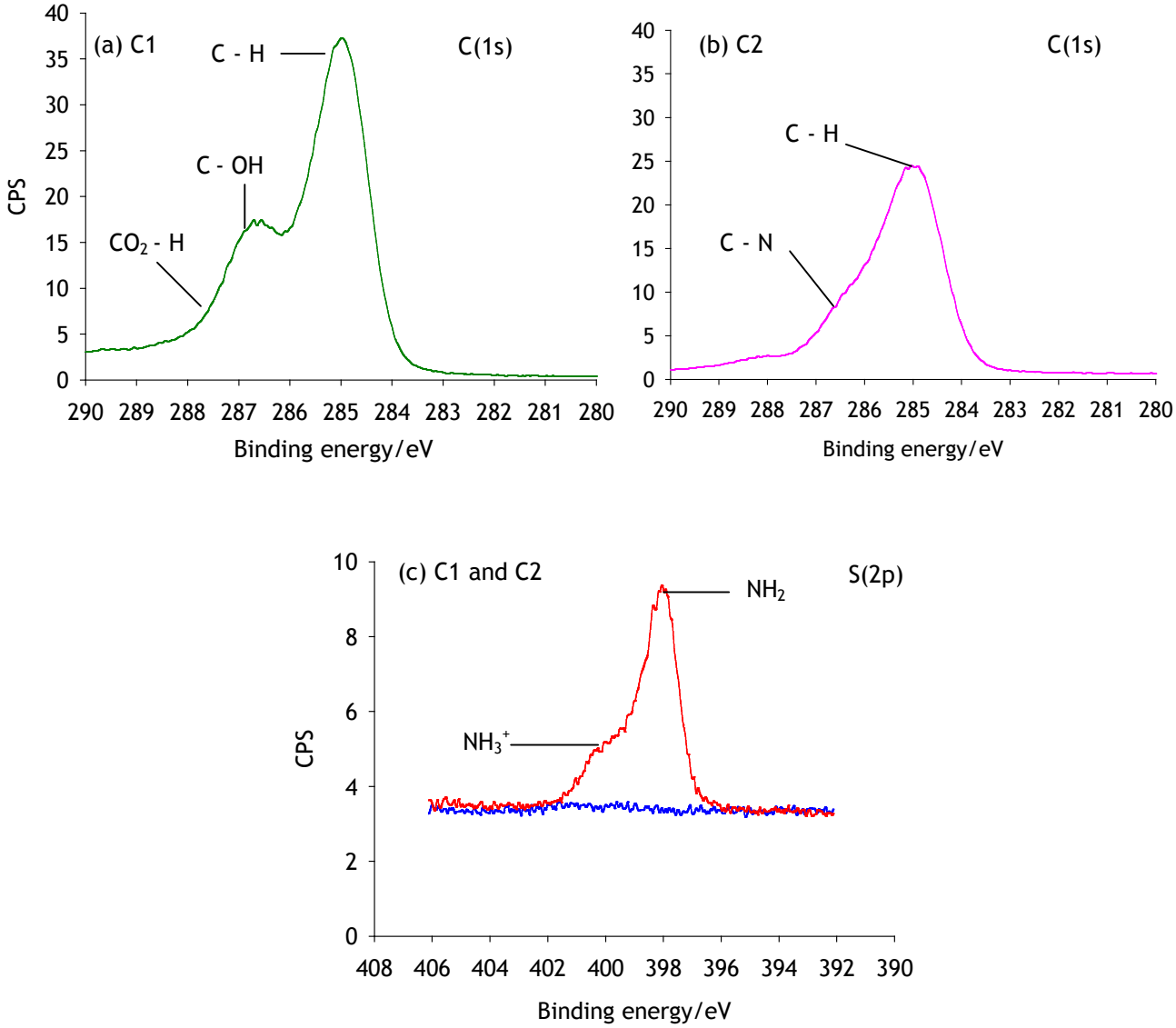

Figure 5.7: XPS spectra scanned at a specific region for the SU-8 sample treated with O_2 plasma and H_2SO_4 (C1) and O_2 plasma, H_2SO_4 and APTES 99% (C2). (a) Carbon C(1s) for sample C1 (green line), (b) Carbon C (1s) for sample C2 (magenta line), and (c) Nitrogen N (1s) region for both C1 (blue line) and C2 (red line) samples.

Meanwhile, **Figure 5.8** shows the XPS spectrum of carbon, nitrogen and sulphur regions after the NHS-biotin procedure (C4) and the complete sequence of biotin-streptavidin binding step. All of the elemental spectra were referred to the carbon C(1s) peak at 285 eV. From the comparison of the C(1s) spectra of Figure 5.7(b), 5.8(a) and 5.8(b), the appearance of the peaks at 288 eV and 286 eV for the surface treated with streptavidin-FITC (Figure 5.8(b)) show that a molecule containing an amide bond has been immobilised (i.e. a protein).

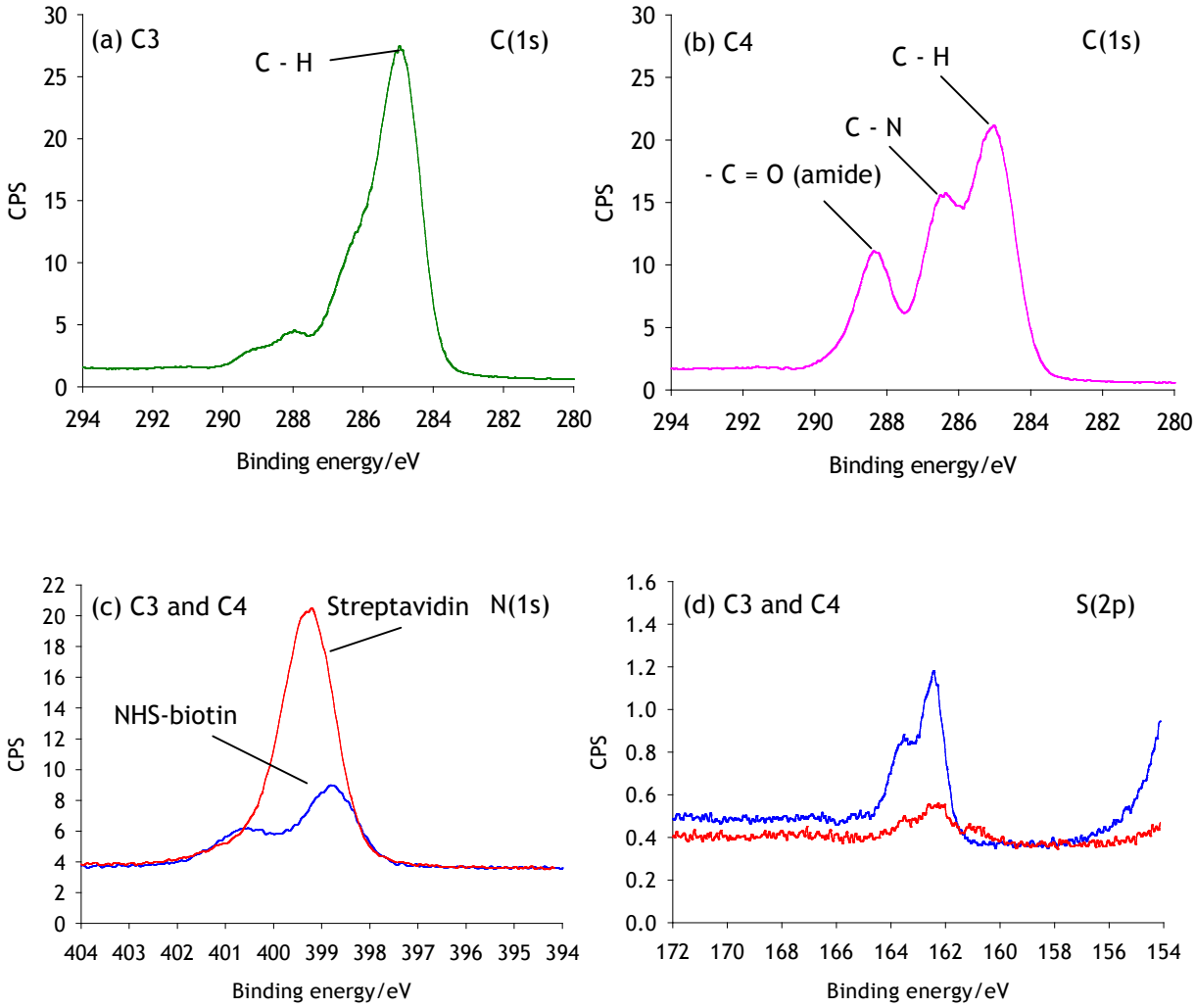

Figure 5.8: XPS spectra data collected from samples treated with O_2 plasma, H_2SO_4, APTES 99% and NHS-biotin (C3) and O_2 plasma, H_2SO_4, APTES 99%, NHS-biotin and streptavidin-FITC (C4). (a) Carbon C(1s) peak for C3 (green line); (b) Carbon C(1s) peak for C4 (magenta line); (c) Nitrogen N(1s) region for C3 (blue line) and C4 (red line); and finally (d) Sulphur S(2p) region for C3 (blue line) and C4 (red line) samples.

In addition, **Figure 5.8(c)** illustrates the N(1s) region for sample surfaces modified by NHS-biotin and streptavidin-FITC. Two features are seen in the spectrum of the NHS-biotin sample due to the presence of nitrogen in the amino silane and nitrogen in the biotin ring at 399-400 eV and promoted amine species at 400-401 eV. In contrast, for the streptavidin sample, the predominant N species found is that in an amide bond. Due to the large size of the protein, these are greater in number than those present in the NHS-biotin 'monolayer'. As part of the measurement set furthermore, the XPS spectrum was scanned through the sulphur S(2p) region in order to detect the S atoms in the biotin ring.

Figure 5.8(d) demonstrates that the sulphur S(2p) peak for the biotin sample, that can be clearly seen in the spectrum of sample C3 becomes masked following streptavidin immobilization, as in sample C4. The ratio of S to N in the NHS-biotin chemical structure was 1:3, and the ratio from the XPS measurement was approximately 0.8:3, showing that most of the aminosilane groups had become functionalised with NHS-biotin. Notably, the size of the S(2p) peak become smaller when protein is immobilised on the surface, as in sample C4, due to masking of biotin by the larger streptavidin protein molecule.

As a conclusion, the XPS results highlights that the carbonyl group (-COOH or -CONH) and N(1s) counts increase for samples subjected to the complete immobilization protocol. This represents the streptavidin-FITC binding at the end of the immobilization procedure. This XPS measurement peak results confirmed that the intermediate steps of aminosilanisation and biotin functionalization had proceeded as anticipated. This mean that the protocol for NHS-biotin conjugation with streptavidin-FITC were successful and consistent with the fluorescence images of **Figure 5.9.**

5.4 Immobilization in Microfluidic Channel

With the confidence gained from the surface assays described in Section 5.1 to 5.3, similar surface modification and immobilization protocols were employed in microfluidic channel experiments (discussed in **Chapter 6**). As final confirmation that these worked in the confined volume of a microfluidic device, the bonded PDMS microfluidic channel was removed from the sensor substrate and viewed under the microscope with an FITC filter set as shown in **Figure 5.9**. This indicated a significant quantity of streptavidin was immobilised in the channel by following the protocols outline above.

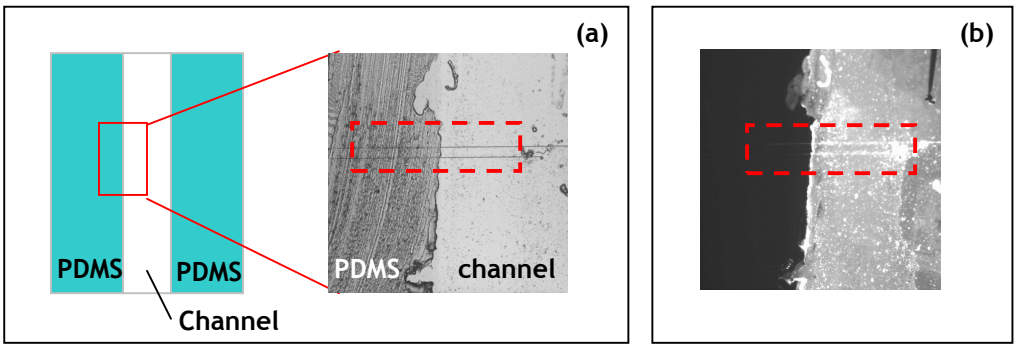

Figure 5.9: Diagram and images of FITC after the immobilization protocol is employed inside the microfluidic channel. (a) Microfluidic channel diagram (inset: SU-8 waveguide (red dashed line) and (b) Intensity counts between PDMS-channel boundaries.

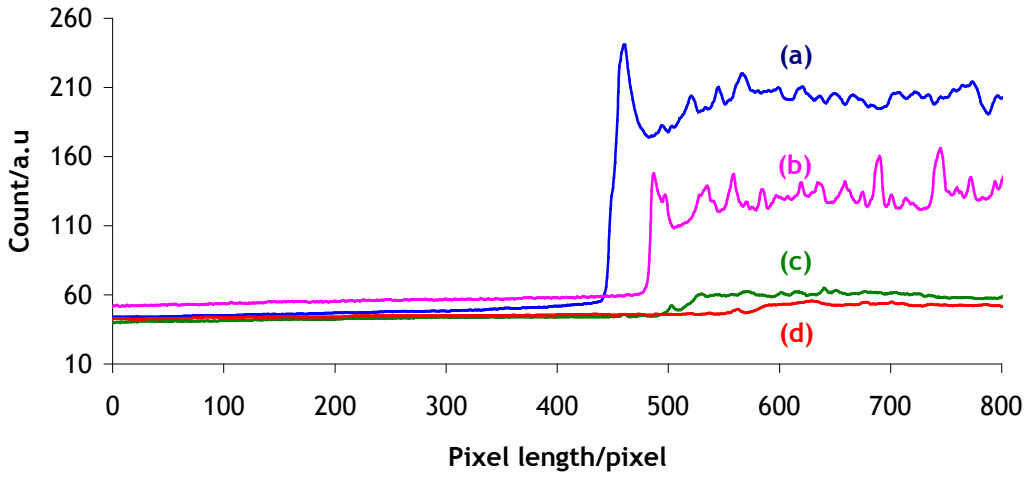

Figure 5.10: The fluorescence image shows the comparison of intensity counts across the sample after (1M) concentrated d-biotin solution was added to regenerate the sensing surface. (a) The original intensity counts as FITC (blue line), (b) after 10 min of incubation in an ultrasonic bath (magenta line), (c) after 3 hours incubation in the d-biotin solution (green line) and (e) after overnight d-biotin incubation (red line).

Finally, experiments were performed to discover whether the biotin-streptavidin bonding could be broken by soaking in a solution of concentrated d-biotin. As shown in **Figure 5.10**, line sections taken from fluorescence images indicate that a moderate reduction fluorescence intensity from (a) original state to (b), where the sample have been cleaned with IPA in an ultrasonic bath for 5 minutes; while in (c) where the solution has been soaked in a high concentration of d-biotin solution induced into the microfluidic channel and (d) after soaking in biotin solution overnight, there was almost complete loss of streptavidin signal.

5.5 Summary

In conclusion, experimental work using fluorescence conjugates and the XPS instrument has been used to determine the protein immobilization protocol on the SU-8 polymer surface. The data analysis from both methods have been discussed and confirmed that the SU-8 surface modification and protein immobilization protocols were successful. The detailed procedures for surface modification and protein immobilization are presented in **Appendix A.5.3**. This procedure was used in the specific protein binding experiments, described in the next chapter.

References

[1] G. Blagoi, S. Keller, A. Johansson, A. Boisen, and M. Dufva, "Functionalization of SU-8 photoresist surfaces with IgG proteins," Applied Surface Science, vol. 255, pp. 2896-2902, 2008.

[2] R. Marie, S. Schmid, A. Johansson, L. E. Ejsing, M. Nordstrom, D. Hafliger, C. B. V. Christensen, A. Boisen, and M. Dufva, "Immobilisation of DNA to polymerised SU-8 photoresist," Biosensors & Bioelectronics, vol. 21, pp. 1327-1332, 2006.

[3] M. Joshi, R. Pinto, V. R. Rao, and S. Mukherji, "Silanization and antibody immobilization on SU-8," Applied Surface Science, vol. 253, pp. 3127-3132, 2007.

[4] A. Deepu, V. V. R. Sai, and S. Mukherji, "Simple surface modification techniques for immobilization of biomolecules on SU-8," Journal of Materials Science-Materials in Medicine, vol. 20, pp. 25-28, 2009.

[5] M. Calleja, J. Tamayo, M. Nordstrom, and A. Boisen, "Low-noise polymeric nanomechanical biosensors," Applied Physics Letters, vol. 88, pp. -, 2006.

[6] L. N. Jiang, K. P. Gerhardt, B. Myer, Y. Zohar, and S. Pau, "Evanescent-Wave Spectroscopy Using an SU-8 Waveguide for Rapid Quantitative Detection of Biomolecules," Journal of Microelectromechanical Systems, vol. 17, pp. 1495-1500, 2008.

[7] S. L. Tao, K. C. Popat, J. J. Norman, and T. A. Desai, "Surface modification of SU-8 for enhanced biofunctionality and nonfouling properties," Langmuir, vol. 24, pp. 2631-2636, 2008.

[8] B. Y. Shew, Y. C. Cheng, and Y. H. Tsai, "Monolithic SU-8 micro-interferometer for biochemical detections," Sensors and Actuators a-Physical, vol. 141, pp. 299-306, 2008.

[9] J. M. Cooper, J. Shen, F. M. Young, P. Connolly, J. R. Barker, and G. Moores, "The Imaging of Streptavidin and Avidin Using Scanning-Tunneling-Microscopy," Journal of Materials Science-Materials in Electronics, vol. 5, pp. 106-110, 1994.

[10] Beamson, G.; Briggs, D. High resolution XPS of organic polymers. The Scienta ESCA300 database; John Wiley and Sons: Chichester, U.K., 1992

[11] A. Glidle, T. Yasukawa, C. S. Hadyoon, N. Anicet, T. Matsue, M. Nomura, and J. M. Cooper, "Analysis of protein adsorption and binding at biosensor polymer interfaces using X-ray photon spectroscopy and scanning electrochemical microscopy," Analytical Chemistry, vol. 75, pp. 2559-2570, 2003.

[12] C. Kim, D. Jeong, J. Hwang, H. Chae, and C. K. Kim, "Argon and Nitrogen Plasma Surface Treatments of Polyimide Films for Electroless Copper Plating," Journal of the Korean Physical Society, vol. 54, pp. 621-627, 2009.

[13] M. Dhayal and D. A. Ratner, "XPS and SPR Analysis of Glycoarray Surface Density," Langmuir, vol. 25, pp. 2181-2187, 2009.

[14] B. Thierry, M. Jasieniak, L. C. P. M. de Smet, K. Vasilev, and H. J. Griesser, "Reactive epoxy-functionalized thin films by a pulsed plasma polymerization process," Langmuir, vol. 24, pp. 10187-10195, 2008.

[15] Sigma-Aldrich Corp, USA [Online] http://www.sigmaaldrich.com/

[16] MicroChem Corp, USA [Online] http://www.microchem.com/

[17] Zeiss AG, Germany [Online] Available: http://www.zeiss.com/micro

[18] Andor Technology Plc [Online]. Available : http://www.andor.com/

[19] Casa Software Ltd, UK [Online] Available: http://www.casaxps.com/

CHAPTER 6

Applying Micro-resonator for Optical Biosensing

Introduction

As demonstrated in the previous chapter, spectra were obtained from various gapless ring and disk resonator configuration for specific ring and disk radii. Importantly, the resonances in these spectra remained observable when water was placed on the sensor surface. Since the sensor surface was to be used inside a microfluidic channel, this latter investigation was crucial before further sensing experiments were designed.

As has been noted, the FSR obtained from calculations and experimental results for a 'single' disk structure was 1.3 nm (see **Section 4.3.1**, **Chapter 4**). It was discussed that this small FSR value coupled to the uniformity of the resonances pattern leads to complexity in detection and measurement, especially when the magnitude of the resonance shift is similar to the FSR value, or greater. For such shifts, the 'new' resonance wavelength peak would be undistinguishable from a smaller shift of the neighbouring peak resonance. However, this dilemma was successfully overcome by fabricating the double-cascaded gapless disk resonator with a resulting wider composite FSR value within the visible wavelength region.

In this chapter, the potential characteristics of DDR are investigated as a potential optical refractive index biosensor. The two principal experiments are conducted using a microfluidic channel arrangement in order to measure the resonance wavelength shift due to the changes of surrounding media refractive index. The first experiment involved the detection of changes in the bulk refractive index of a series of sugar solutions. Making solutions of defined sucrose concentration in water is a well-established means of making solutions with known refractive indices [see **Appendix A.6.1**]. The second experiment was specific to protein detection and based on the change in effective refractive index that occurs when material is absorbed on to the resonator surface[1][2]. The specific biotin-streptavidin SU-8 functionalisation was as described and antibody-antigen systems utilised in the previous chapter, so as to provide an analogy with protocols used in conventional immunoassays.

6.1 Calibrating Shifts Resonance Using Solutions of Different in Refractive Index.

6.1.1 Introduction

As the optical resonator operates in an aqueous solution, the output signal is affected by analytes or other properties of the aqueous media that acts as an upper cladding of the waveguide. This solution modifies the surrounding refractive index and so alters the effective index of the cladding that defines the waveguide guiding mode. This results in the resonance wavelength peaks being shifted by an amount that depends on the refractive index change[1-4][7-10]. An easy way to vary the refractive index of the bulk solution is to make large changes of the concentration of an analyte.

6.1.2 Materials and Methods

As indicated, a simple way to demonstrate the bulk detection and resonance wavelength shift of the resonators device was by using various concentration of sucrose solution (Sigma, S-7903). In this section, sucrose solutions of different refractive indices have been prepared and utilised in order to perform the sensing calibration. A selected resonance wavelength peak was monitored using the LabSpec software (Horiba Ltd, Japan) and the resonance shifts were recorded. DI water was used to give an initial reference reading of the resonance wavelength.

The experimental setup of **Figure 4.5** was utilised in this experiment. Two pumps were used to mix a concentrated sucrose solution and DI water in a mixing chamber before passing over the resonator. The flow rates of both pumps were varied (see **Table 6.1**) and the solutions from the exit of the microfluidic channel were collected in Eppendorf® [Eppendorf AG, Germany] tubes. This allowed measurement of the refractive index of collected portion of the

mixed solution to be made off-line using an Abbe refractometer instrument [Bellingham and Stanley Ltd, UK]. Correlations could then be made between the refractive index value of sucrose solutions and the measured resonance wavelength shift.

6.1.3 Evaluating The Stability of Optical Output in Aqueous Solution

As a preliminary step, the DI water was injected into the microfluidic channel. The flow rate was set to increase from 0.05 ml/min to 0.50 ml/min for t = 4000 s during the course of a experiment. This water flow test was conducted in order to investigate the stability of the resonance wavelength pattern during the continuous water flow. It was very important to make sure that the resonance shift displacement was not influenced by immersion time in water or the flow rate. These results are shown in **Figure 6.1**.

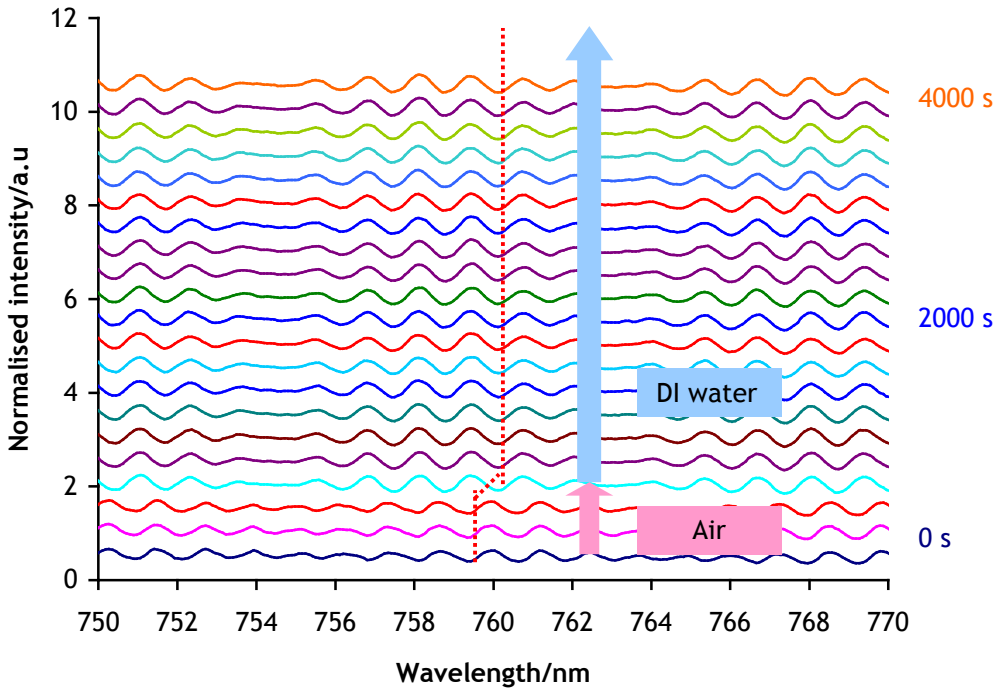

Figure 6.1: The plotted graph illustrated the normalised intensity/a.u of resonance wavelength patterns at different time/s during the continuous water flow experiment. The line was vertically displaced for clarity. Each colour is a recording sequential at t = 200 s intervals. The actual recording data was at every t = 3 s respectively. Resonance shift monitoring is shown by the red dashed line.

Figure 6.1 shows the spectra collected from the double-cascaded gapless disk resonator at t = 200 s intervals as the DI water solution flowed continuously inside the microfluidic channel. This graph shows that there is a larger resonance shift from ~ 0.7 nm between t = 400 s and t = 600 s. During this interval there is a refractive index difference change from 1.00 (air) to

1.33 (water). From t = 600 s onward, it is clearly seen that there was no further shift in the resonance peak patterns. By focusing on one resonance wavelength, that at λ = 759.421 nm, the change in output intensity can also be monitored, in **Figure 6.2**. According to the result, there was no resonance wavelength shift or wavelength drift due to water continuously flowing inside the microfluidic channel. This indicated that the sensor device was suitable to investigate optical response in flowing analyte media in further experiment.

As displayed in **Figure 6.2**, when DI water was injected into the dry device at t = 500 s the intensity counts sharply increase from 5000 to 6500 counts (see **Figure 4.10, Chapter 4**). The intensity counts and pattern then remained stable until t = 4000 s as the flow rate was gradually increased to 1.00 ml/min. Notably, although there is a slight decrease in intensity after t = 500 s, close inspection of the spectra showed there was no discernable shift in the resonance feature.

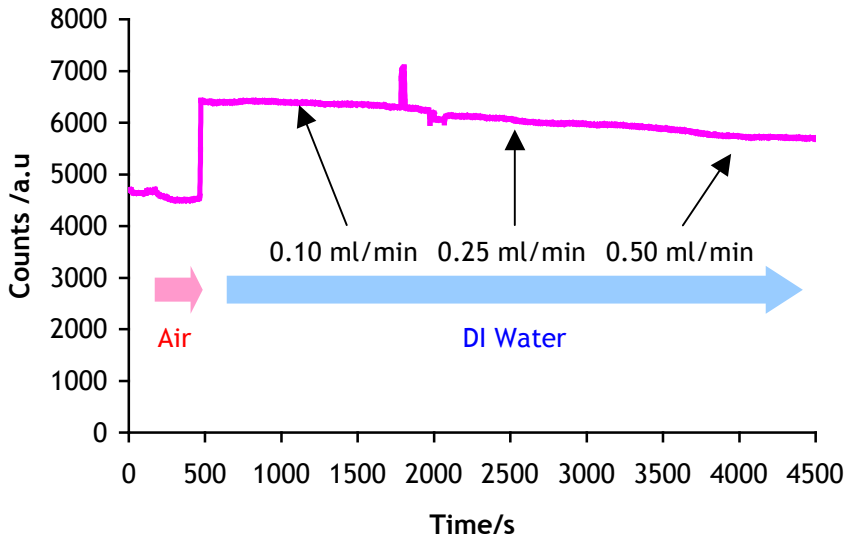

Figure 6.2: The intensity of resonance wavelength counts/a.u at the particular resonance wavelength peak of λ = 759.421 nm according to the time/s at the continuous flow of water experiment inside the microfluidic channel.

From the observation, the intensity count gradually decreased by approximately 10% from the DI water was introduced at t = 500 s until t = 4500 s. It was assumed that with the increasing temperature, the density of the DI water was slightly decreasing and the refractive index of the DI water was also altered. As a result, the light propagation speed was also changed as was the influenced the intensity count.

6.1.4 Evaluating Changes in Optical Output for Continuously Varying Changes in Solution Refractive Index.

As discussed before, sucrose was utilised in order to make solutions of different refractive indices. Two pumps were utilised in this experiment, where the first pump held a syringe contained a concentrated sucrose solution while the second pump held a DI water syringe. Refractive indices of the solutions were measured using an Abbe refractometer prior to the conducted experiment.

Table 6.1 lists the flow rates (ml/min) for each pump and the calculated mixed sucrose concentration. These were collected into a series of 11 Eppendorf® tubes. In addition, the experimental times for each set of flow rate conditions were recorded as in Table 6.2, in order to correlate the resonance wavelength response with the solution composition. Notably, the mixed sucrose solution was allocated to allow passes over the resonator at a sufficient time for the output response to reach a steady state, before altering the flow rates to set the next sucrose concentration in the series.

Table 6.1: Different continuous flow rate arrangements to be set at pumps variable for two sets of sucrose tests.

Pump 1 flow rate, ml/min (Sucrose)	Pump 2 flow rate, ml/min (DI Water)	Mixed concentration (50% sucrose)	Eppendorf tube no.
0	0.1	**0**	1
0.01	0.09	**5**	2
0.02	0.08	**10**	3
0.03	0.07	**15**	4
0.04	0.06	**20**	5
0.05	0.05	**25**	6
0.06	0.04	**30**	7
0.07	0.03	**35**	8
0.08	0.02	**40**	9
0.09	0.01	**45**	10
0.1	0	**50**	11

Table 6.2: Recorded time for both sets of experiment.

Mixed concentration (50% sucrose)	Start (s)	Finish (s)	Eppendorf tube no.
0	0	360	1
5	380	740	2
10	770	1130	3
15	1150	1510	4
20	1590	1850	5
25	1984	2334	6
30	2360	2720	7
35	2745	3105	8
40	3135	3495	9
45	3530	3890	10
50	4050	4424	11

Figure 6.3 shows extracts from the raw data set that contained spectra recorded every 3s for approximately t = 4000s. The presented spectra correspond to those collected half way through the time interval corresponding to a particular sample.

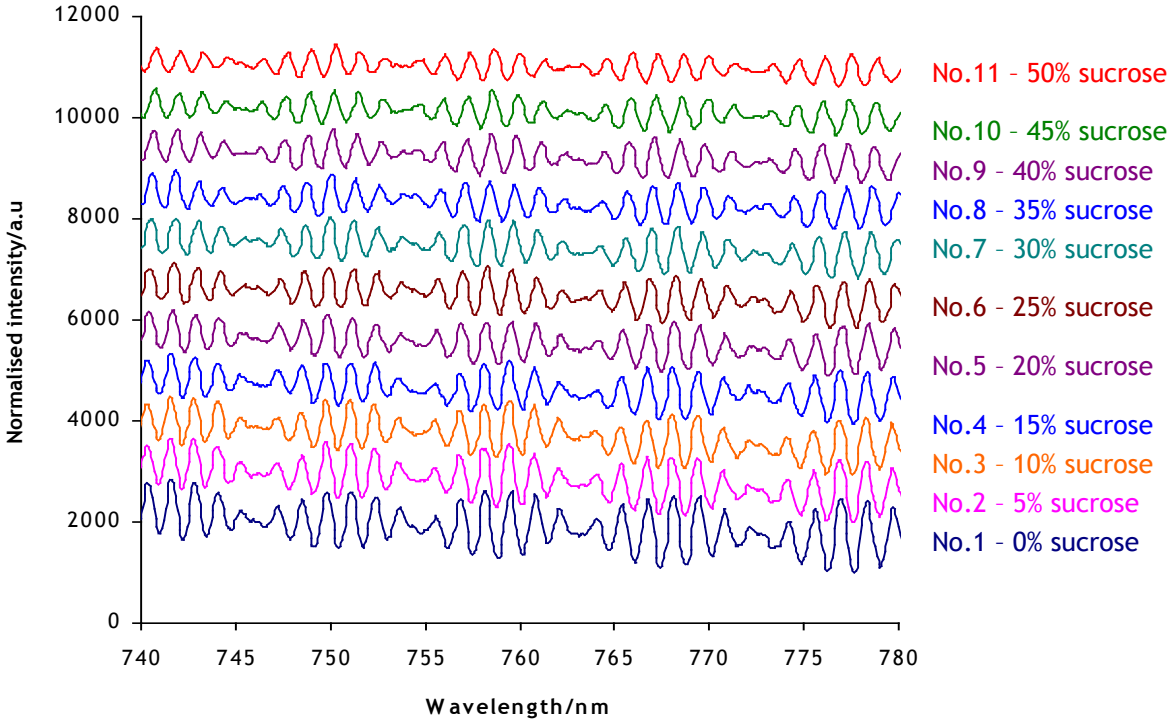

Figure 6.3: The normalised intensity/a.u of resonance wavelength response due to the duration of the experiment for Sucrose 50% solution. Each coloured line represents the resonance pattern that was recorded according to the Eppendorf® tube number in Table 6.2. The plotted lines were vertically displaced for clarity.

Figure 6.4 shows a subset of the spectra in **Figure 6.3**, where the x-axis has been expanded to make it easier to see the shift in resonance peak. Since the base solution for this experiment was the DI water, the initial resonance response at t = 0 s was recorded when the sensor area was filled with the DI water. A reference resonance peak was measured at λ = 758.220 nm. The concentrations of the mixed sucrose solution corresponding to these measurements were derived from **Table 6.2.**

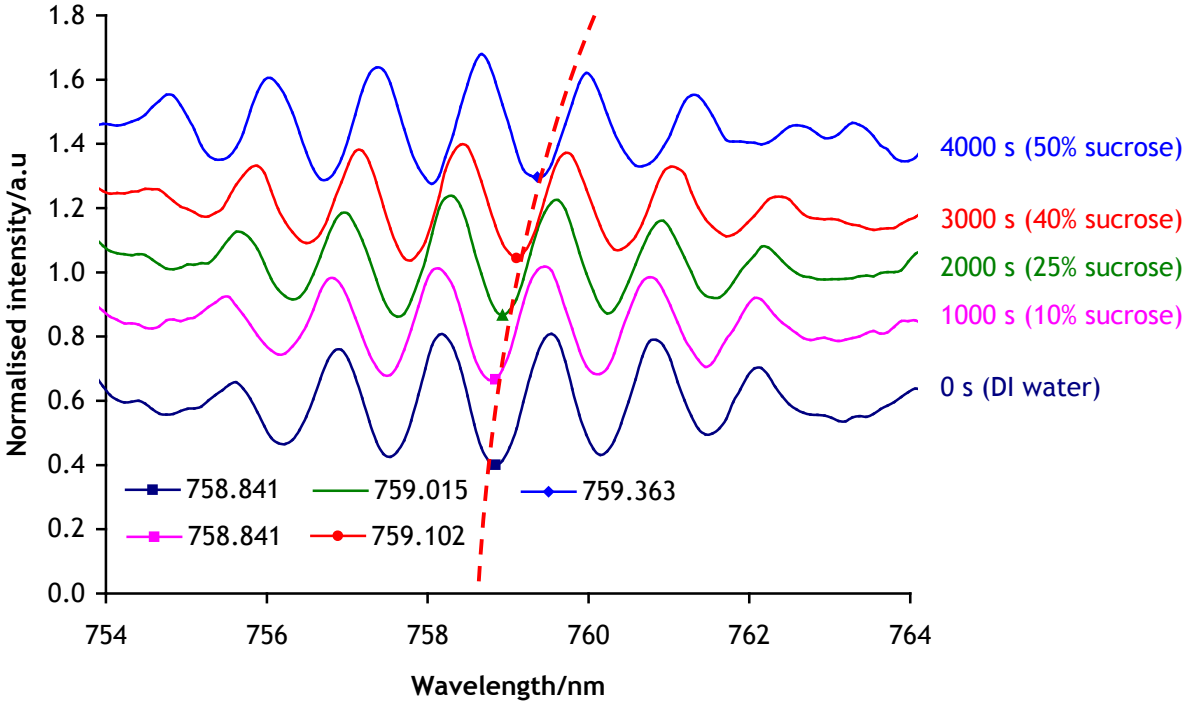

Figure 6.4: Normalised intensity of resonance wavelength pattern at different time stage of experiment. The wavelength region was projected between λ = 754 – 764 nm and the plotted lines were vertically displaced for the ease of comparison. The (red dashed) shows the tracked of resonance peak position upon the time duration.

By monitoring the chosen peak in **Figure 6.4**, it was clearly seen that the resonance was displaced from the value in DI water of λ = 758.841 nm to a higher wavelength of λ = 759.363 nm when in a 50% sucrose solution.

At the same time as collecting spectra as indicated earlier, the mixed solutions from the microfluidic channel outlet were collected in the Eppendorf® tubes and the refractive index of these solutions were measured by using Abbe refractometer [see **Appendix A.6.2**]. These refractive index measurements are shown in **Figure 6.5**. The shift in resonance is gradual, with increasing sucrose concentration, as shown in **Figure 6.6**.

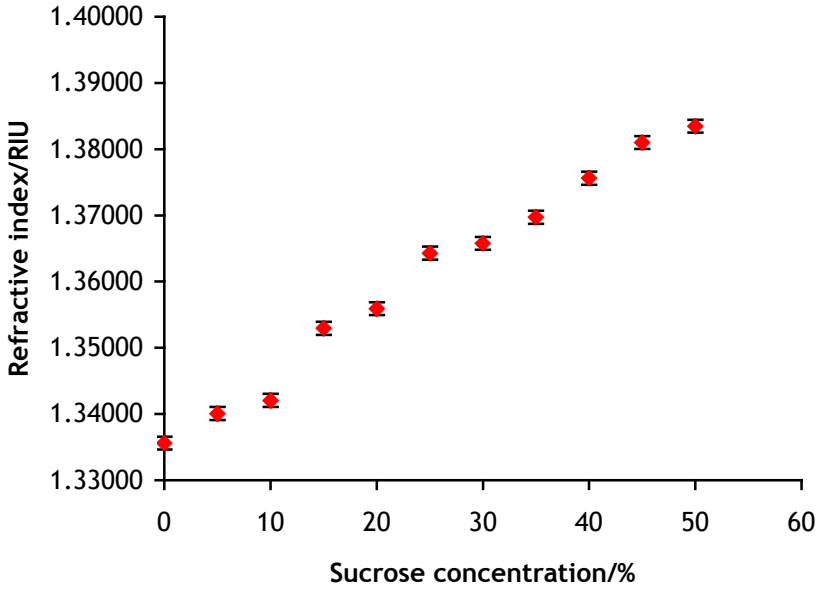

Figure 6.5: The refractive index value of the collected solution from an Eppendorf® tube upon the sucrose concentration/% at continuous sucrose flow experiment for 50% sucrose concentration. The error bar for refractive index unit was obtained from Abbe refractometer manual at ± 0.00098.

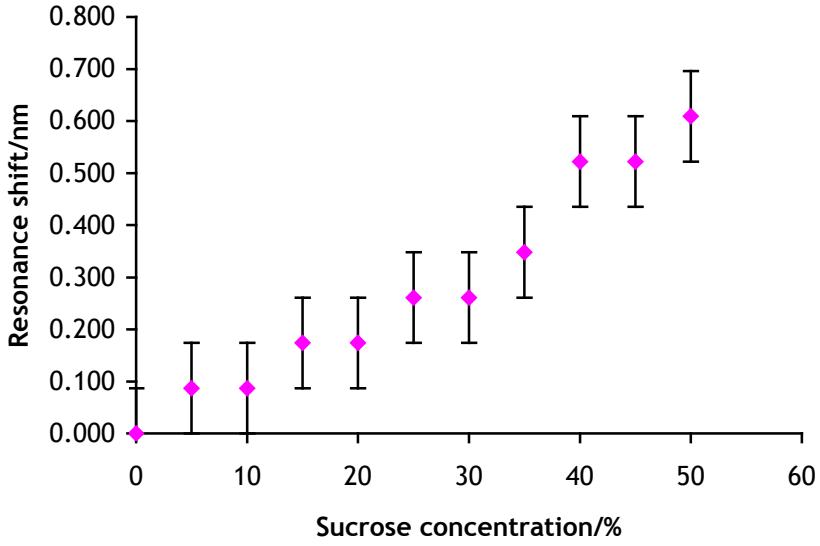

Figure 6.6: Resonance shift/nm response against the sucrose concentration (%) solution, for 50% sucrose solution. The error bar for resonance shift was obtained from of spectrum analyser system and was assumed to be at ± 0.087 nm, see page 74.

From the plotted data, the graphs in **Figure 6.5** and **Figure 6.6** show that under continuous flow conditions, both refractive index and resonance shift are well correlated with sucrose concentrations. Using data in **Figure 6.3** (and a similar graph for an 80% sucrose experiment) the refractive index changes and resonance wavelength shifts were tabulated [see **Appendix A.6.3**]. Thus, as shown in **Figure 6.7**, the resonance wavelength shift demonstrated a linear relationship with sucrose concentration solution for experiments involving either 50% or 80% stock sucrose solutions (i.e. disk radius is 40 μm). In the plot of **Figure 6.7(a)**, for the 50% sucrose experiment, the linear correlation between refractive index and resonance shift is 11.6 nm/RIU. This was a similar value to that obtained when these experiments were repeated using a stock of 80% sucrose solution, as shown in **Figure 6.7(b),** where the linear variation in resonance shift with refractive index was 11.9 nm/RIU.

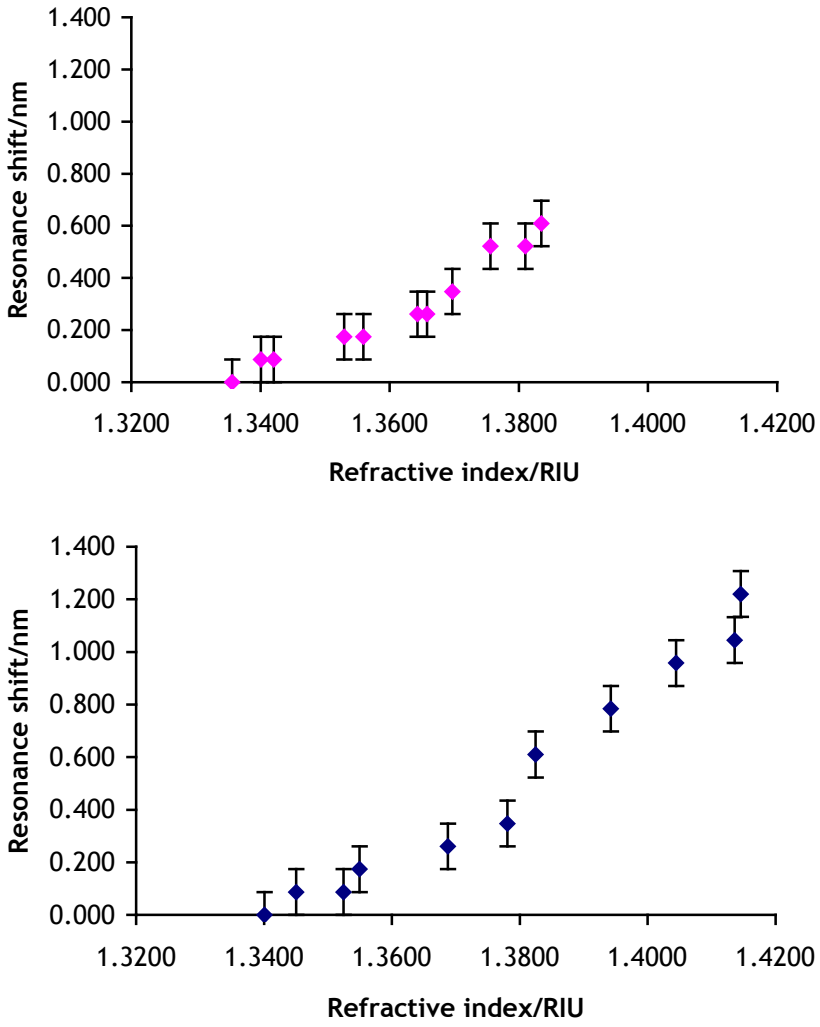

Figure 6.7: Resonance wavelength shift upon measured refractive index changes of sucrose concentration during continuous flow experiment. (a) 50% sucrose and (b) 80% sucrose. The error bar for resonance shift was obtained from of spectrum analyser system at ± 0.087 nm.

In summary, these experiments showed that, when the sucrose solution concentration increases, the refractive index will also increase. From the data analysis, it was demonstrated that there was a close to linear relationship between the resonance wavelength shift and refractive index changes for both mixed sucrose solution. This result was important for solution calibration and refractive index detection of the unknown species.

6.1.5 System Response Time

In order to verify the ability of the sensor device and microfluidic system to respond rapidly due to the changes of refractive index, a solution flowing over the sensor was switched from DI water to 30% sucrose using an in-line valve. As shown in **Figure 6.8**, the output response was rapid on the timescale of the overall measurement.

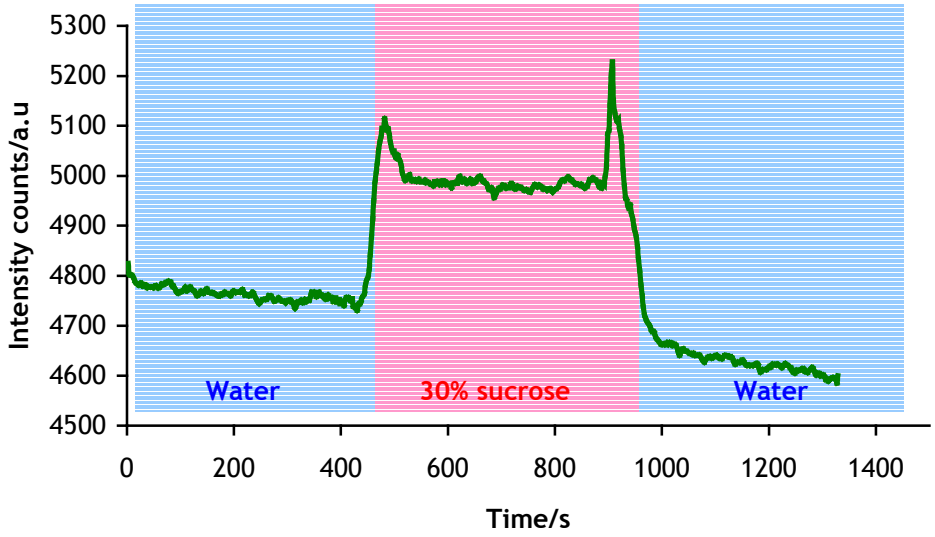

Figure 6.8: Intensity counts/a.u (green line) of specific point (resonance wavelength at λ = 757.01 nm) according to the experiment time/s duration for 30% sucrose concentration.

As illustrated in **Figure 6.8**, the intensity count of specific resonance wavelength λ = 757.01 nm was recorded for a period of the time to determine the response. When the sucrose solution was introduced at t = 480 s, the output count was increased until it was stabilised at ~ 5000 counts. When the sucrose solution reached the equilibrium state in the microfluidic channel, the recorded intensity count was stabilised. It can be seen that the intensity count level was gradually decreasing from 4800 to 4600 counts with time. The possible explanation would be local temperature changes or that the sucrose density was decreased. As a result, the refractive index of the sucrose was also slightly decreased.

It is thought that the optical response is instantaneous, but measurements to decouple the sensor response time from the microfluidic delivery system response time would require

making a network of microfluidic channels above the sensing area so that changes in solution could be made closer to the sensing element. It was also observed that twos peaks were occurred between the region of water and sucrose solution, to be specific when the switching valve is used at t = 500 s and t = 950 s. The possible reason for both peaks was caused by different pressure that affect the sensing structure during valve switching step. Nevertheless the measured time response gives a indication of the minimum length of time required for the system to reach equilibrium following each step in the protein assay described in later section.

6.1.6 Use of Calibration Curve

To evaluate the ability of the calibration curves in **Figure 6.7**, to assay individual sucrose solutions, three known and two unknown sucrose solutions were made up. These were then flowed over the sensor and the shifts in resonance recorded, as in **Table 6.3**. During these experiments, solutions from the output channel of microfluidic were collected by using Eppendorf ® tubes for further analysis using an Abbe refractometer. These data together with the calibration curve are then plotted on the same graph, as in **Figure 6.9**.

Table 6.3: Resonance wavelength shift (nm) and refractive index measurement of individual sucrose solution and unknown samples.

Sucrose (%)	Resonance Shift (nm)	Ref Index measured by Abbe refractometer
10	0.174	1.34602
20	0.261	1.36183
30	0.436	1.37954
Unknown 1	0.087	1.33809
Unknown 2	0.610	1.40683

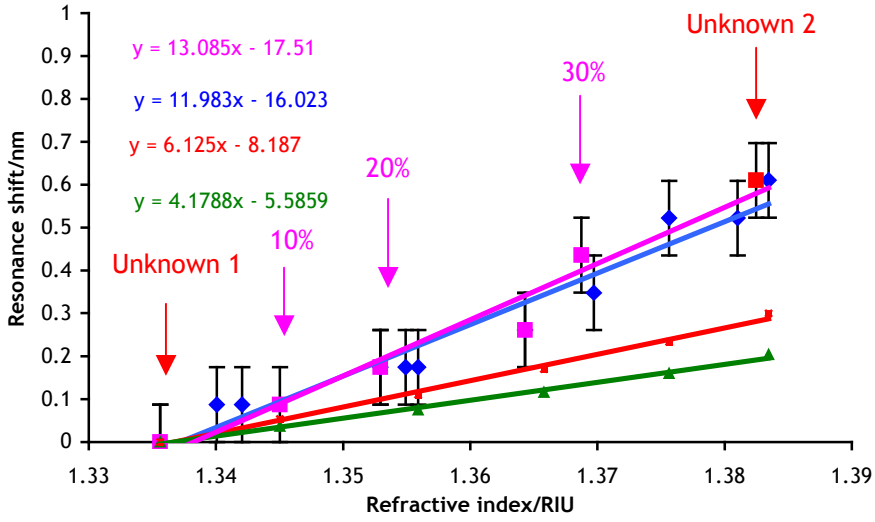

Figure 6.9: Resonance wavelength shift response upon the sucrose concentration for continuous flow mixing (blue points), individual sucrose concentration (magenta points) and unknown sucrose concentration (red points) from the experiments. The calculation calibration curves were shown as TM polarization (red line) and TE polarization (green line). It is probable that these early simulation results do not yet predict the experimental data.

From this, it appears that the resonance shifts for the pre-made 10, 20 and 30% solutions make an over estimate of the sucrose concentration of the unknown species. The errors are likely to be due to the solutions in each Eppendorf® sample being the accumulation of a solution of variable concentration that had passed over the resonator surface in a particular time interval during the continuous flow calibration experiments.

A second technique that can be used to assay the sucrose solution is to compare the whole resonance pattern of the unknown solution with the various resonance patterns collected during the continuous flow experiment. When the resonance in a spectrum from this latter set coincides with those of the unknown sucrose spectrum, the spectrum will correspond to the 'correct' sucrose concentration in the continuous flow data set. This procedure would lead to better precision in the determination of resonance shifts.

In conclusion, it was demonstrated that the fabricated SU-8 double-cascaded disk resonator could be used to measure the refractive index of a sucrose solution (bulk detection). When the refractive index of the surrounding solution changes (because of sucrose solution), the resonance wavelength also changed by ~ 12 nm/RIU. Several experiments were conducted in order to investigate the relationship between sucrose solution concentrations, the refractive index change and the resonance wavelength shift. From the presented results, a linear relationship was obtained between the resonance wavelength shifts and the sucrose refractive index value. The sensitivity is low compared to that of a Mach-Zehnder system. However, the use

of a vernier cascaded disk configuration has the potential to facilitate the measurement of small changes with greater precision, especially if a configuration was used in which only one of the disks was exposed to the analyte.

6.2 Surface specific detection

6.2.1 Introduction

A second mechanism of sensing using resonator devices uses refractive index changes caused by absorption on the SU-8 polymer surface. In order to do this, modification of the sensing surface needs to be performed in order to construct a binding site for specific species [9]. This method, if successful, would lead to label-free detection since the evanescence field that penetrates the SU8 polymer boundary can be utilised as a probe to sense analytes adsorbed during a binding event.

As a preliminary investigation, a system based on biotin-(strept)avidin binding was chosen for specific detection since it is one of the most common methods used for noncovalent conjugation. In this thesis a variant of avidin, streptavidin[2][3][7][11] was used for specific binding detection experiments. Streptavidin is a protein that has been produced and extracted from the bacteria of Streptomyces *avidinii*, and thus the primary structure is considerably different to the avidin (a glycoprotein found in egg white[5]). Use of the streptavidin molecule is advantageous compared to avidin because it has lower non-specific binding interactions with the other proteins and molecules often found on substrate surfaces. However, both avidin and streptavidin molecules show similar binding strength towards biotin. The dissociated constant of the streptavidin (K_d) is approximately 1.3 x 10^{-15}M and due to its tetrameric structure, it can bind up to four biotin species. Streptavidin is also resistant to denaturation under extreme conditions. It was reported that 6-8 M guanidine at pH of 1.5 is needed to encourage the dissociation between biotin-streptavidin binding[6][12].

6.2.2 Material and Methods

Again, the setup shown in **Figure 4.4** and **Figure 4.9**, was used for the protein immobilization experiments. SU-8 polymer sensing areas inside the microfluidic channel were functionalised with NHS-biotin B3295 (Sigma-Aldrich, USA) using the protocol in **Chapter 3**. The materials and chemicals utilised in the experiments were a Streptavidin *avidinii* SA-5000 (Vector Laboratories Inc, USA), Biotinylated anti-Mouse IgG BA-2000 (Vector Laboratories Inc, USA), Mouse IgG I-5381 (Sigma-Aldrich, USA), d-biotin B-4501 (Sigma-Aldrich, USA), Dulbecco's Phosphate Buffer Saline (PBS) D8537 (Sigma-Aldrich, USA) and DI water.

Generally, each experiment in this section was conducted a minimum of two times in order to probe the reproducibility of the sensing events. The total duration of the experiment was approximately 15 min in order to give enough time for injected solutions to reach

equilibrium and be used out at each stage. In order to avoid the detection of non-specific adsorption and free molecules in the solution, the channel was rinsed with PBS to remove the unwanted molecules species and residue after each step in the protocol as in **Figure 6.10**.

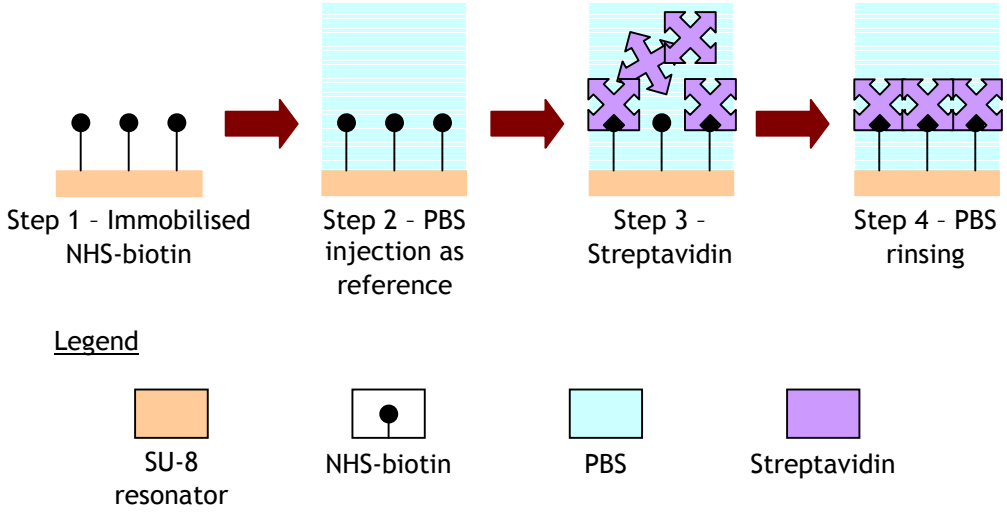

Figure 6.10: The sequences of step in specific protein experiment. Duration (s) for each step is recorded and optical output is monitored in real time during the experiments.

6.2.3 Biotin-streptavidin Interaction

The NHS-biotin was immobilised onto the device (as described in **Appendix A.5.3**) and prepared streptavidin solution was introduced into the microfluidic channel. The resonance wavelength spectrum was recorded and analysed as shown in **Figure 6.11.**

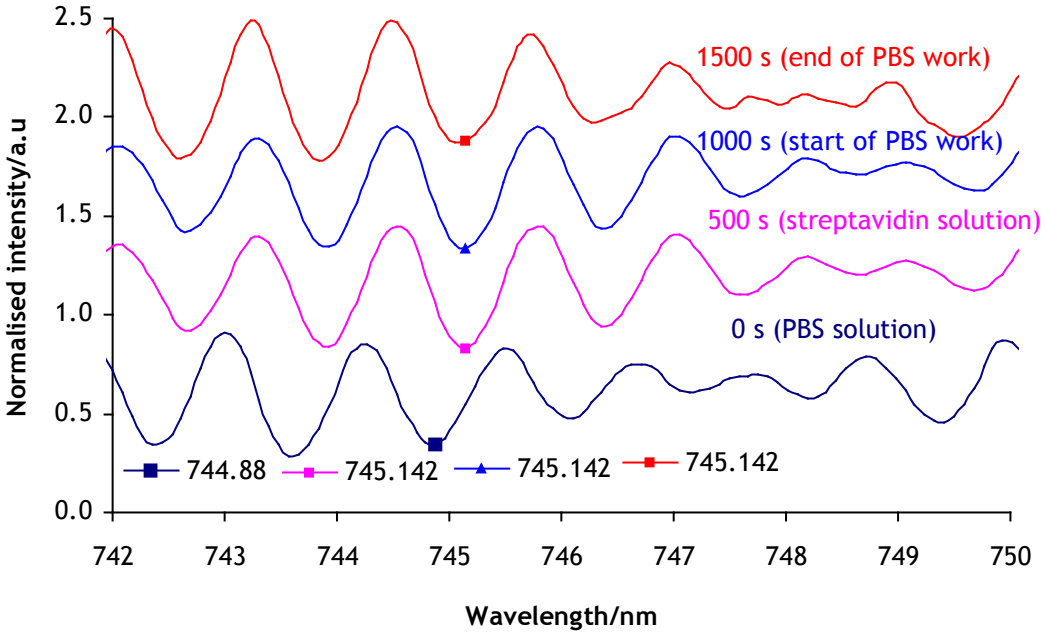

Figure 6.11: The optical response of double-cascaded disk resonator sensor due to the different steps of applied solution. Resonance wavelength peak was chosen and monitored during the experiment. (0 s – PBS solution, 500 s – streptavidin, 1000 s – PBS solution after streptavidin-biotin and 1500 s – PBS solution reach equilibrium). Each collected response was vertically displaced for clarity.

Figure 6.11 demonstrates the resonance wavelength pattern from the DDR device when various prepared solutions were passed over the sensing area. The normalised intensity was vertically displaced for the ease of comparison during peak monitoring and resonance shift recognition. Firstly, the PBS solution (Step 2) was introduced to the biotin functionalised sensor (in Step 1) device to give a base line reading. Then, in Step 3, the prepared streptavidin solution (0.030 mg/ml) was introduced into the sensing area through the microfluidic channel, and the output spectra were recorded. Finally, the PBS solution was injected to rinse the non-specific bound and free-floating streptavidin as shown in (Step 4).

From the collected data, it was observed that the resonance response was steady during the first stage that involved flowing of PBS solution. For reference, a resonance feature at λ = 744.880 nm was chosen. According to the analysed data between t = 250 - 700 s, this feature shifted at its position stabilised at t = 500 s. Thus, t = 500 s was selected as the representative of streptavidin binding solution. Here, the resonance wavelength had at λ = 745.142 nm. This was a 0.262 nm shift from the initial state. The channel was then rinsed with PBS for t = 1000 s, to remove the streptavidin solution and any non-specifically adsorbed streptavidin. After rinsing, the resonance wavelength shift was still approximately 0.262 nm. This indicated that the

streptavidin molecules were still bound on the sensor surface, probably forming a monolayer of streptavidin.

In order to validate that the device sensor was not detecting non-specific adsorption or free floating streptavidin molecules, another experiment was conducted using a device that did not have NHS-biotin immobilised on the surface. Similar experimental procedures were employed and the collected data were analysed as shown in **Figure 6.12.**

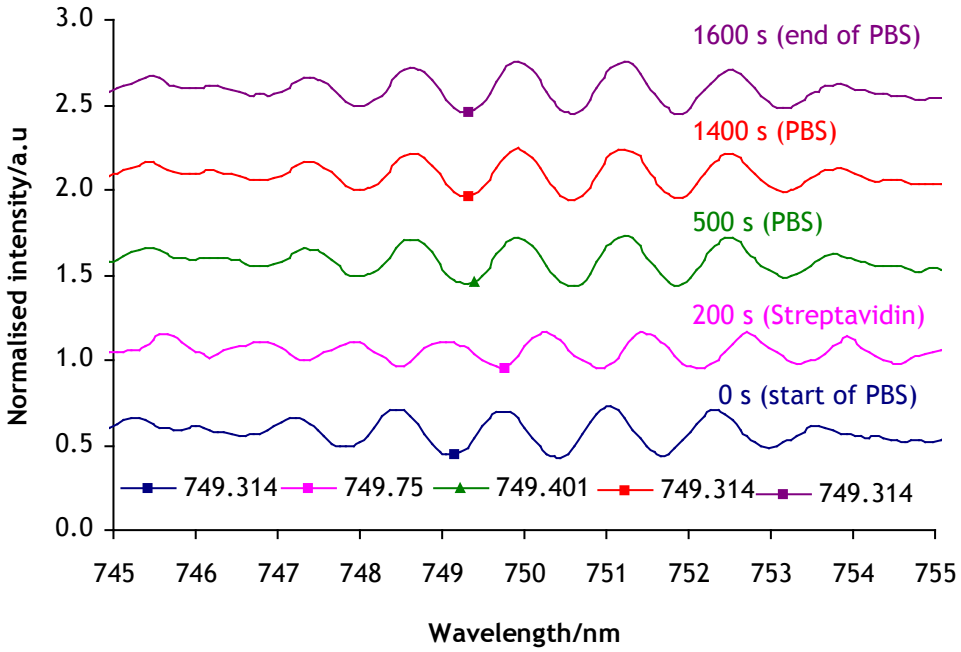

Figure 6.12: The resonance wavelength spectra upon the different steps of employed solution. The initial (PBS) step was represented by t = 0 s. The second step consists of streptavidin solution at t = 200 s. It was followed by PBS solution at 500, 1400 and 1600 s to rinse the streptavidin solution until it was totally flushed.

Here, the chosen resonance wavelength peak of λ = 749.314 nm in PBS solution was used as a reference. The streptavidin solution was flowed into the microfluidic channel and it was observed that the resonance wavelength pattern gradually changed the position and until finally it became stable at t = 300 s. Then, the channel was rinsed with PBS for t = 1000 s.

From **Figure 6.12**, it was demonstrated that the resonance peak at λ = 749.314 nm, moved to λ = 749.401 nm when streptavidin solution was applied onto the sensing area. However, when the PBS solution was introduced again to flush the free floating streptavidin and non-adsorption molecules, it can be clearly seen that the monitored resonance wavelength shifted back to λ = 749.314 nm. This phenomenon indicated that there was no permanent binding interaction between streptavidin and the sensor surface (which in this case had not been functionalised with the NHS-biotin molecules).

These experiments confirmed that the biotin-streptavidin binding activity occurred and could be detected by monitoring the resonance wavelength shift occurred (0.261 nm). Importantly, there was no permanent resonance wavelength shift when streptavidin solution was introduced into and then rinsed off the sensing area that did not have NHS-biotin immobilised on it. This experiment indicated that the sensor showed the capability to detect protein molecules without any fluorescence labelling on the targeted protein. Both experiments were repeated with the same sensing device. Between experiments, the device was regenerated by injection of the higher concentrated d-biotin solution into the microfluidic channel to displace any streptavidin molecules.

6.2.4 Detection of Sequential Binding Events in A Stepwise Assay

In the first configuration of a biotin-streptavidin detection system, the streptavidin molecules were used as a bridge to bind biotinylated proteins to a biotinylated surface by making use of the multiple (four) binding sites on streptavidin. In this Section, streptavidin molecules used to link the NHS-biotin that has already immobilised on the SU-8 polymer surface with a biotinylated antibody BA-2000 (Vector Laboratories, USA) that is injected into the microfluidic channel. A series of steps as illustrated in **Figure 6.13** is used to build up a multi layer surface for use in an immunoassay detection system. The full assay system consisted of NHS-Biotin, streptavidin, biotinylated anti mouse IgG, and mouse IgG.

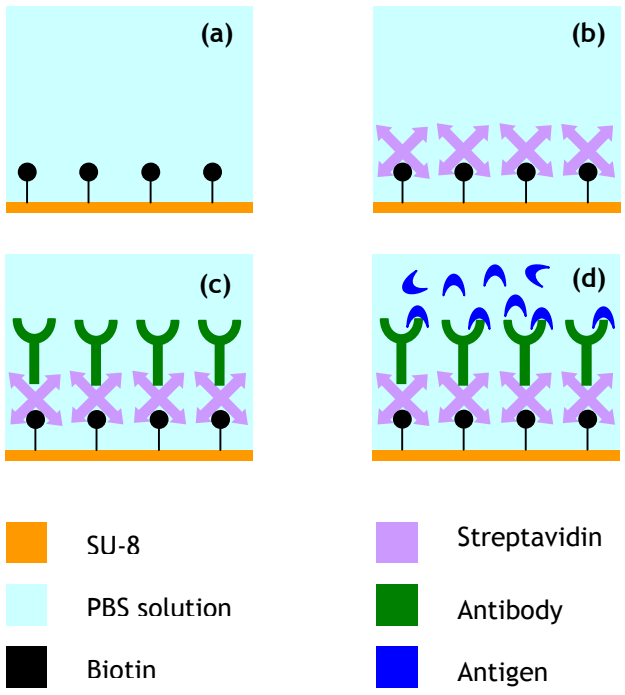

Figure 6.13: The schematic steps of basic configuration of biotin-streptavidin system that have been tested on the SU-8 sensor inside the microfluidic channel. (a) SU-8 surface with

immobilised biotin; (b) Unlabelled streptavidin molecules as a bridge; (c) Biotinylated antibody binding onto the binding site and (d) Specific antigen binding onto the antibody.

Figure 6.13 illustrates the basic configuration of biotin-streptavidin system detection by using a fabricated SU-8 polymer sensor. Firstly, the sensor surface was immobilised with NHS-biotin (as discussed in **Chapter 4.3**). Then, the PBS solution was introduced into the microfluidic channel and covered the sensing area. This stage was used as a reference stage for the resonance peak measurement before the binding of a protein or antibody binding was performed. When non-labelled streptavidin solution was introduced into the microfluidic channel, the resonance wavelength response was recorded at every three seconds for sensing analysis. A flow rate of (0.05 ml/min) was used and it was assumed that the streptavidin molecules had formed a monolayer on the sensing surface by the t = 150 s, since the resonance pattern stabilized. After incubation with a biotinylated antibody, an appropriate antigen was added to complete the detection experiment. (Note: PBS rinsing solution was used in between of each step, in order to remove any non-absorbed molecules that can possibly interfere with detection of the bulk analytes.

As before, the experimental setup and delivery system used was as in **Figure 4.4 and Figure 4.9**. With the valve selected to pump no 1, PBS solution was delivered into the microfluidic channel. This was flowed for t = 30 s to make sure there was no air bubbles inside the channel before the acquisition began. In order to monitor the resonance wavelength patterns, spectra were recorded every 3 seconds. The measurement procedure was similar to that used to collect the data as in **Figure 6.11**, but this time in **Figure 6.14** (below) shows, it involved a larger data set. The resonance shifts for different steps are tabulated in Table 6.4.

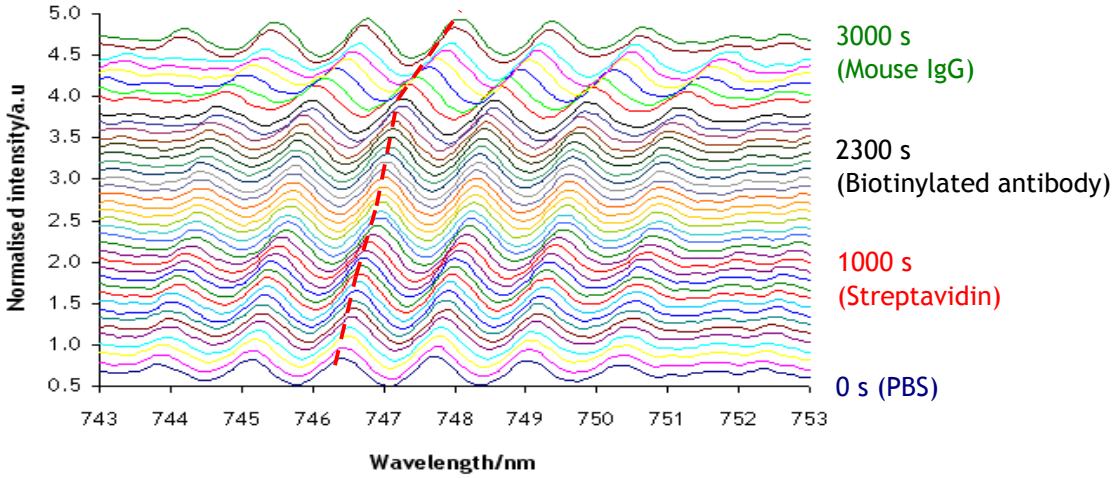

Figure 6.14: The full series of recorded resonance spectrum wavelength upon the experimental step. Each colour represented 50 s of data acquisition interval. The dashed (red) line shows the displacement of the monitored resonance peak.

Table 6.4: The summarized data from multiple proteins binding testing

Items	Test 1		Test 2	
	Resonance/nm	Shift /nm	Resonance/nm	Shift /nm
(1).PBS	745.219	0	745.120	0
(2).Streptavidin	745.655	0.436	745.550	0.430
(3).Biotinylated anti	745.916	0.697	745.820	0.700
(4).Mouse IgG	746.117	0.898	745.990	0.870
(5).d-biotin	746.700	1.481	746.780	1.660
(6).PBS	745.480	0.261	745.642	0.552

Plotting the data of **Table 6.4** and **Figure 6.14,** as in **Figure 6.15 (a)** shows that there was no effect of flowing PBS solution over the sensor surface, t = 0 - 150 s. The flow was switched to a second pump to allow the introduction of the streptavidin solution (0.03 mg/ml) which was introduced at t = 150 s, the monitored resonance wavelength peak shifted by approximately 0.436 nm from λ = 745.219 nm reference resonance wavelength peak. It remained steady at this value until t = 850 s. Subsequently, the biotinylated anti-Mouse IgG (0.03 mg/ml) was passed over the sensor from t = 980 s until t = 1800 s. This leads the chosen resonance wavelength to shift to 0.697 nm during that period.

In order to detect the specific binding properties of mouse IgG, biotinylated anti-Mouse IgG was introduced into the microfluidic channel continuously at t = 2000 s until t = 3000 s while the resonance wavelength pattern was recorded. As shown in the **Figure 6.15(iv)**, the resonance moved slightly approximately 0.898 nm and remained at the constant resonance wavelength value of λ = 746.117 nm, after the subsequent PBS solution rinsing stage.

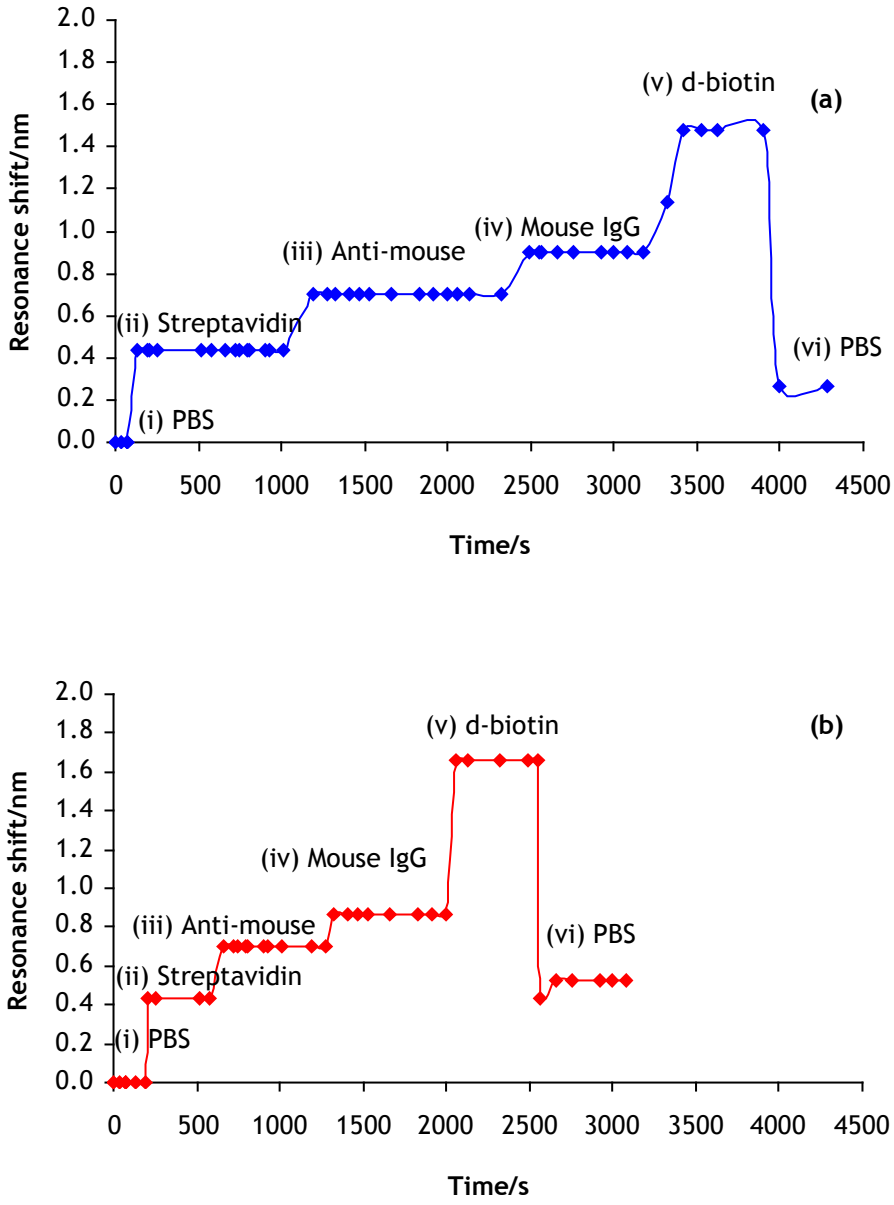

Figure 6.15: The calculated average value of resonance wavelength shift/nm according to the different protein binding activity upon the time scale of the experiment 1 (blue line) and experiment 2 (red line). (i) Reference wavelength due to immobilised biotin on sensing surface and surrounded by PBS media; (ii) streptavidin solution state; (iii) biotinylated anti-Mouse IgG; (iv) Mouse IgG antigen; (v) concentrated d-biotin solution and (vi) PBS solution.

In order to validate whether the observed resonance shifts were a consequence of biotin-streptavidin binding, a concentrated biotin solution was injected in order to disrupts the biotin-streptavidin bonding. The solution based biotin is able to displace the biotin group that is anchored to the SU-8 and allow the streptavidin to drift away from the surface. Thus, when a concentrated d-biotin solution (10 mg/ml) was introduced into the system at t = 3000 s, the

resonance shift sharply increased by 1.481 nm. This phenomenon was as expected since a higher concentration of d-biotin solution (10 mg/ml) solution will have a high refractive index. However, when the PBS rinsing solution was injected into the microfluidic channel at t = 3600 s, the monitored resonance shift sharply decreased to a level similar to that found for the streptavidin coated surface. Thus indicated that on this timescale, there was a possibility to dissociate the biotinylated-antibody-streptavidin binding with the concentrated d-biotin solution and a vast volume of the PBS solution. However, it did not completely remove the streptavidin molecule binding from the biotin.

When a second experiment as in **Figure 6.15(b)** was performed, it was notable that the resonance wavelength response also demonstrated nearly identical shift values to those of **Figure 6.15(a)**.

6.3 Summary

In a conclusion, it was demonstrated that the SU-8 polymer DDR could be utilised as a bulk refractive index measurement and showed a practical way of detecting the specific protein binding detection, although the shifts in resonance peak are small. The first experiments that consist of bulk refractive index measurement showed and explained the detection of continuous changing sucrose concentration. These gained a linear relationship between the resonance peak shift and sucrose concentration that allowed the determination of an 'unknown' solution. The resonance wavelength shift of this device is approximately 12 nm/RIU, compared to the individual prepared solution and unknown concentrated species were identified. In the second set of experiment, the fabricated device showed the capability of detecting the biomolecules (streptavidin, biotinylated antibody, antigen) that bound onto the surface of the sensor structure without using any fluorescence label. From the specific protein binding experimental results, it was shown that the fabricated device has offered the capability of specific protein sensing and also demonstrated a potential future towards label-free optical biosensing. It is notable that in the protein binding experiments, the overall resonance shifts are in the 1-2 nm range and thus similar to the FSR of a single ring/disk resonator. This similarity highlights the advantage of constructing a cascaded resonator device that has a more complex resonance spectrum envelope and wider composite FSR.

References

[1] C. Y. Chao, W. Fung, and L. J. Guo, "Polymer microring resonators for biochemical sensing applications," IEEE Journal of Selected Topics in Quantum Electronics, vol. 12, pp. 134-142, 2006.

[2] K. De Vos, I. Bartolozzi, E. Schacht, P. Bienstman, and R. Baets, "Silicon-on-Insulator microring resonator for sensitive and label-free biosensing," Optics Express, vol. 15, pp. 7610-7615, 2007.

[3] A. Delage, D. X. Xu, A. Densmore, S. Janz, P. Waldron, J. Lapointe, B. Lamontagne, T. Mischki, G. Lopinski, J. Schmid, and P. Cheben, "Label-free biological sensors based on ring resonators," Icton 2008: Proceedings of 2008 10th Anniversary International Conference on Transparent Optical Networks, Vol 4, pp. 2-5372, 2008.

[4] A. Densmore, D. X. Xu, P. Waldron, S. Janz, A. Delage, G. Lopinski, T. Mischki, P. Cheben, E. Post, J. Lapointe, and J. H. Schmid, "Label-free biosensing using silicon planar waveguide technology - art. no. 67962X," Photonics North 2007, Pts 1 and 2, vol. 6796, pp. X7962-X7962615, 2007.

[5] N. M. Green, "Avidin and Streptavidin," Methods in Enzymology, vol. 184, pp. 51-67, 1990.

[6] N. M. Green and E. J. Toms, "Dissociation of Avidin-Biotin Complexes by Guanidinium Chloride," Biochemical Journal, vol. 130, pp. 707-&, 1972.

[7] A. Ksendzov and Y. Lin, "Integrated optics ring-resonator sensors for protein detection," Optics Letters, vol. 30, pp. 3344-3346, 2005.

[8] V. M. N. Passaro, F. Dell'Olio, B. Casamassima, and F. De Leonardis, "Guided-wave optical biosensors," Sensors, vol. 7, pp. 508-536, 2007.

[9] F. Vollmer and S. Arnold, "Whispering-gallery-mode biosensing: label-free detection down to single molecules," Nature Methods, vol. 5, pp. 591-596, 2008.

[10] F. Vollmer, D. Braun, A. Libchaber, M. Khoshsima, I. Teraoka, and S. Arnold, "Protein detection by optical shift of a resonant microcavity," Applied Physics Letters, vol. 80, pp. 4057-4059, 2002.

[11] A. Yalcin, K. C. Popat, J. C. Aldridge, T. A. Desai, J. Hryniewicz, N. Chbouki, B. E. Little, O. King, V. Van, S. Chu, D. Gill, M. Anthes-Washburn, and M. S. Unlu, "Optical sensing of biomolecules using microring resonators," IEEE Journal of Selected Topics in Quantum Electronics, vol. 12, pp. 148-155, 2006.

[12] Hermanson, G. T. Bioconjugate Techniques (Second Edition), Academic Press: London, U.K., 2008.

[13] "Bellingham & Stanley Ltd, UK" [Online]. Available: http://www.bellinghamandstanley.com/

[14] Eppendorf AG, Germany. [Online]. Available: http://www.eppendorf.com

[15] Sigma-Aldrich, USA. [Online]. Available: http://www.sigmaaldrich.com

[16] Vector Laboratories Inc, USA. [Online]. Available: http://www.vectorlabs.com

CHAPTER 7

Summary and Future Work

Introduction

In this final chapter, the overall progress and results that have been achieved throughout this PhD research period are described together with the conclusions that can be drawn. The aims of this work, stated in the introductory section, are reiterated. The future path of the research and potential applications are also discussed.

7.1 Overall Summary and Conclusions

The motivation behind the research project was based upon creating an optical biosensor that can be produced using standard fabrication processes. Other important characteristics included operation in the visible wavelength region, ease of protein immobilised surface protocols and integration of the device with a microfluidic delivery system.

Generally, the promise of resonator devices for optical biosensor has previously been demonstrated by using Hydex® glass [1][2], Si_3N_4 [3][4], silicon-on-insulator (SOI) [5] and polymers [6][7][8] as the core material. In this work, SU-8 polymer was chosen as the core material to develop the sensing device due to its availability and ease of fabrication process. To date, most of the fabricated devices have also used a tuneable laser at λ = 1550 nm (at communication wavelengths) as the operating source. In contrast, the fabricated device in this work was to be designed to operate within the visible region of approximately λ = 500 – 800 nm. The operation

wavelength in the visible region gives the advantages of avoiding water absorption (which is strong in the IR), providing either label-free detection or label-free detection combined with fluorescence label detection, and the availability of a variety of light sources.

Generally, the main objectives of this thesis were to design, fabricate and characterise SU-8 polymer micro-resonator devices for applications in optical biosensing. These major aims were accomplished and some device applications investigated, based upon the experimental work using double-cascaded gapless SU-8 polymer disk resonators, operating in the visible wavelength region λ = 500-800 nm.

Prior to fabrication, FDTD simulation was performed using a variety of resonator designs in order to evaluate the resonance wavelength patterns. This provided a better understanding of the general behaviour of devices across a range of parameters, prior to performing actual experiments with fabricated devices. However, the insights gained from the simulation were limited since the simulation software from Lumerical could only cope with small structures. For example, two dimension (2D) resonator designs (40 μm of radius) of greater than 40 μm required simulation areas, which were found to be either beyond the limit of the software, or needed large amounts of memory and long computational times. 3D simulation was not possible at all. Consequently, simulations were performed using $1/10^{th}$ scale models.

The fabrication processes were optimised by using the electron beam lithography fabrication tools and laboratory facilities in the JWNC. Extensive work enabled a 200 nm gap between the disk resonator structure and bus waveguide on the SU-8 polymer structure to be made and reproduced reliably. However, difficulties were found to arise when trying to make smaller gaps due to inconsistent expansion of the SU-8 polymer.

To overcome this gap-spacing problem, devices that had no gap between the bus waveguide and resonator structure were proposed. This approach eliminated the gap spacing and at the same time improved the coupling between the bus waveguide and resonator structure.

Devices were characterised by using a visible light source that covered the spectrum of λ = 500 – 800 nm. The introduction of a DDR generated a wide composite FSR allowing the resonance wavelength shift to be monitored. The composite FSR value between the central groups of resonance pattern was approximately 10 nm. These resonance patterns were suitable to enable monitoring of both solution refractive index changes and also protein binding interactions, in real-time.

Since the SU-8 polymer was used as the material to construct the sensing device, surface modification was performed in order to immobilise proteins onto the surface, for example, the deposition of biotin layers for capturing streptavidin and other molecules. As part of this work,

surface characterizations were performed to determine the functional groups of the SU-8 polymer, and the structural changes in the polymer at various stages of immobilization protocol. Two characterization methods were used: fluorescence labelling using FITC and XPS analysis. These investigations allowed optimization of the protein immobilization protocol and showed that it was efficient.

In order to introduce the analytes to the sensing area, a microfluidic channel system was constructed. This allowed calibrations to be performed by supplying a solution of continuously varied sucrose concentration into the microfluidic channel. This calibrations curve could then be used to measure an individual sucrose solution of unknown concentration.

Following this calibration, other more extensive experiments were conducted in order to develop an antibody binding assay. A sensing surface was prepared by immobilised NHS-biotin and subsequently used to measure the resonance wavelength shift when further molecular binding interactions occurred, for example forming a monolayer of, streptavidin. This was performed by injecting prepared streptavidin solutions onto the biotinylated devices as well as onto untreated devices, (to differentiate between specific and non-specific absorption). From these results, the resonance shift for streptavidin binding was determined (0.261 nm). These measurements also showed that the streptavidin binding interaction only occurred when the immobilised biotin was present on the SU-8 polymer surface.

Further investigations on the capability of the fabricated sensor to detect on multiple protein binding interactions were performed. In these experiments, the free binding sites on immobilised streptavidin were used as a bridge to bind biotinylated antibodies. Two experiments were performed and selected wavelength peaks were analysed to measure the resonance wavelength shift corresponded to the antibody binding interactions. The resonance wavelength shift value for each consecutive experiment exhibited similar responses upon the flow of specific molecules. One of the main goals in the research objective was therefore achieved.

The reversibility of the antibody-streptavidin-biotin interaction was investigated through the addition of concentrated d-biotin solutions, which were introduced into the microfluidic channel in order to “release” the streptavidin molecules from the biotin. These experiments were not wholly successful and in future, further experiments need to be carried out to break the biotin-streptavidin binding and regenerate the SU-8 polymer surface, in order to have reusable devices.

In summary, and in brief, the use of the compact device of SU-8 polymer DDR for an optical biosensor can be deemed successful. The straightforward fabrication process resulted in a rapid fabrication flow without performing a number of more involved fabrication processes, such as deep reactive ion etching (RIE)(as might be required for glass/Si). In addition, the

difficulty of obtaining reproducibility of the narrow gap spacing between the bus waveguide and resonator was overcome by proposing the idea of a gapless structure, which was achieved without sacrificing coupling efficiency or sensitivity. Experiments with bulk refractive index solutions using sucrose and specific protein binding layers were successfully demonstrated in this work.

7.2 Future work

7.2.1 Materials and Methods

There were two part of experiments performed in this section. The first experiment involved the deposition of a thin metal film (Platinum (Pt)) using Plassys MEB 400S Electron Beam Evaporator in the JWNC cleanroom. Then the experiment was conducted using the experimental setup as shown in earlier chapter (Figure 4.4, Chapter 4). In the second section experiment, a similar experimental setup shown in **Figure 4.4** and **Figure 4.9** was used for the protein immobilization experiments. SU-8 polymer sensing areas inside the microfluidic channel were functionalised with NHS-biotin B3295 (Sigma-Aldrich, USA) using protocol in **Chapter 3**. The materials and chemicals utilised in experiments were a Dylight 649® streptavidin (Vector Laboratories Inc, USA), Dulbecco's Phosphate Buffer Saline (PBS) D8537 (Sigma-Aldrich, USA) and DI water.

7.2.2 Quantitative Measurement

An obvious difficulty in making quantitative absolute measurement with the micro-resonator configuration is in working out the precise surface coverage that gives a certain shift in resonance wavelength. Whilst it might be possible to develop formulae to do this based upon the equations that describe the propagation of light in a resonator system, these are not straightforward. Thus, in an attempt to circumvent this problem, a thin metal film was deposited on the resonator surface with the aim of being able to deposit well defined layer-by-layer assemblies (the deposition of metallic surfaces is much better defined than on an SU-8 surface and can be quantitatively measured using electrochemical or external FTIR reflectivity techniques. A brief investigation of this showed that for a 10 nm layer of Pt, the optical attenuation was not too large and this may be an avenue worth exploring in the future.

7.2.3 Spectral Absorption and Resonance Wavelength Shift Analysis

In the immediate future, further applications on protein binding detection that involved colourimetric assays have been proposed, utilizing the recently optimised experimental setup (see **Figure 4.4** and **Figure 4.9(a)**), developed in this project.

The hypothesis behind this experiment is based on the device being able to operate in the visible wavelength region. This means that resonance wavelength shifts can be combined with optical absorption at the resonance wavelengths by a colour centre in, say, a fluorophore tag. For example, if the coloured Dylight 649® streptavidin was bound to the resonator surface, then those wavelengths that couple into the resonator will be attenuated due to interaction with the Dylight 649® colour centre. In contrast, those wavelengths that do not couple into the resonator and so are not absorbed by the Dylight 649® colour centre will pass along the bus waveguide without attenuation. Thus, if the ratio of the intensity of adjacent on and off-resonance features is measured, this should dramatically decrease in spectral regions where the Dylight 649® absorbs. This would open up the exciting possibility of being able to perform absorption spectroscopy without the need for the 'blank' reference measurements that are always used in current spectrophotometer configurations (see **Appendix A.4.2**).

Initial experiments to investigate the detection of protein with fluorophore conjugates have already been performed. These involved injecting Dylight 649® streptavidin (**Vector, SA-5649**) onto an SU-8 polymer sensing area that was already functionalised with NHS-biotin. The measurement wavelength region was set from 600 to 700 nm for the real time monitoring, and the spectral response due to the binding interaction (Dylight 649® absorb at 655 nm).

Figure 7.1 shows a schematic diagram of a molecular assembly constructed for the colourimetric absorption assay. The optical response from the output waveguide was acquired in real time and during the course of the Dylight 649® streptavidin immobilization. DI water was used as a reference background, both before and after the Dylight® 649 streptavidin addition step.

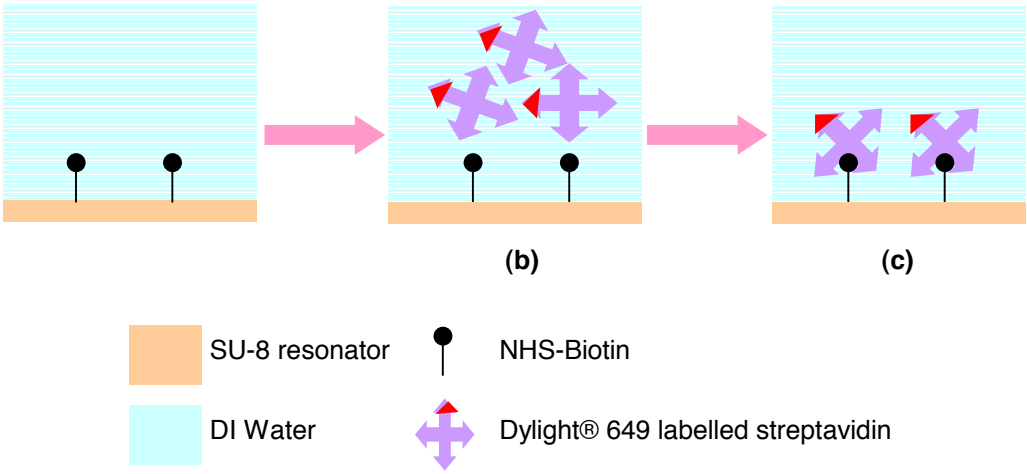

Figure 7.1: The schematic diagram for protein binding and fluorescence labelling experiment. (a) Immobilised NHS-Biotin, (b) Dylight® 649 labelled streptavidin solution and (c) Biotin-Dylight® 649 streptavidin binding.

Figure 7.2(a) shows the change in optical response that occurs as a consequence of Dylight 649® streptavidin binding. This is a consequence of the strong optical absorption occurring within this region. The spectroscopic shape of this response is dramatically different to that seen when non-labelled streptavidin or sucrose solutions are passed over the SU-8 surface (see **Figure 6.11**).

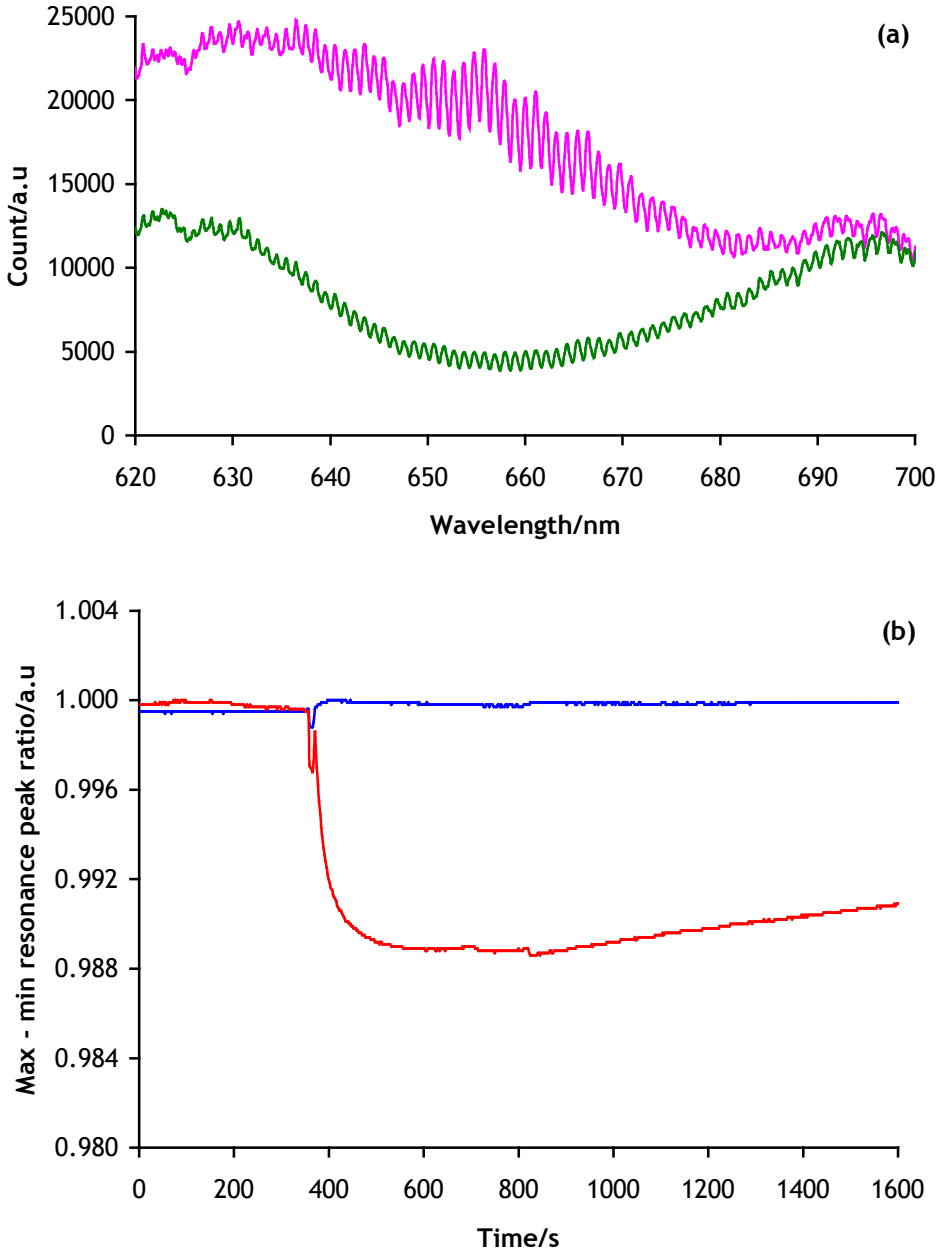

Figure 7.2: The optical response of the fabricated device correspond to the Dylight® 649 streptavidin solution that was injected into the microfluidic channel. (a) Resonance wavelength spectrum at different recorded times, t = 100 - 250 s (magenta line) and t = 270 - 800 s (green line) and (b) The ratio value between maximum to minimum peak at different selected wavelengths 600 nm (blue line) and 655 nm (red line) along the experimental period.

In **Figure 7.2(b)**, the ratio of the adjacent on and off-resonance features was plotted for two wavelength regions, one at 630 nm and the other at 655 nm, against time. For the 630 nm features, the ratio showed a constant value from the beginning until the end of the experiment. I.e. No absorption at 630 nm happened throughout the experiment. In contrast, the calculated ratio at around the 655 nm features demonstrated a decreases from 1.000 to 0.988 as Dylight®649 streptavidin was bound from the solution. The signal to noise value for this ratio measurement was very good and the ratio remained stable up until the injection of DI water at t = 800 s.

Finally, **Figure 7.3** shows the collected spectra from experiments conducted before and after Dylight®649 streptavidin solution was introduced into the microfluidic channel system. Here, it can be seen that there is also a resonance wavelength shift of 0.261 nm when streptavidin molecules bind onto the immobilised biotin on the sensing surface.

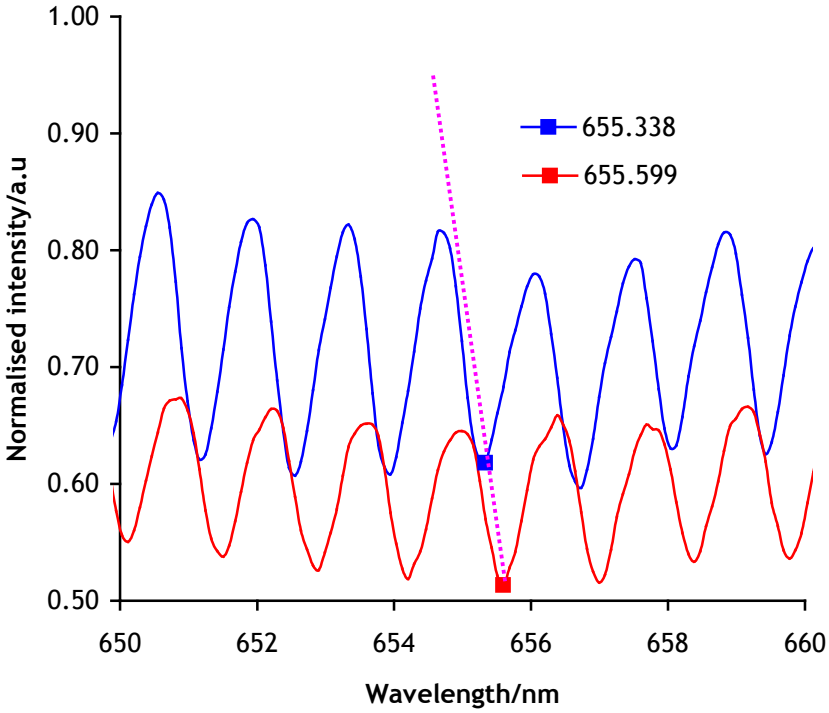

Figure 7.3: Normalised intensity of recorded resonance response at 200 s (blue line) and 1500 s (red line). Dashed line (magenta) shows the resonance shift before and after Dylight 649® streptavidin steps. Resonance spectra were vertically displaced for clarity.

Thus, by exploiting the capability of the fabricated device at the visible wavelength region, fluorescence labelled molecules can be utilised in order to measure protein binding interaction and these can be augmented with resonance shift measurements to offer the prospect of improving the detection limit in assays or resolving the contribution of different labelled and unlabelled species to the sensor response. Importantly, the combination of two

detection techniques in a single device will provide a platform for further enhancement of the optical biosensor in either the label or label-free detection method. In addition, with the establishment of more complex microfluidic delivery system, this fabricated device will lead towards an integrated optical biosensor having real time detection capabilities.

7.3 Conclusion

In conclusion, the fabricated SU-8 polymer double-cascaded gapless disk resonator device with microfluidic channel arrangement system was successfully fabricated, characterised and applied to assay experiments in this work. The operational wavelength at visible region exhibited a potential platform for the resonance wavelength shift detection in optical biosensing. Future work is focused on combining the resonance shift detection and optical absorption spectral analysis by utilizing the advantage of the fabricated device that can be operated in visible wavelength region.

References

[1] A. Yalcin, K. C. Popat, J. C. Aldridge, T. A. Desai, J. Hryniewicz, N. Chbouki, B. E. Little, O. King, V. Van, S. Chu, D. Gill, M. Anthes-Washburn, and M. S. Unlu, "Optical sensing of biomolecules using microring resonators," IEEE Journal of Selected Topics in Quantum Electronics, vol. 12, pp. 148-155, 2006.

[2] A. Ramachandran, S. Wang, J. Clarke, S. J. Ja, D. Goad, L. Wald, E. M. Flood, E. Knobbe, J. V. Hryniewicz, S. T. Chu, D. Gill, W. Chen, O. King, and B. E. Little, "A universal biosensing platform based on optical micro-ring resonators," Biosensors & Bioelectronics, vol. 23, pp. 939-944, 2008.

[3] C. A. Barrios, "Optical Slot-Waveguide Based Biochemical Sensors," Sensors, vol. 9, pp. 4751-4765, 2009.

[4] C. F. Carlborg, K. B. Gylfason, A. Kazmierczak, F. Dortu, M. J. B. Polo, A. M. Catala, G. M. Kresbach, H. Sohlstrom, T. Moh, L. Vivien, J. Popplewell, G. Ronan, C. A. Barrios, G. Stemme, and W. van der Wijngaart, "A packaged optical slot-waveguide ring resonator sensor array for multiplex label-free assays in labs-on-chips," Lab on a Chip, vol. 10, pp. 281-290, 2010.

[5] K. De Vos, J. Girones, S. Popelka, E. Schacht, R. Baets, and P. Bienstman, "SOI optical microring resonator with poly(ethylene glycol) polymer brush for label-free biosensor applications," Biosensors & Bioelectronics, vol. 24, pp. 2528-2533, 2009.

[6] P. Rabiei and W. H. Steier, "Micro-ring resonators using polymer materials," Leos 2001: 14th Annual Meeting of the Ieee Lasers & Electro-Optics Society, Vols 1 and 2, Proceedings, pp. 517-518907, 2001.

[7] C. Y. Chao, W. Fung, and L. J. Guo, "Polymer microring resonators for biochemical sensing applications," Ieee Journal of Selected Topics in Quantum Electronics, vol. 12, pp. 134-142, 2006.

[8] M. Balakrishnan, M. Faccini, M. B. J. Diemeer, E. J. Klein, G. Sengo, A. Driessen, W. Verboom, and D. N. Reinhoudt, "Microring resonator based modulator made by direct photodefinition of an electro-optic polymer," Applied Physics Letters, vol. 92, pp. -, 2008.

[9] Vector Laboratories Inc. [Online] http://www.vectorlabs.com

[10] Sigma-Aldrich Corp. [Online] http://www.sigmaaldrich.com

Appendix

A.4.1 Abbe Refractometer 60

An Abbe refractometer is an instrument that measures the refractive index of material. It can particularly measure solid and semi-solid material such as thin polymer, rubber and honey or liquids. For example, it can also be used to determine the solution refractive index of a fragrance, oil, plastics or resins. The instrument employs a critical angle effect that is marked by a boundary line between the light and dark portion of a prism imaged in an objective lens. The Abbe refractometer 60 instrument covers the refractive index range from 1.20 to 1.70, utilizing the sodium D_1 line illumination at 586.6 nm of wavelength. The reading from an eyepiece scale is divided to 0.1 allowing for estimation to ±0.0001of refractive index.

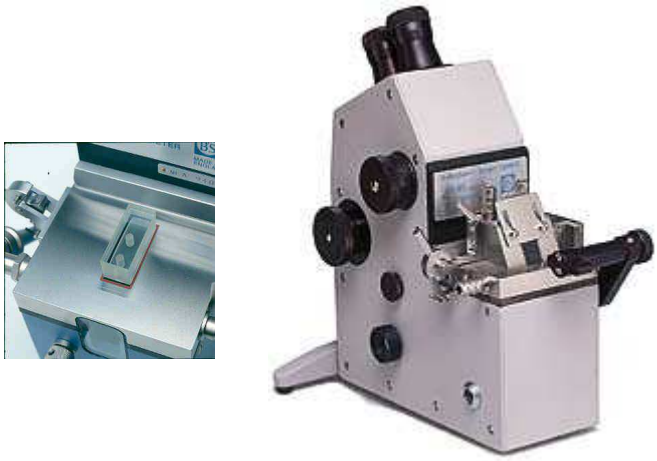

Figure A.4.1: Abbe refractometer 60 for refractive index measurement.

Generally, calibration of the instrument has to be done prior to measurements of unknown samples. Here, a standard silica piece with specific refractive index of 1.45848 should read 16.336^{o} on the refractometer scale was employed for calibration. After the calibration procedure, a small drop of liquid sample was pipette onto the fixed prism for measurement. The liquid will be spread out to cover the fixed prism interface. The eyepiece knob was turned until the position where the field was divided onto light and dark position (dark below). The borderline was carefully tuned until accurately set on the intersection of cross-wire. The observation scale angle was recorded and compared with the standardization table for refractive index values. This procedure and images were obtained from the Bellingham + Stanley website.

A.4.2 Hitachi U-2000 spectrophotometer

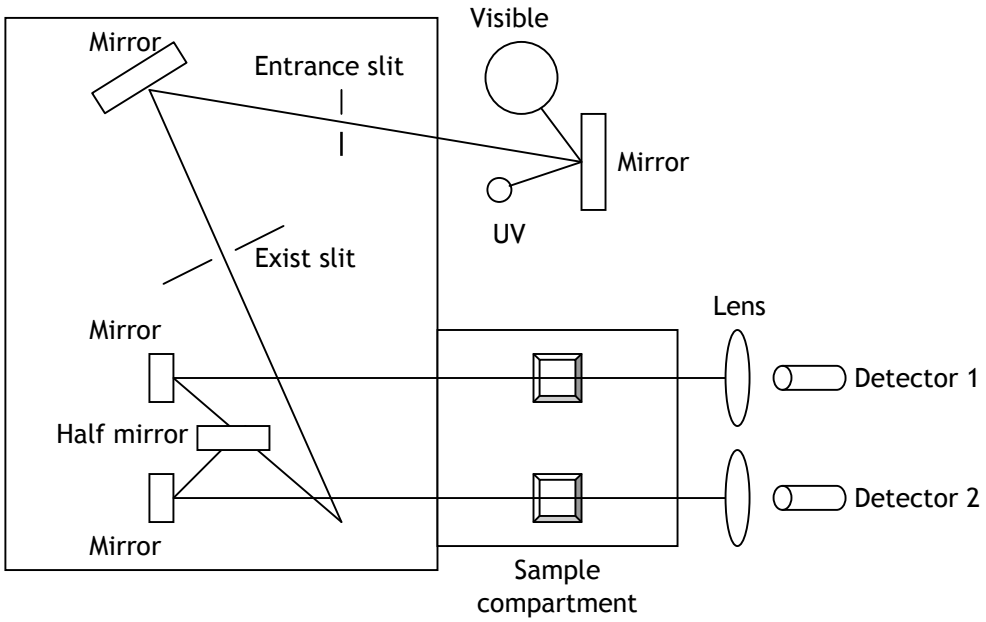

Figure A.4.2: Double beam spectrophotometer for absorbance measurement.

Figure A.4.2 illustrates the double beam UV/VIS spectrophotometer block diagram for a Hitachi U-2000 series instrument that was used to quantify the absorbance of the tested material. This equipment has a double beam design to enhance the linearity and accuracy of the detection. Light source energy is divided into two sections; half of the light will be passed through the reference and the other counterpart propagated through the sample. Absorptivity of light through the sample was measured and compared to the reference signal, using a suitable photodetector. This allows changes due to light source fluctuations to be compensated for, so ensuring the stability of the spectrum measurement for a longer time and allowing broad spectrum scanning.

From the Beer-Lambert Law, absorption is given as follows:

$$A_\lambda = -\log\frac{I}{I_0}$$

Where A = absorbance, λ = wavelength, I_0 = intensity of light before and I = intensity of light after propagated inside the sample.

A.5.1 Chemical structure of (3-Aminopropyl) triethoxysilane

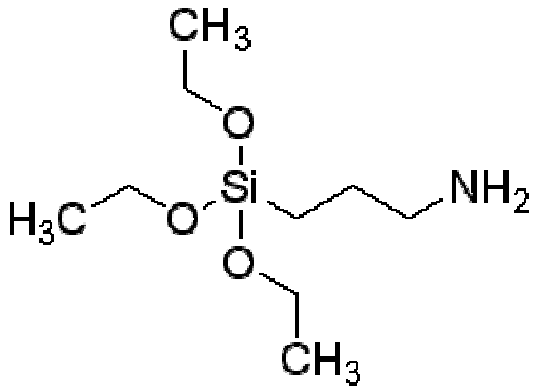

Figure A.5.1: Shows the (3-Aminopropyl)triethoxysilane (APTES 99%) structure. This chemical structure was obtained from Sigma-Aldrich website. (Cat. No. 440140)

A.5.2 Protocol for SU-8 functional group detection

1. Samples were treated in oxygen plasma for 10 min at 100W.
2. Samples were incubated in APTES 98% in ethanol for 1h at 60°C.
3. Dried with ethanol and put in the oven for 2 hours at 120°C.
4. 200 µl of DMSO and 2mg FITC were dissolved.
5. Reaction buffer are prepared (1.7 g of $NaCO_3$ + 2.8g of $NaHCO_3$ + water, pH 9.5).
6. Samples were incubated with (FITC in DMSO 1mg/ml) in reaction buffer for 1 h.
7. Rinsed with DI water and ready for measurement.

A.5.3 Surface modification and immobilization protocol

1. Samples were treated with O_2 plasma for 30 s at 100W, and then the samples were incubated in H_2SO_4 (0.1M) or ethylenediamine C_2H_4 $(NH_2)_2$ for overnight.
2. Samples rinsed with water (H_2O).
3. Samples were soaked in the aminosilane solution APTES 99% (3-Aminopropyl)triethoxysilane, 440140-Aldrich) in (ethanol 98%. – 20ml = 19.5 ethanol + 0.5 ml of H_20). (Total 3ml APTES in 97ml of ethanol) for 2 hours
4. Samples were rinsed with ethanol and dried.
5. Biotin solution: B3295 Biotinamidohexanoyl-6-aminohexanoic acid-N-hydroxysuccinimide ester + DMSO (25mg/mL) until dissolved.
6. Samples were incubated in biotin for 1 hour – flipped down
7. Samples were rinsed with PBS pH 7.4 / water

8. Streptavidin–FITC (Streptavidin–FITC from *Streptomyces avidinii* – S3762 Sigma Aldrich) was prepared (1mg/mL of water)
9. Samples were incubated with streptavidin – FITC module for 0.5 – 1 hour and covered to avoid photobleaching.
10. Rinse with PBS pH 7.4 and store in PBS solution in the fridge for next measurement.

A.5.4 High resolution X-ray photoelectron spectrometer

XPS is a technique that involved the photoelectron effect to investigate the chemical element on the surface of the sample. High-energy X-ray photons are focused onto the sample. This high energy is absorbed by the electron of the surface elements. Electrons with a specific energy, determined by the particular atom and X-ray energy will be ejected from the surface and collected by a hemispherical analyser. There, the energy of electrons is measured and a resulting intensity peak displayed at the spectrometer. By analysing the peak position, elemental species on the sample can be determined. Since the binding energy of electron on the surface was different between the known energy of the X-ray beam and kinetic energy of the emitted electron, the electron binding energy can be calculated from the equation below:

$$E_{BE} = hv - \left(E_{kin} + \theta\right)$$

where E_{BE} is the binding energy (eV), hv = energy of X-ray photon, E_{kin}= kinetic energy of electron and θ is constant according to the spectrometer work function.

XPS facilities that located in Daresbury Laboratory, employed a high power rotating anode A1K(α) at 1486.7 eV. This rotating anode obtained the maximum power of 8kW. The detection system consists of a hemispherical electron analyser and multi-channel detector which was utilised to increase the sensitivity of the instrument after the electrons pass through the analyser. A high vacuum chamber with a three-axis manipulator was used to define the take off angle precisely.

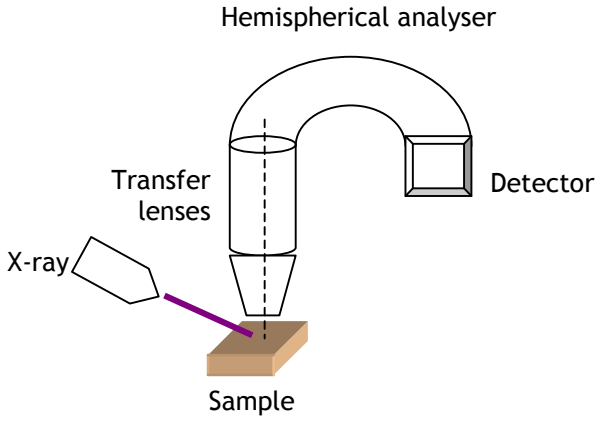

Figure A.5.3: The schematic diagram of the XPS instrument.

A.6.1 Sugar scale concentration and refractive index standard.

Standardisation of Model 60/SO

Since this model does not carry a refractive index scale the model standardisation procedure cannot be followed. Instead of the test plate and contact liquid referred to in the general instructions, a bottle of test oil is provided together with a table of Oil scale values at various temperatures. A few drops only of test oil is applied to the polished prism and the hinged prism closed over it in the same way as for routine measurements. From the table, determine the correct reading for the oil and adjust the scale reading to this figure by the method described under section 3.

Measurements of samples required in terms of refractive index may be made using the sugar scale and the conversion table below.

Sugar %	N_D^{20}	Sugar %	N_D^{20}	Sugar %	N_D^{20}
0	1. 33299	32	1. 38474	64	1. 45107
1	1. 33442	33	1. 38658	65	1. 45342
2	1. 33587	34	1. 38843	66	1. 45578
3	1. 33732	35	1. 39029	67	1. 45816
4	1. 33879	36	1. 39217	68	1. 46055
5	1. 34027	37	1. 39406	69	1. 46297
6	1. 34176	38	1. 39597	70	1. 46540
7	1. 34325	39	1. 39789	71	1. 46785
8	1. 34477	40	1. 39982	72	1. 47031
9	1. 34629	41	1. 40178	73	1. 47280
10	1. 34782	42	1. 40374	74	1. 47530
11	1. 34937	43	1. 40573	75	1. 47782
12	1. 35092	44	1. 40772	76	1. 48036
13	1. 35249	45	1. 40974	77	1. 48292
14	1. 35407	46	1. 41177	78	1. 48549
15	1. 35567	47	1. 41381	79	1. 48808
16	1. 35727	48	1. 41587	80	1. 49069
17	1. 35889	49	1. 41795	81	1. 49332
18	1. 36052	50	1. 42004	82	1. 49597
19	1. 36217	51	1. 42215	83	1. 49864
20	1. 36382	52	1. 42428	84	1. 50132
21	1. 36549	53	1. 42642	85	1. 50403
22	1. 36718	54	1. 42858	86	1. 50675
23	1. 36887	55	1. 43075	87	1. 50949
24	1. 37058	56	1. 43294	88	1. 51225
25	1. 37230	57	1. 43515	89	1. 51503
26	1. 37404	58	1. 43737	90	1. 51783
27	1. 37579	59	1. 43961	91	1. 52064
28	1. 37755	60	1. 44187	92	1. 52348
29	1. 37933	61	1. 44415	93	1. 52633
30	1. 38112	62	1. 44644	94	1. 52921
31	1. 38292	63	1. 44875	95	1. 53210

For further supplies of test liquid order catelogue No. 60/TL.

12/12

A.6.2 Refractive Index of Collected Solution.

The measurement results of refractive index from Abbe refractometer against the collected solution from outlet tubing during the experiment.

		Test1		Test2		Average
Item	Sucrose (50)%	Abbe (°)	Ref Index	Abbe (°)	Ref Index	Ref index
1	0	3.641	1.33511	3.707	1.33611	1.33561
2	5	4.083	1.34007	4.078	1.34007	1.34007
3	10	4.279	1.34205	4.291	1.34205	1.34205
4	15	5.447	1.35294	5.439	1.35294	1.35294
5	20	5.694	1.35591	5.687	1.35591	1.35591
6	25	6.467	1.36380	6.563	1.36479	1.36430
7	30	6.734	1.36578	6.723	1.36578	1.36578
8	35	7.139	1.36972	7.085	1.36972	1.36972
9	40	7.738	1.37562	7.735	1.37562	1.37562
10	45	8.265	1.38150	8.241	1.38052	1.38101
11	50	8.493	1.38346	8.507	1.38346	1.38346

		Test1		Test2		Average
Item	Sucrose (80)%	Abbe (°)	Ref Index	Abbe (°)	Ref Index	Ref Index
1	0	4.141	1.34007	4.147	1.34007	1.34007
2	8	4.625	1.34502	4.619	1.34502	1.34502
3	16	5.343	1.35195	5.370	1.35294	1.35245
4	24	5.583	1.35492	5.558	1.35492	1.35492
5	32	7.017	1.36873	7.015	1.36873	1.36873
6	40	7.928	1.37758	7.967	1.37856	1.37807
7	48	8.847	1.3864	8.787	1.3864	1.38640
8	56	9.649	1.39421	9.641	1.39421	1.39421
9	64	10.644	1.40393	10.665	1.40489	1.40441
10	72	11.576	1.41359	11.563	1.41359	1.41359
11	80	11.732	1.41455	11.729	1.41455	1.41455

A.6.3 The measured data for sucrose concentration (%), refractive index and resonance wavelength (nm) for continuous flow sucrose solution experiment.

Item	Sucrose (50)%	Start(s)	Finish(s)	Ref Index (n)	Resonance(nm)	Shift(nm)
1	**0**	0	360	1.33561	758.144	0.000
2	**5**	380	740	1.34007	758.231	0.087
3	**10**	770	1130	1.34205	758.231	0.087
4	**15**	1150	1510	1.35294	758.318	0.174
5	**20**	1590	1850	1.35591	758.318	0.174
6	**25**	1984	2334	1.36430	758.405	0.261
7	**30**	2360	2720	1.36578	758.405	0.261
8	**35**	2745	3105	1.36972	758.492	0.348
9	**40**	3135	3495	1.37562	758.666	0.522
10	**45**	3530	3890	1.38101	758.666	0.522
11	**50**	**4050**	**4424**	**1.38346**	**758.753**	**0.609**

Item	Sucrose (80)%	Start(s)	Finish(s)	Ref Index (n)	Resonance(nm)	Shift(nm)
1	**0**	0	100	1.34007	758.027	0.000
2	**8**	100	460	1.34502	758.114	0.087
3	**16**	504	864	1.352445	758.114	0.087
4	**24**	934	1294	1.35492	758.201	0.174
5	**32**	1275	1635	1.36873	758.288	0.261
6	**40**	1703	2063	1.37807	758.375	0.348
7	**48**	**2102**	**2462**	**1.38248**	**758.637**	**0.610**
8	**56**	2561	2921	1.39421	758.811	0.784
9	**64**	2955	3315	1.40441	758.985	0.958
10	**72**	3368	3728	1.41359	759.072	1.045
11	**80**	3838	4198	1.41455	759.247	1.220